Feasibility Study of Femtosecond Laser Written Arrayed Waveguide Gratings for Astronomy

By

Glen Douglass

A thesis submitted to Macquarie University
for the degree of Master of Research
Department of Physics & Astronomy
March 2015

© Glen Douglass, 2015.

Typeset in LaTeX 2_ε.

Except where acknowledged in the customary manner, the material presented in this thesis is, to the best of my knowledge, original and has not been submitted in whole or part for a degree in any university.

Glen Douglass

Acknowledgements

First of all I would like to thank my supervisors: Professor Michael Withford and Dr. Simon Gross, for giving me the opportunity to conduct research in astrophotonics an area of great passion and interest to myself. I would like to thank Mick his for positive attitude, always highlighting the positives outcomes. Simon, thank you for all the knowledge you have patiently passed onto me in the lab, your willingness to help and solve any problem I have encountered is inspirational and I hope I can do the same to others students in the future.

I would like to specially thank Dr. Felix Dreisow, the time you spend in Australia helping me on my project has enabled my master thesis to reach outcomes few believed where possible in such a short time. Not only did you teach me valuable skills in the lab, you have have also given me advise for the future.

I would also like to thank the Masters group: Blake, MVB and Reece. All the late nights and stupid conversations have got me this far. Next I would like to thank every one in the Hearing Hub office especially Izza, Yuwen, Stokes, Marty, Pete and Thomas, for making a fun office environment.

I would like to thank my family, even though you still have no idea what Im doing I appreciate your support. Finally I would like to thank my beautiful girlfriend Stefany, for supporting me throughout the whole project and helping me be calm.

Abstract

This thesis studies the feasibility of femtosecond laser written array waveguide gratings (AWG) with an interest in astronomical applications. AWGs have recently been studied as a new integrated alternative to the current generation of astronomical spectrographs. AWGs have the advantage of being small, robust and stable all important factors sought after in astronomical instrumentation. One setback for the use of AWGs in astronomy is that current fabrication techniques are expensive and slow to prototype, making development of such devices difficult. This feasibility study has explored the possibility of fabricating AWGs using a laser direct write technique that is cheap and allows for fast design prototype. The femtosecond laser direct write technique uses a focused high powered laser to produce a localised refractive index change in a glass substrate which is typically used to form waveguides. To fabricate AWGs using the laser writing technique, the capability to inscribe large smooth planar waveguides that act as a 2D free propagation zones were evaluated. Once a suitable slab fabrication method was established a laser written AWG proto-type was produced with initial output showing a degree of correlation to the theoretical output at a single wavelength. From this initial proto-type design improvements were made to improve the device, however initial results shows that laser written AWGs are highly susceptible to phase array error which could affect the feasibility of laser written AWGs. This initial study shows that laser written AWGs could have future applications in telecommunications and integrated spectroscopic sensors when phase errors are minimised.

Contents

1 Introduction

The pursuit to understand the universe is part of human nature. This has driven man to look deeper into space than ever before. This desire to look at the far extent of our universe requires larger, more powerful telescopes to be constructed. With current generation telescopes being pushed to the edge of their design capabilities, larger more advanced telescopes are being proposed.

With the next generation of extremely large telescopes (Figure 1.1a) approaching, it has become clear that the current design of astronomical instruments (Figure 1.1b) will be impractical. As the size of a telescope increases, the size of traditional instruments also grows proportionally, creating new engineering problems and causing the cost to rise with as telescope aperture squared [1].

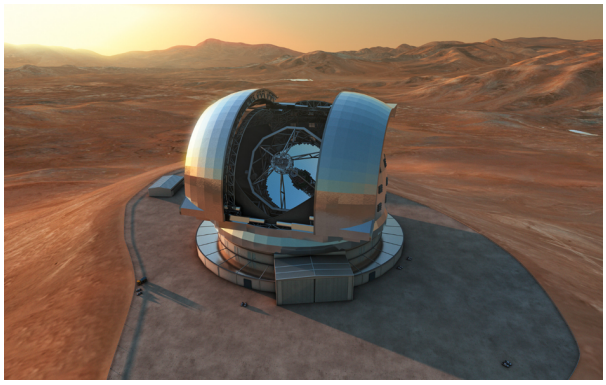

(a)

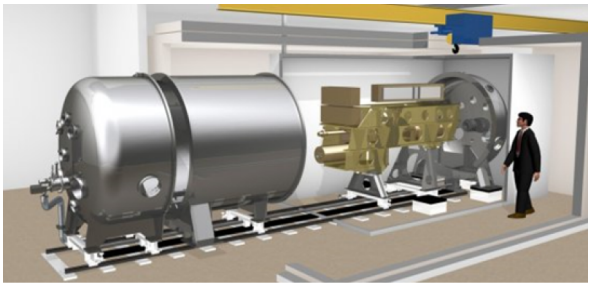

(b)

Figure 1.1: (a) Illustration of the proposed 39.3 m European extremely large telescope (E-ELT) in Chile (Licensed under Creative Commons). (b) Schematic of the HARPS high resolution spectrograph for an 3.6 m telescope [2].

The sheer cost and size of these new instruments has become a serious issue for new scientific endeavours causing the delay of many next generation telescopes. This has resulted in a great push by the astronomical community to develop smaller and cheaper instruments for the use on next generation telescopes.

Recent developments in photonics has provided an entirely new approach in designing next generation instrumentation. The field of photonics focuses on techniques to manipulate, generate and detect light in both the macro and microscopic scales, using new materials and processes to create photonic circuits. An example of a photonic technology that has been developed for the telecommunications industry is the optical fibre, which is now used extensively in astronomy to transport light to instruments.

To increase the data rate of optical fibre networks, wavelength division multiplexing (WDM) was introduced in the early 1980's [3]. Instead of transferring data using just one laser frequency, WDM uses multiple wavelengths to carry different data streams, dramatically increasing the data rate. With the implementation of the WDM technology new optical components known as wavelength demultiplexers and multiplexers were required to separate and combine the different wavelengths channels. One such device is the Array Waveguide Grating (AWG) also known as a waveguide grating router, optical phased array (PHASOR) or phased array waveguide grating.

AWGs were first proposed in 1988 by M. K Smit [4]. The first working devices were then reported by A. Vellekoop and M. K Smit [5, 6] designed for a wavelength of 633 nm. Shortly after functional devices for telecommunication wavelengths were developed [7]. C. Dragone then extended the concept from 1xN to NxN devices, which nowdays are used as wavelength routers [8, 9]. An alternative to the AWG is the photonic Echelle grating, which uses a micro-echelle grating on a photonic chip instead of a waveguide array. These devices have a smaller footprint, however it is challenging to machine smooth vertical gratings due to fabrication limitations [10]. This constraint has led to AWGs being the most commonly used waveguide router.

In 1995, Fred Watson [11, 12] proposed the use of integrated optics, specifically the photonic Echelle grating as a spectrograph for astronomy. At that time the technology and manufacturing techniques required to fabricate devices for astronomical applications were still being developed. The idea was essential forgotten till 2006 when Bland-Hawthorn *et.al.* [13] rejuvenated interest in the idea. This time the potential of the AWG as an integrated photonic spectrograph was proposed (see Figure 1.2). During this time AWG technology had been extensively developed by the telecommunications industry driving the fabrication techniques required to make high resolution and throughput devices. This development allowed astrophotonics to exploit existing technologies to realise AWG spectrographs for astronomy. In May 2011 Cvetojevic *et al.* [14] used an adapted off-the-shelve telecommunications AWG to successively undertake an on-sky demonstration of a AWG spectrograph for astronomy. The miniture photonic spectrograph observed CO molecular absorption bands at a resolving power of $R = 2500$ at a wavelength of 1600 nm. AWGs are particularly useful for astronomy for multiple reasons, these include: high efficiency, stability, robustness and the ability for mass production unlike current bulk optical spectrograph designs.

The fabrication of these devices, when small runs are required, is extremely expensive and time consuming. A more recent method for rapidly fabricating integrated photonic

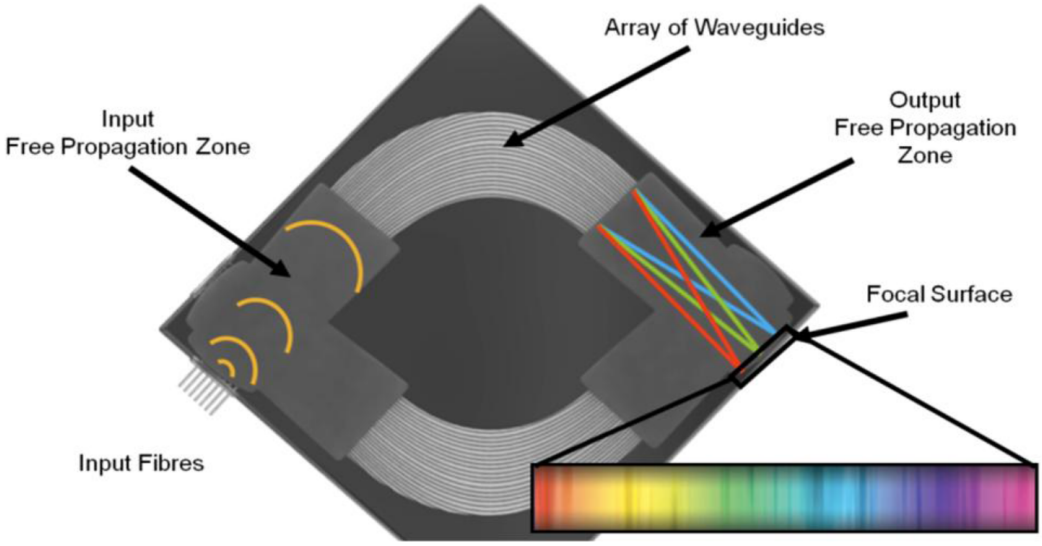

Figure 1.2: Illustration of AWG spectrograph on a small wafer [15].

circuitry is the femtosecond laser direct write technique. This technique allows for fast and cost effective manufacturing of devices, and for design alterations to be quickly tested. This laser-direct write technique has already been utilised to fabricate other new astronomical devices which include; photonic lanterns, stellar interferometers and in the near future OH suppression Bragg gratings [16–18].

In this thesis the feasibility of fabricating an integrated photonic spectrograph using the femtosecond laser direct write technique is evaluated. The theory,design and fabrication techniques utilised to fabricate components of an integrated spectrograph are outlined as well as a complete design and a first demonstration of a complete laser written device.

In Chapter 2 the fundamentals of the femtosecond direct-write technique are presented. Chapter 3 then explains the photonic circuitry of the Arrayed Waveguide Grating (AWG) including design, theory and current manufacturing process. Chapter 4 describes the experimental procedures used to fabricate, evaluate and design laser written AWGs. Chapter 5 focuses on the fabrication of a smooth laser written refractive index regions and tapers that are key components of AWGs. Chapter 6 outlines the fabrication techniques and challenges that had to be solved before fabricating a complete AWG. The chapter then finishes with initial experimental results of the complete device. Concluding remarks and future work are provided in Chapter 7.

2
Background

This chapter gives a general overview of the femtosecond laser direct write process. It begins with a brief description on how an optical fibre works. Next an overview of the nonlinear absorption mechanisms underlying the writing process is given, followed by a description of the three different modification regimes. The chapter concludes by reviewing writing techniques, glass selection, fluorescence and finally laser written slab waveguides.

2.1 Optical Waveguides

Optical waveguides use the process of total internal reflection to efficiently guide light. Optical fibres are fabricated with a high index core surrounded by lower index cladding. If light is injected into the core within the acceptance angle of the fibre, light is guided within the core region.

An important parameter that describes the guiding properties of a step index waveguide or fibre is the V number.

$$V = \frac{\pi d}{\lambda}\sqrt{n_{core}^2 - n_{cladding}^2} \tag{2.1}$$

where d is the core diameter, λ is the wavelength, n_{core} and $n_{cladding}$ are the refractive indices of the core and cladding, respectively. The V number provides an indication of the number of modes which can propagate in a fibre of a certain diameter and refractive index contrast. When $V < 2.405$ the fibre guides a single mode and when $V > 2.405$ the fibre guides multiple modes.

2.2 Femtosecond laser direct-write

In 1996 two different research groups [19, 20] demonstrated that focusing a sub-120 fs pulsed Ti:sapphire laser inside of a transparent material could induce a physical modification, (Figure 2.1). Glezer *et al.* [20], created 200 nm voids inside fused silica, while Davis *et al.* [19], used femtosecond pulses of a lower energy to create a highly localised refractive index change within various dielectrics. By focusing the laser beam inside the dielectric and translating the sample, a line of positive refractive index change was inscribed. This index change was shown to act as an optical waveguide. This landmark paper by Davis *et al.* [19], started the current research area of femtosecond laser direct-writing.

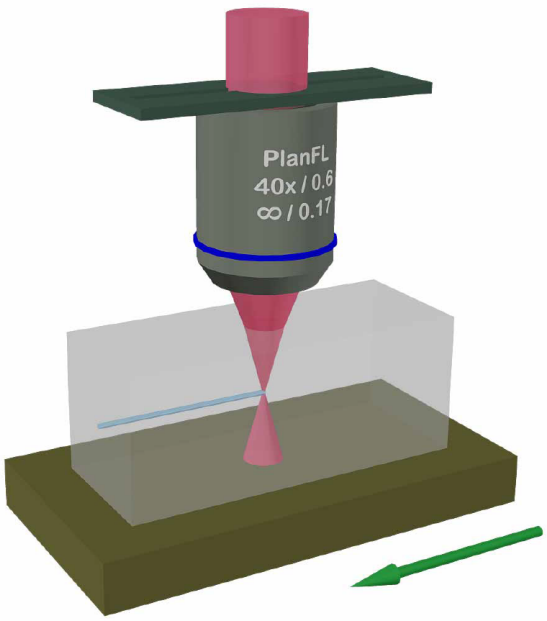

Figure 2.1: Femtosecond laser direct-write setup showing a femtosecond laser beam being focused into a slab of glass [21].

2.3 Nonlinear excitation mechanisms

To induce a refractive index change within a material energy needs to be transferred from the laser field to the material's lattice. In order to absorb the laser field's energy an electron must absorb enough energy to move from the valence band to the conduction band. For typical dielectrics e.g. fused silica, only an extreme UV photon can provide the energy required to bridge the band gap. As femtosecond pulses in the near infrared spectrum lack the photon energy to be linearly absorbed, a nonlinear excitation process is required. The two main processes are photoionisation and avalanche ionisation.

2.3.1 Photoionisation

Photoionisation refers to the direct excitation of an electron by the laser field. Photoionisation can be divided into two different regimes: tunnelling ionisation and multiphoton ionisation.

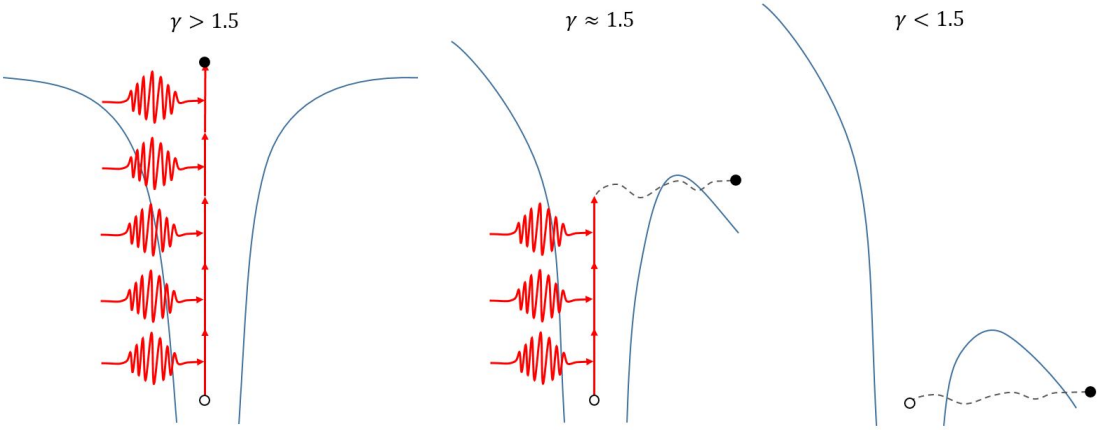

(a) Multiphoton ionisation (b) Intermediate regime (c) Tunnelling ionisation

Figure 2.2: Photoionisation

Tunnelling ionisation

When the intensity of the electric field is large, the electric field distorts the Coloumb barrier [22]. This suppresses the potential that binds the valence electron, allowing the electron to tunnel free, Figure 2.2c.

Multiphoton ionisation (MPI)

If multiple photons are absorbed simultaneously by a single electron, the electron can obtain enough energy to reach the conduction band, (see Figure 2.2a). The amount of photons required to be absorbed depends on the material and must satisfy $k\hbar\omega > E_g$, where k is the number of photons, $\hbar$ is Plank's constant, ω is the laser frequency and E_g is the materials band gap. Table 2.1 shows the typical band gap and photon numbers of different materials.

The MPI and tunnelling ionisation regimes can be distinguished by the Keldysh parameter γ [23],

$$\gamma = \frac{\omega}{e}\left[\frac{mcn\varepsilon_0 E_g}{I}\right]^{\frac{1}{2}} \tag{2.2}$$

where ω is the laser frequency, e and m is the charge and mass of an electron, c is the speed of light, n is the refractive index of the material, E_g is the band gap of the of the material, ε_0 is the permittivity of free space and I is the laser intensity.

If γ is larger then 1.5 MPI dominates, whereas for γ smaller than 1.5 tunnelling ionisation dominates.In the case of $\gamma \approx 1.5$ both contribute to the ionisation rate as shown in

Figure 2.2b. In other words MPI is the dominant photoionisation process for low intensities while tunnelling ionisation is dominant at high intensities. MPI is also the dominant process for low band gap materials, while tunnelling ionisation is more prominent for high band gap materials.

Material	E_g $[eV]$	k (800 nm)
Fused silica	9	6
Eagle 2000	4	2
BK7	5	3

Table 2.1: Band gap energies for typical optical glasses and the number of photons k required for MPI to bridge their band gap at a wavelength of 800 nm.

2.3.2 Avalanche ionisation

Avalanche ionisation is a two step process. First a free electron absorbs energy from the laser field. This absorbed energy can then be transferred to a valence electron via impact ionisation. If the absorbed energy is large enough, the valence electron can be promoted to the conduction band.

Avalanche ionisation has been found to be the dominant process for pulses of a few hundred femtoseconds and larger [24]. For shorter pulses MPI and tunnelling ionisation are the dominant excitation mechanisms [24, 25], whereas avalanche ionisation only has a minor contribution [26].

2.4 Energy tranfer

Regardless of the nonlinear ionisation mechanism, energy from the free electron plasma is transferred via electron-phonon coupling to the dielectrics lattice. Since this transfer time is $\approx$ 1 ps [27], the absorption and lattice heating processes are decoupled. The material modification can be classified into three different regimes; smooth refractive index change [1], birefringent structures and voids.

2.4.1 Smooth refractive index change

The creation of a smooth refractive index change is essential for the fabrication of low loss waveguides. The observed refractive index change cannot be attributed to just one process only but a range of different mechenism depending on the material. It was originally suggested by Davis *et al.* [19] that densification and strain was the source of the positive

[1] The refractive index change has been found to be positive or negative depending on the inscription parameters and the material used.

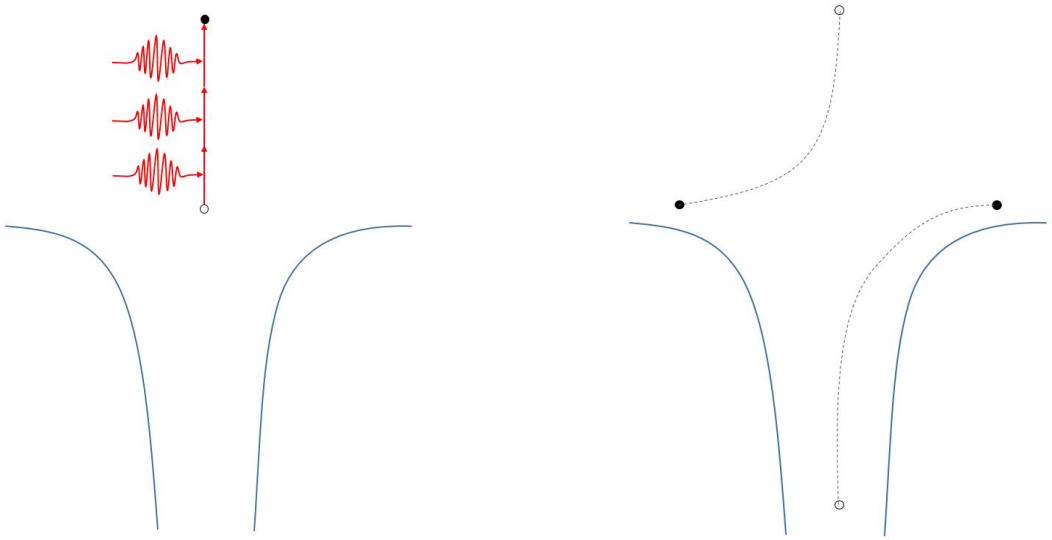

(a) Free carrier absorption

(b) Impact ionisation

Figure 2.3: Avalanche ionisation.

refractive index change. This proposal has been strongly supported by Raman spectroscopy. In the case of fused silica, Raman spectroscopy found an increase in 3 and 4 silica rings, when observing laser exposed regions. The formation of these molecules strongly supports densification of the glass within the laser exposed region [28]. Fluorescence studies have also shown laser writing increases the concentration of non-bridging oxygen hole centres [29]. These colour centres have been shown to have only a minor contribution to the total refractive index change [30–32].

2.4.2 Birefringent refractive index change

At an intermediate writing power selfaligned nanostructures can form in fused silica. The formation of nano structures is dependent on the laser polarisation [33, 34]. The nano structures are aligned perpendicular to the writing polarisation and form periodic gratings with a period of $20 - 140$ nm (Figure 2.4), waveguides written with these nano structures have been found to be birefringent [35, 36].

It is currently suggested that the formation of these nanostructures is caused by an inhomogeneous dielectric break down, resulting in the formation of nano-plasmas. These nano-plasmas forms nano-planes aligned with the polarisation of the incident field [33].

Applications of birefringent laser writing include polarisation sensitive holograms [37], waveguide polarisation splitters [38] and micro-channel fabrication [39].

2.4.3 Voids

At high intensities, a high density plasma is created within the material. If the plasma's pressure is greater than the Young's modulus of the material, a shock wave is formed. This

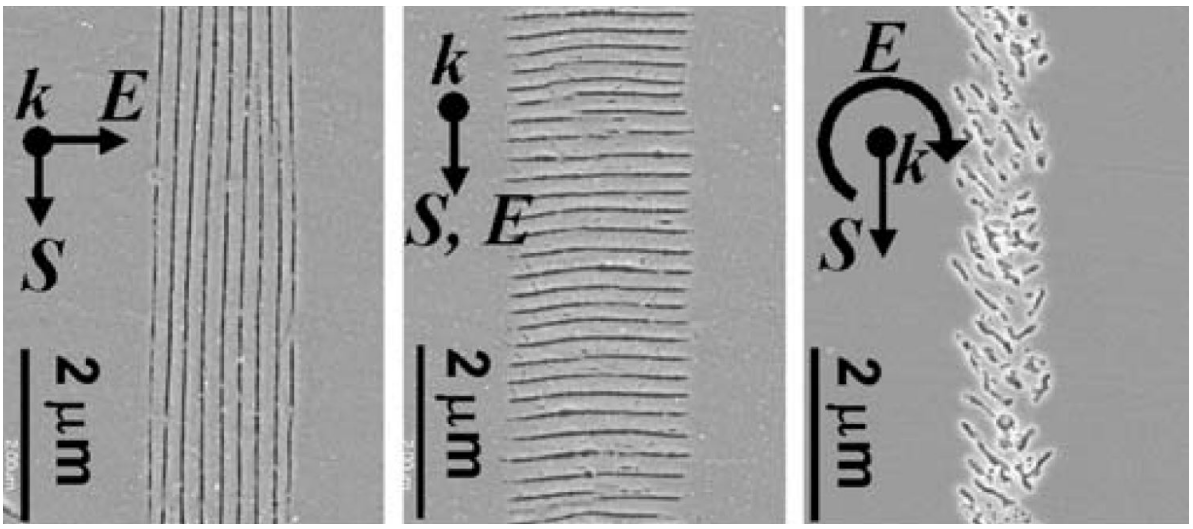

Figure 2.4: Polarization dependent nanostructure formation with the polarization orientation perpendicular (left) and parallel to the writing direction (centre), as well as circular polarisation (right) [33].

shock-wave leaves a less dense or hollow core with a denser surrounding shell. Void formation is readily used for 3D data storage [20], photonic crystal devices [40] and Bragg gratings in bulk glasses and fibres [41, 42].

2.5 Laser repetition rate

In laser direct writing there are two very distinct writing regimes: the low repetition rate (athermal) and high repetition rate (thermal), (Figure 2.5). When writing in the low repetition rate regime the period between each pulse is longer than the thermal diffusion time. Therefore before the next pulse, all the heat from the previous pulse has dissipated away. Consequently each modification must overlap to create a smooth waveguide. This requirement limits the writing speed of a 1 kHz system to below 25 μm/s [44]. Waveguides fabricated using the low repetition rate typically have a highly elliptical cross section. The ellipticity is a result of the focal volume being dependent on the waist of the Gaussian beam and the depth of focus. To inscribe circular waveguides beam shaping techniques are required[2]. Beam shaping is commonly done by introducing astigmatism. Astigmatically shaped beams can be formed by placing a slit in front of an objective [45], or using a cylindrical telescope or via a spatial light modulator [46]. An alternative to beam shaping is the multi-scan technique, in which multiple structures are written slightly offset [47, 48], creating a waveguide of a square or rectangular cross section.

When the time between consecutive pulses drops below the thermal diffusion time, the heat from the previous pulse can not completely diffuse into the material before the next pulse arrives. Therefore after each pulse the temperature at the focal point accumulates,

[2]To efficiently couple light from optical fibres, laser written waveguides must be of a circular cross section.

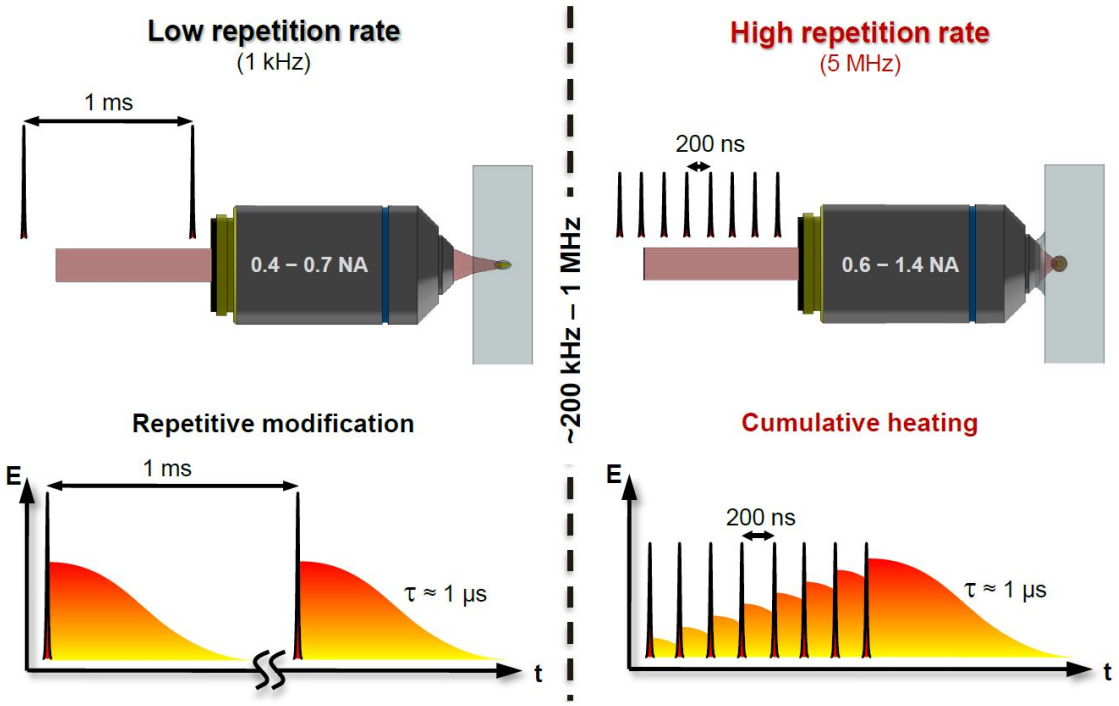

Figure 2.5: Illustration of the low and high repetition rate regimes [43].

resulting in local melting of the material. Once the sample is moved, the melted volume rapidly quenches, leaving a structural modification [27, 49–51]. Thermal diffusion moves symmetrically from the focal point, therefore under the correct writing conditions beam shaping techniques are not required to create circular waveguides in the cumulative writing regime.

Cumulative heating is dependent on the laser intensity and the translation speed. It can be seen that the change from the thermal to cumulative heating can occur over a small translation speed increase or a small pulse energy change as demonstrated in Section 5.2.3.

2.6 Spherical aberrations

Spherical aberrations are due to the refractive index mismatch at the air/glass interface of the sample. These aberrations cause the focal spot to be distorted resulting in a lower peak intensity as well as deforming the shape of the laser written waveguides. Most biological microscope objectives are corrected for aberrations when focusing at 170 μm. However any deviation from this depth causes aberrations to occur. These distortions are more severe for higher NAs. Consequently, there is a fine balance between choosing an objective with an NA large enough to limit the required peak power and hence avoiding self-focusing [3], and

[3]Nonlinear $\chi^{(3)}$ process, high laser intensity induces a non permanent refractive index change. As the laser field is Gaussian the induced refractive index change is greater at the centre than the edges, typically creating a positive lens inside the material.

a small enough NA to avoid large distortions. Spherical aberrations can be mitigated to a large extent by using oil immersion objectives. However these objectives have a limited working distance, of a few hundred microns.

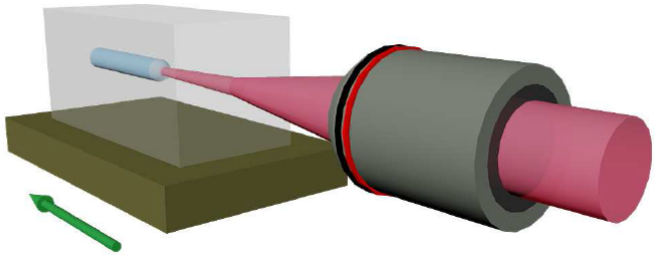

(a) Parallel (longitudinal)

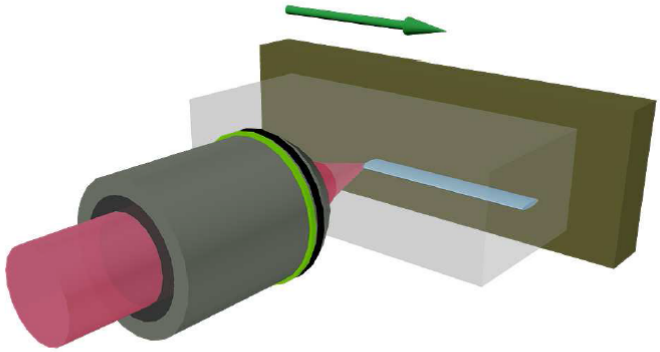

(b) Perpendicular (transverse)

Figure 2.6: Laser writing geometries [52].

2.7 Writing geometry

Figure 2.6 shows two different writing geometries used for laser direct-writing. When writing with the parallel method, the sample is translated parallel to the laser beam. This method produces circular waveguides independent of the NA or repetition rate. However, the length of the waveguides written with the parallel technique is restricted by the working distance of the objective.

Perpendicular writing on the other hand, translates the sample in a perpendicular direction relative to the incident laser beam. This has the advantage that waveguides can be written to any length restricted only by the travel of the stages. However beam shaping is generally required in order to inscribe waveguides of a circular cross section.

NB. parallel and transverse writing suffer from spherical aberrations.

2.8 Fluorescence

Laser writing has been shown to induce non-bridging oxygen hole centres (NBOHCs). These NBOHCs are generated in fused silica during the writing process as the ≡Si−O−Si≡ bond is broken into ≡Si−O (NBOHCs) and Si≡ (positively charged oxygen vacancy (E' centre)) [53]. The NBOHCs have a broad absorption band from 4.8 eV to 2 eV [54] meaning they can be excited at 633 nm by a helium-neon laser to produce a photoluminescence at 650 nm (see Figure 2.7a). NBOHCs are typically unstable in fused silica due to hydrogen reacting with the NBOHCs [55]. To achieve stable fluorescence, the glass must have minimal hydrogen concentration and high OH content to form a large amount of NBOHCs. As photoluminescence intensity is proportional to the propagation power, recording the photoluminescece essentially allows the propagation of light to be visualised. Dreisow *et al.* [56] used this technique to great effect to visualize the propagation of light in fs laser written waveguide arrays as seen in Figure 2.7b. This visualisation method was also explored in this thesis project as a method to evaluate light propagation within slab waveguides.

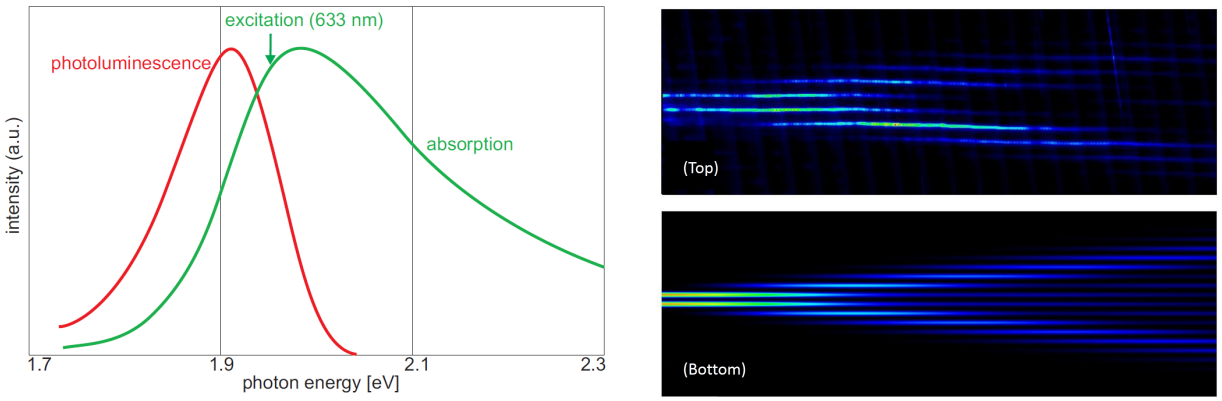

(a) (b)

Figure 2.7: (a) Absorption and emission of NBOHCs in fused silica [56]. (b) Quasi-incoherent double waveguide excitation; the top figure shows the experimental coupling within the waveguide array and the bottom shows the theoretical results for comparison [56].

2.9 Glass substrates

The glass selection is dependent on device application. Properties such as nonlinearity, dopants, fluorescence and transmission all play a role for the material choice. In this work three different glasses were used; Heraeus Suprasil 1, Corning 7980 HPFS and Corning Eagle 2000.

Heraeus Suprasil 1 is a highly pure fused silica with a high OH content $<$ 1000 ppm. This high OH content makes the glass suitable for the fluorescence visualisation techniques as long lived NBOHCs are created during laser writing [56]. Suprasil is an optical grade glass with high index homogeneity 3×10^{-5} and high transmission from 0.2−2 μm. This makes Suprasil a preferred material for optical beam splitters, prisms and interferometry [57]. Corning 7980

HPFS, fused silica with similar OH content to Suprasil was also tested. Corning 7980 HPFS is ordered as pre-polished wafer to an accuracy of $\pm 25 \mu m$, while Suprasil 1, is commerically avaliable as high precision optical slab with approximately the surface accuracy.

Corning Eagle 2000 is an alkaline earth boro-aluminosilicate glass. Eagle 2000 is lightweight, physically robust, inexpensive, chemically durable, has a low thermal expansion coefficient and a high transmission range [58]. Corning Eagle 2000 comes as a sheet glass drawn using Corning's fusion process which has a thickness accuracy of $\pm 10\%$.

Eagle 2000 was shown by Eaton *et al.* [49] to be suitable for waveguide writing and is now a commonly used material for waveguide devices in telecommunications, quantum optics and astronomy [59–61]. However Eagle 2000 has absorption losses due to iron impurities which result in a broad absorption band centered around 1100 nm as shown in Figure 2.8.

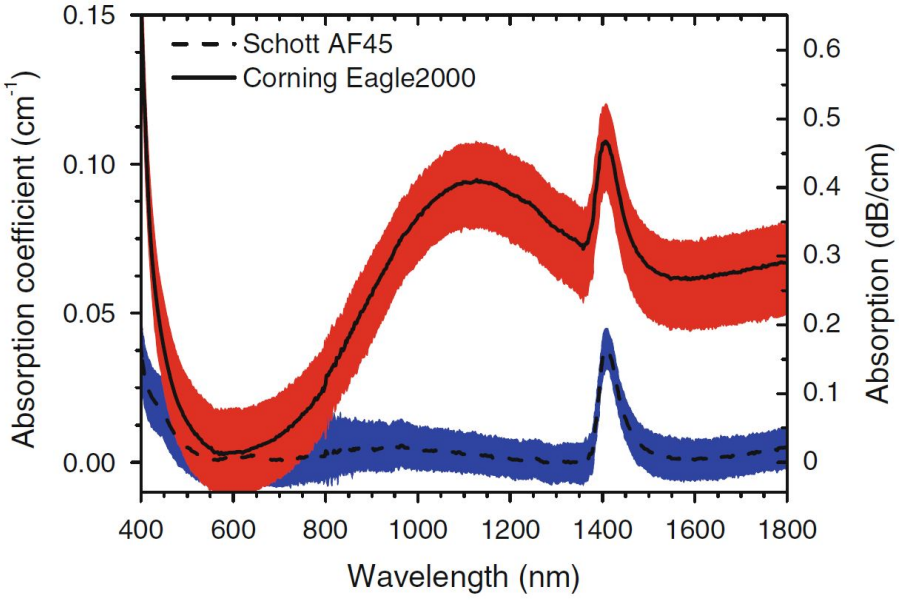

Figure 2.8: Absorption spectra of Corning Eagle-2000 and another multicomonent silica glass (Schott AF45) [60].

2.10 Laser written slab waveguides

The fabrication of slab waveguides is an integral part of this project. Currently there are limited reports on the inscription of uniform broad area slab waveguides using the femtosecond laser direct-write technique. The only two reports on the fabricating of such structures are by Watanabe *et al.* [62] and Ghosh *et al.* [63].

Watanabe *et al.* [62] used an amplified Ti:sapphire laser system producing 85 fs pulses at 1 kHz repetition rate, centred at 800 nm to fabricate a multi-mode interference device (MMI). Using 1.5 μJ pulse energy in fused silica a filamentation occured that was utilised to create 100 μm wide slabs of uniform refractive index change. The filament was scanned at 1 μm/s

in the x direction to create a wide refractive index change. Next the filament was translated 50 μm in the z direction and the process was repeated to create a longer slab. Figure 2.9a shows a schematic of the 30 μm wide and 870 μm long device. The near-field patterns of a MMI device were observed at different wavelengths as illustrated in Figure 2.9b. These results were then compared to simulations as shown in Figure 2.9c. A strong agreement with experimental data was found using a refractive index contrast of 2.0×10^{-3}. The differences were attributed to non-uniformities in the refractive index change caused by the start and end regions of the filament.

Ghosh *et al.* [63] used a Yb-doped fibre laser producing 350 fs pulses, centred at 1064 nm, and a repetition rate of 500 kHz to fabricate a 500 μm wide slab waveguide in erbium-doped bismuthate glass. Using the multi-scan technique, multiple structures were written 0.4 μm apart. The slab was written with 86 nJ pulse energy and a writing speed of 8 mm/s using a 20 x, 0.4 NA objective. The paper gives no detailed analyses of the slab except for stating "The slab waveguide yielded single-mode guidance in the vertical direction and highly multimode guidance in the horizontal direction" [63].

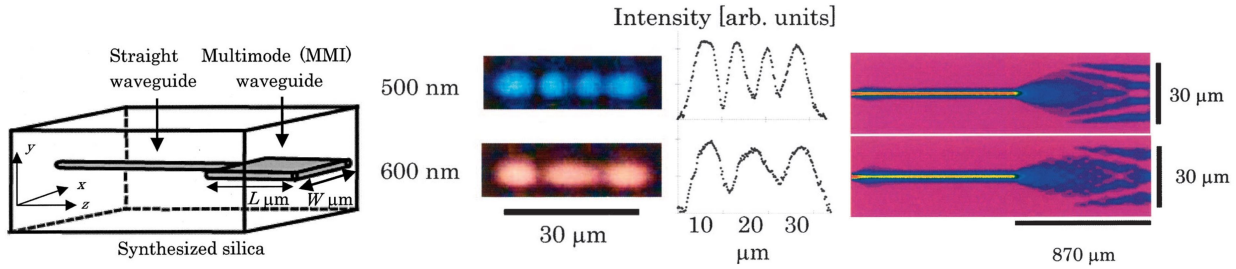

(a) (b) (c)

Figure 2.9: (a) Schematic of the MMI device. (b) Near-field MMI device output at 500 and 600 nm respectively. (c) Simulated intensity propagation at 500 nm (top) and 600 nm (bottom) [62]

3
Photonic Spectrographs

Current spectrograph designs are large, expensive and extremely sensitive to environmental conditions. With the astronomical community beginning to design and construct new extremely large telescopes (ELTs), current spectrographs need to be scaled proportionally to the aperture size. This scaling process is an extremely challenging engineering exercise and costly. It has been suggested that the cost of the instruments will increase as the telescope aperture squared or faster [1]. Instrumentation studies for the European ELT suggest that the cost of a single spectrograph could be between $\$50 - 100$M, approximately the cost of building a current generation telescope [64]. The expense has led astronomers to the relatively young field of astrophotonics. Astrophotonics sits at the interface between photonics and astronomy and uses photonic technologies to solve astronomical instrumentation problems [1, 16, 17, 65–68]. This chapter will focus on the integrated photonic spectrograph (IPS), specifically the arrayed waveguide grating (AWG). The chapter begins by discussing alternative AWG applications other then the telecommunication and astronomical functions addressed in the introduction. This is followed by the design, operation and typical manufacturing techniques.

3.0.1 Alternative AWG applications

Due to their size and characteristics, AWGs have recently been applied to various other applications, including on chip spectral domain optical coherence tomography [69] and minaturised Raman spectroscopy [70]. Recently there has been an increased effort to develop fast, compact spectroscopic sensors for the medical and biological fields. Current compact sensors are based on free space optical systems, meaning they are difficult to miniaturise and are inherently unstable. AWGs have recently been shown to effectively work as a miniaturized spectroscopic sensor with a sub-nanometer wavelength resolution. To measure the spectral transmittance of liquids, AWGs with microfluidic channels were fabricated with a photo-detector directly coupled to the AWG's output [71] (Figure 3.1b). Since commercial

telecommunication AWGs are fabricated with a central wavelength in the near infra-red, the detector range is limited to a region of minimal interest to large parts of the sensing community. Therefore AWGs needed to be developed for the visible, since many materials and analytes have specific markers in this wavelength range. In 2006 K. Suzuki *et al.* [72], developed an AWG with a wavelength range of $400 - 700$ nm. The output of this device can be seen in Figure 3.1a. Using these new visible AWGs, chlorophylls a and b could both be discriminated [73].Thus confirming the potential of AWGs as a compact spectroscopic sensor.

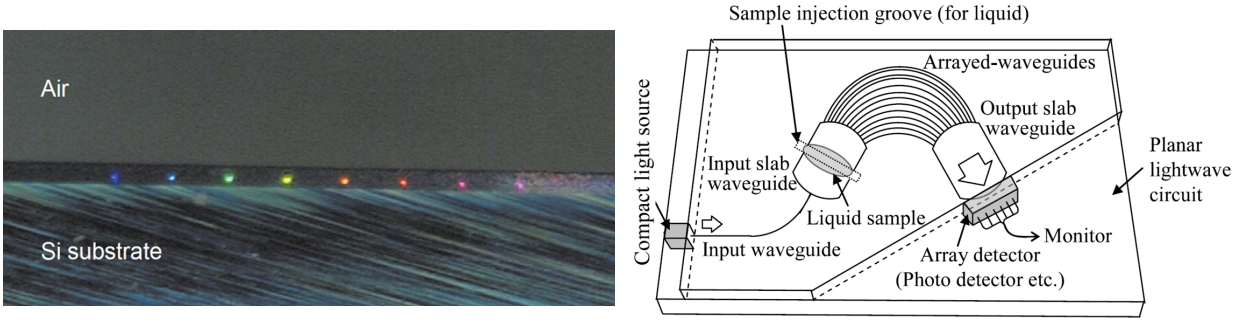

(a) (b)

Figure 3.1: (a) A microscope image of the eight output ports of a AWG for the visible [72]. (b) Sketch of an AWG spectroscopic sensor [73].

AWGs have also recently been demonstrated for use as integrated optical tweezers. Using the focused output of the AWG a particle can be trapped and moved. Figure 3.2a shows how a groove has been added at the focal position in the second slab. In this groove particles within a solution can be added. When a single wavelength is injected into the AWG, a particle can be trapped at the re-imaged focus. Figure 3.2b demonstrates that once a particle is trapped, the wavelength can be altered and as such moving the trapped particles. Several particles can be independently manipulated by using a wavelength division multiplexed light source [74]. This technique allows trapped particles to be easily evaluated at different wavelengths and easily moved.

3.1 Arrayed Waveguide Grating fundamentals

As illustrated in Figure 3.3, AWGs consist of an input taper (Section 3.1.1), an input/ output free propagation zone (FPZ)[1] (Section 3.1.2), a FPZ/waveguide array transition (Section 3.2) and a waveguide array (Section 3.2.1). The basic principle of operation is as follows: Light injected into the first FPZ freely diffracts within the smooth uniform refractive index slab. At the end of the first FPZ the divergent light is captured by an array of individual single mode waveguides. Light is then individually guided in each waveguide of this array. The waveguide array then outputs into a second FPZ where light constructively interferes at the output.

[1]Commonly known as star couplers or slab regions

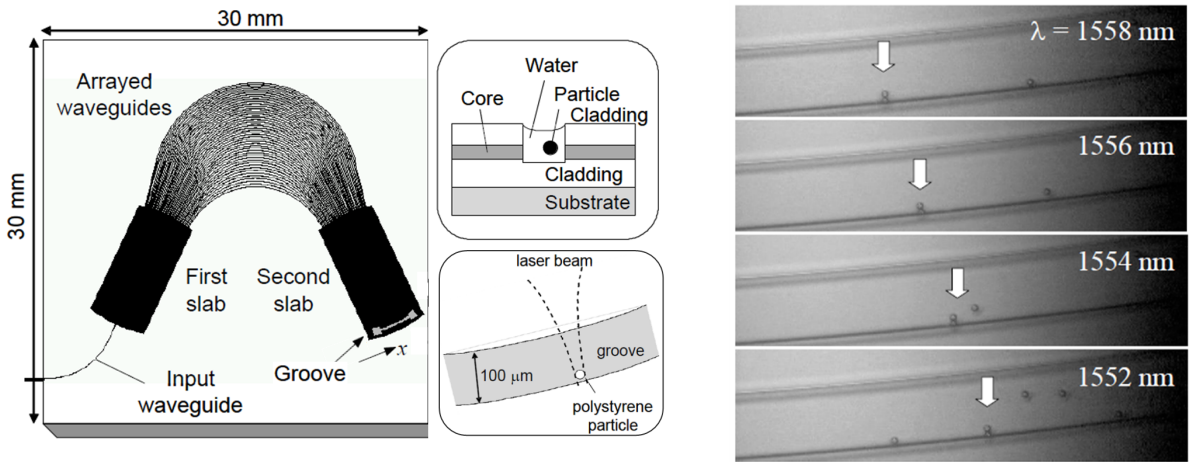

(a) (b)

Figure 3.2: (a) Sketch of an AWG for integrated optical tweezers. (b) Displacement of a trapped polystyrene particle by varying the trapping wavelength [74].

3.1.1 Waveguide tapers

For typical AWG applications the output of the second FPZ is captured by a series of output waveguides. Each waveguide is designed to couple a specific channel of a certain wavelength. However, if there is a small wavelength shift or device fault, the output position of this channel can move laterally. Any small shift in the output could completely remove, or reduce, the throughput of a specific channel, or the device as a whole. To ensure misalignments do not reduce channel throughput, designs have been introduced that physically broaden the focal spot at the output.

One approach is to create a flat top intensity distribution at the start of the input FPZ. Since an AWG acts as an imaging device, a flat intensity response is reproduced at the output. A flat output field can be created using a parabolic-horn (waveguide) taper [75] (Figure 3.4) or a 1×2 multi-mode interference coupler [76]. Another approach is to design a flat electric field output while maintaining a Gaussian electric field at the input. This can be achieved in two ways. If the waveguide array has a *sinc*-shaped electric field profile. The output field will be flat because the FPZ Fourier transforms the electric field [77]. Alternatively if the output is made to have two focal spots slightly offset, but partially overlap to form a broader peak [78]. This can be achieved by fabricating input and output star couplers with two interleaved slightly offset circular arcs of the same curvature.

Since the techniques mentioned above reduce the spectral resolution [15], they are only utilised in applications that split light into specified optical channels.

3.1.2 FPZ

The two FPZs used in an AWG are based on a star coupler. Star couplers are regularly used in optical networks to evenly distribute an input signal to multiple receivers. When light is injected into a single input, the light diffracts in the slab and is evenly coupled to

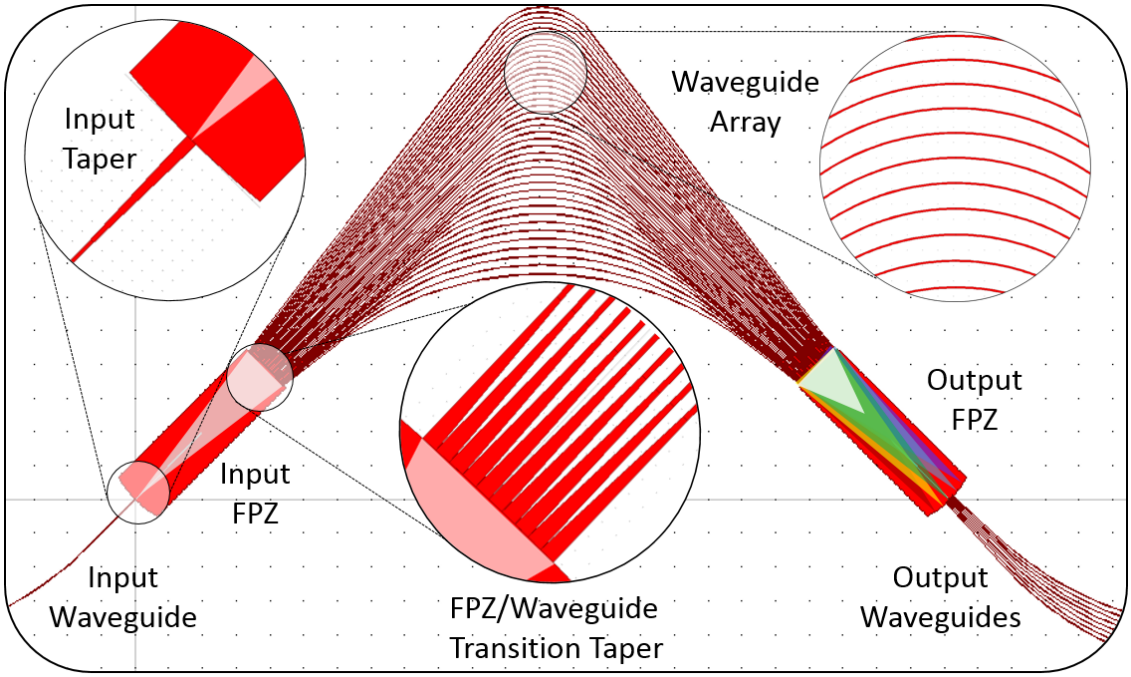

Figure 3.3: Schematic of an arrayed waveguide grating.

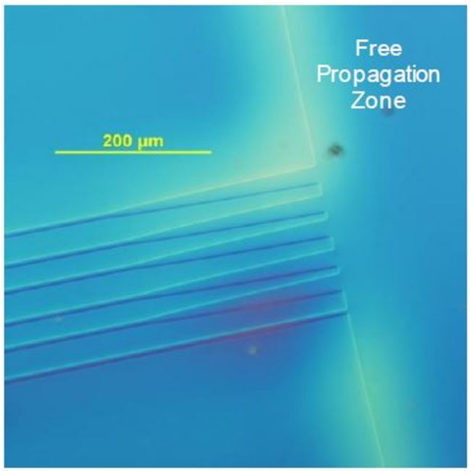

(a)

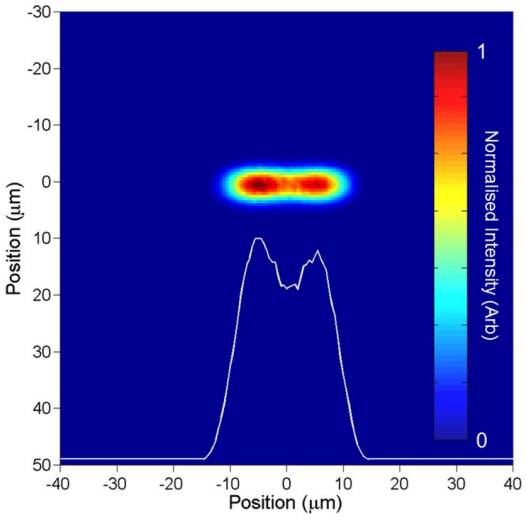

(b)

Figure 3.4: (a) A linear adiabatic planar taper of the input of a commercial AWG. (b) Intensity profile at the output for a parabolic input waveguide [15].

the output waveguides, independent of the position of the input waveguide. Alternatively light interferes when it is coherently injected into multiple input ports. By adjusting the input phase of the incident field, light can be directed to the desired output. In this thesis AWGs are fabricated using FPZs with a Rowland circle geometry. This means that the input

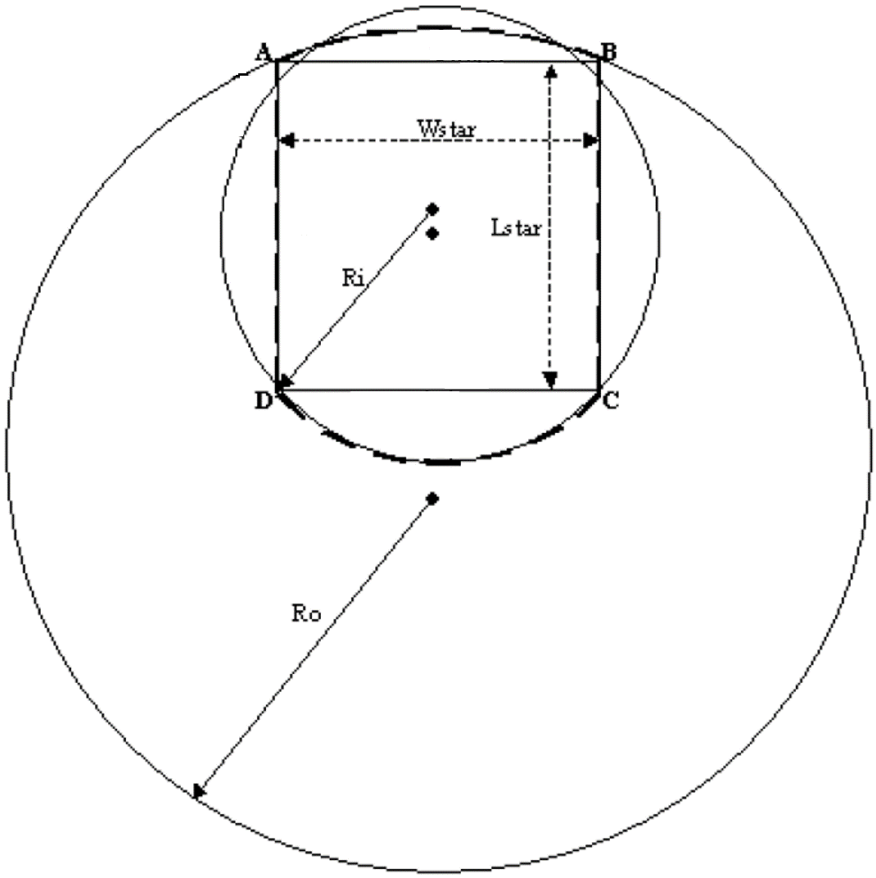

Figure 3.5: Rowland circle geometry of a star coupler. The body of the star coupler is formed between ARC AB & ARC CD. L_{star} and W_{star} define the length and width of the star coupler [79].

and output ends of both FPZs are curved. This curvature is designed so that light injected into the FPZ at any position is captured in phase by the waveguide array and the output interference is captured at the curved FPZ output. The geometry of a Rowland circle FPZ can be seen in Figure 3.5. Light is input into the arc swept by R_i and is collected by the waveguide array on an arc swept by R_o. For the output FPZ the design is identical except incident and output arcs are reversed.

The Rowland curvature can be calculated using the the wavelength dispersion discussed mathematically later in appendix A.1. Essentially this equation can be used to calculate how long the FPZ needs to be for light to be able to disperse wide enough to be captured by all the waveguide at the output of the FPZ. The input radius is then defined as half R_o.

3.2 FPZ/waveguide transition taper

At the interface between the FPZ and the waveguide array it is not practically possible to completely capture the whole diffracted Gaussian field, as the decive becomes to large. The waveguide array is designed to capture the Gaussian field up to its $1/e^2$ intensity. This ensures that a majority of the light field is collected while maintainng a resonable waveguide array size. A major source of loss in an AWG is the mode profile mismatch between the FPZ and the waveguide array. At the end of the FPZ the intensity profile is a broad Gaussian. This Gaussian field needs to be adiabatically converted into the waveguide array, otherwise the mode mismatch would result in excessive losses. Several techniques have been proposed and utilised to reduce the losses at this interface.

Initially, planar linear and parabolic tapers were used to reduce the losses at the transition. These techniques are simple and easy to manufacture but lack efficiency.

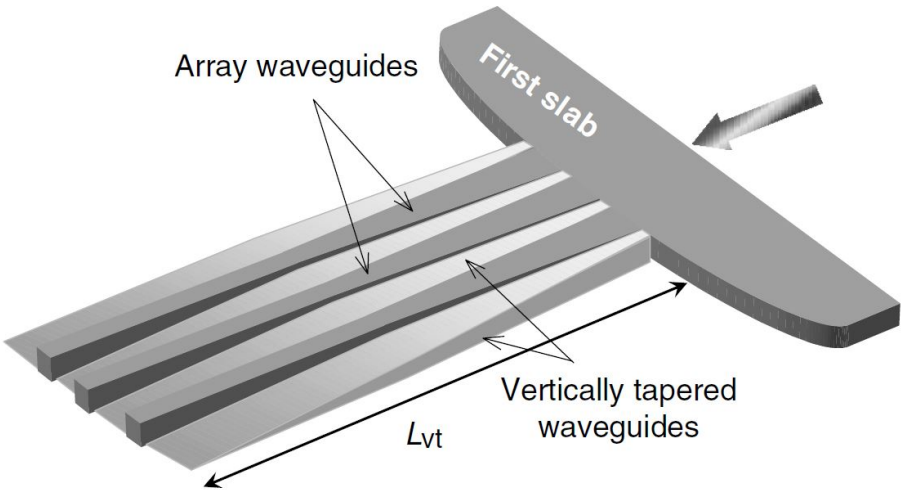

Figure 3.6: Vertical tapers are positioned between the array waveguides and taper vertically over a length L_{vt} which is typically $500 - 1000$ μm [80].

One of the most efficient adiabatic taper techniques is the complex vertical taper technique [81, 82], (Figure 3.6). Vertical tapers can be fabricated by photo-lithography and etching. However, due to the inherit complexity a less efficient but more simple taper technique called segmentation is commonly used [83]. Segmentation adds sections perpendicular to the waveguides. The width of these sections decrease as they become further away from the FPZ (Figure 3.7). Since the segments are smaller than the FPZs Gaussian mode, the segments create an effective refractive index that slowly alters the mode to resemble the acceptance mode of the waveguide array. More recently, efficient non-adiabatic planer waveguide tapers have been proposed that can reduce the required taper length [84].

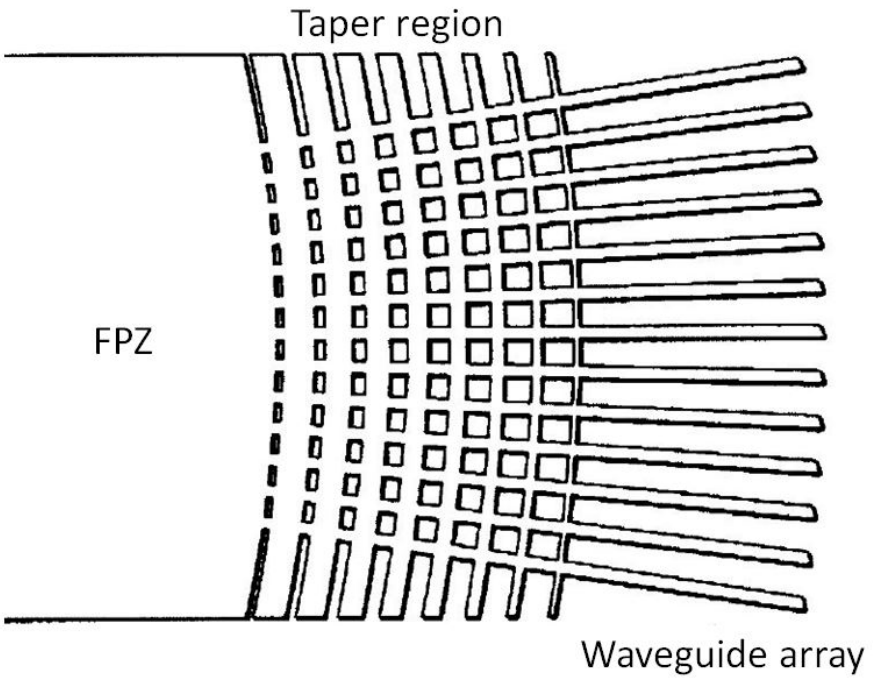

Figure 3.7: Segmentation taper positioned at the FPZ-waveguide array transition.

3.2.1 Waveguide array

Each waveguide in the waveguide array is incrementally longer than the previous waveguide, Therefore the waveguide array is analogous to a diffraction grating. Each waveguide is phase delayed, causing multiple point sources that interfere. Like in gratings, each wavelength has a different phase front tilt after passing through the waveguide array, resulting in a dispersed spectrum to be formed at the FPZ output. For telecommunication applications each individual wavelength channel is coupled into a series of output waveguides for WDM. For spectrographic applications these waveguides can be removed to capture just the dispersed spectrum.

The path length difference ΔL between the waveguides of the array is chosen to be an integer multiple of the central operating wavelength,

$$\Delta L = \frac{m\lambda_0}{n_a} \tag{3.1}$$

where m is the diffraction order, λ_0 is the central operating wavelength of the device and n_a is the effective index of the waveguide array. When light at the central wavelength propagates through the waveguide array all the waveguides have the same relative phase. However at different wavelengths the path length difference causes a phase front tilt. As a result, different wavelengths are focused at different offset positions with respect to the central wavelength. Figure 3.3 graphically demonstrates an exaggerated concept of this wavelength effect.

3.2.2 Phase matching

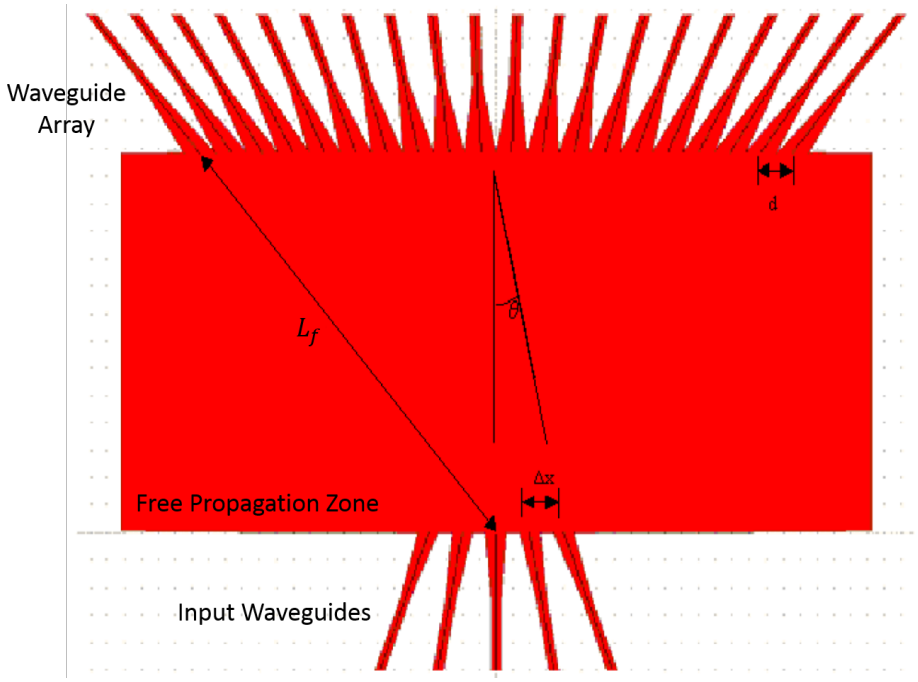

Figure 3.8: Basic free propagation zone design. Light enters from the input waveguides at the bottom of the image and propagates up through the FPZ, it then couples into the waveguide array. The design of the output FPZ is identical but the light propagation direction is reversed [79].

Figure 3.8 shows the geometry of a FPZ. Based on their structure a phase matching equation can be calculated [85] as

$$n_s d sin(\theta_i) + n_a \Delta L + n_s d sin\,(\theta_o) = m\lambda, \tag{3.2}$$

where,

$$\theta_i = i\frac{\Delta x}{L_f}, \tag{3.3}$$

$$\theta_j = j\frac{\Delta x}{L_f}, \tag{3.4}$$

with n_s being the effective index of the FPZ slab, d is the array waveguide separation, i is the number of the input waveguide, j is the number of the output waveguide, Δx is the separation of the input waveguides, and L_f is the focal length of the star coupler.

3.2.3 Angular and linear dispersion

By differentiating Eq. (3.2) with respect to λ the angular dispersion can be calculated. Since the FPZ is large compared to d and Δx, it can be assumed that $\theta_i \approx \theta_o = 0$. Therefore

$$m = n_s d\frac{d\theta_o}{d\lambda} + \frac{dn_a}{d\lambda}\Delta L. \tag{3.5}$$

Substituting ΔL at the centre wavelength λ_0 gives,

$$m = n_s d\frac{d\theta_o}{d\lambda} + \frac{dn_a}{d\lambda}\frac{m\lambda_0}{n_a} \tag{3.6}$$

which can be re arranged to give,

$$\frac{d\theta_o}{d\lambda} = \frac{m}{dn_s}\left(1 - \frac{\lambda_0}{n_a}\frac{dn_a}{d\lambda}\right) \tag{3.7}$$

giving the wavelength dispersion relation,

$$\frac{d\theta_o}{d\lambda} = \frac{mn_g}{dn_s n_a} \tag{3.8}$$

where n_g is the group refractive index is,

$$n_g = n_a - \lambda_0\frac{dn_a}{d\lambda}. \tag{3.9}$$

Rewriting the dispersion relation in terms of frequency,

$$df = \frac{-c^2}{\lambda}d\lambda \tag{3.10}$$

$$\frac{d\theta_o}{df} = \frac{m\lambda^2 n_g}{cdn_s n_a} \tag{3.11}$$

Equations (3.8) and (3.11) give us the dispersion relation in terms of wavelength and frequency. Using the dispersion relation and the geometry of the FPZ, the output waveguide spacing in terms of wavelength and frequency can be calculated:

$$\Delta\lambda = \frac{\Delta x}{L_f}\frac{d\lambda}{d\theta_o} = \frac{\Delta x d n_s n_a}{L_f m n_g} \tag{3.12}$$

$$\Delta f = \frac{\Delta x}{L_f}\frac{df}{d\theta_o} = \frac{\Delta x dc n_s n_a}{L_f m n_g \lambda^2} \tag{3.13}$$

3.2.4 Free spectral range

The free spectral range (FSR) is defined as the frequency spacing between grating orders. When designing an AWG, the FSR needs to be equal or larger than the frequency spacing of the channels multiplied by the number of channels. If an AWG is designed with the $FSR = \Delta f \times \#\ \ of\ output\ ports$ and for the order $m+1$ channel, Equation (3.2) can be modified to [85, 86]

$$(n_s + \Delta_s)\, dsin\theta_i + (n_c + \Delta n_c)\,\Delta L + (n_s + \Delta n_s)\, dsin\theta_o = (m+1)\,\frac{c}{f + FSR} \tag{3.14}$$

where $n_s + \Delta n_s$ and $n_c + \Delta n_c$ are the effective refractive indexes at the frequency of $f+FSR$ of the slab and channel waveguides, respectively. The index change is approximately given by the following equations.

$$\Delta n_c = \frac{dn_c}{df} FSR = -\frac{c}{f^2} \frac{dn_c}{d\lambda} FSR \tag{3.15}$$

$$\Delta n_s = \frac{dn_s}{df} FSR = -\frac{c}{f^2} \frac{dn_s}{d\lambda} FSR \tag{3.16}$$

Eq. (3.14) can be solved by adding (3.15),(3.16) and (3.2), and using the assumption that the free spectral range is much smaller then the frequency $f(f + FSR) = f^2$ and

$$n_g \approx n_s - \lambda \frac{dn_s}{d\lambda} \quad \text{for} \quad \Delta L \gg d(sin\theta_i + sin\theta_o) \tag{3.17}$$

we get the relation:

$$FSR = \frac{c}{n_g \left(\Delta L + dsin\theta_i + dsin\theta_o\right)} \text{ [Hz]} \tag{3.18}$$

For the diagonal ports where $\theta_i + \theta_o = 0$:

$$FSR = \frac{c}{n_g \Delta L} \text{[Hz]} \tag{3.19}$$

Using Equation (3.10) this can be expressed in terms of wavelength:

$$FSR = \frac{\lambda}{m} \frac{n_a}{n_g} \text{[m]} \tag{3.20}$$

3.2.5 Resolving power

The spectral resolution (R) of a spectrograph is a measure of the spectrograph's ability to resolve two different wavelength separated by a small amount $\Delta\lambda$. An AWG is equivalent to a grating spectrometer, therefore the same diffraction limited equation can be used. In this case the number of illuminated grooves actually corresponds to the number of guiding waveguides. Hence the spectral resolution R is given as

$$R = \frac{\lambda}{\Delta\lambda} = \frac{mN}{C}, \tag{3.21}$$

where N is the number of waveguides in the array, m is the order and C is a factor that accounts for imperfections in fabrication, such as path length errors. In the case of lithographically fabricated devices without parabolic taper horns a typical value for C is 1.6 [87].

3.2.6 Alternative AWG types

The AWG design described previously has the output focused onto the Rowland curvature. Another possibility is to focus the AWG's output onto a flat focal field, an example of this design can be seen in Figure 3.9a. A flat focal field is possible using the AWG aberration theory [88]. By introducing three stigmatic points a flat focal field AWG can be created. This is achieved by altering the waveguide array radius, spacing and length. As shown in Figure 3.9b, flat focal field AWGs have reduced wavelength aberrations compared to the conventional Rowland type AWG. This is because typical Rowland type AWGs are only fabricated to remove up to second order aberrations. However higher order aberrations such as coma and spherical are still present and can be reduced by adding stigmatic points. Flat focal field AWGs also have the advantage of easily functioning as a spectrograph. By polishing the end face a photodectector can be directly bounded to the output for recording the output spectrum. S. Lu *et al.* [89] developed the first flat-field AWG in 2005 using an electron-beam direct write technique in epoxy. Due to high crosstalk and insertion losses, the feasibility of flat focal field AWGs are currently limited. An alternative method to create a flat focal field is to use a field flattening lens placed inside the second FPZ. This method was successfully demonstrated by B. Akca *et al.* [90] in 2012.

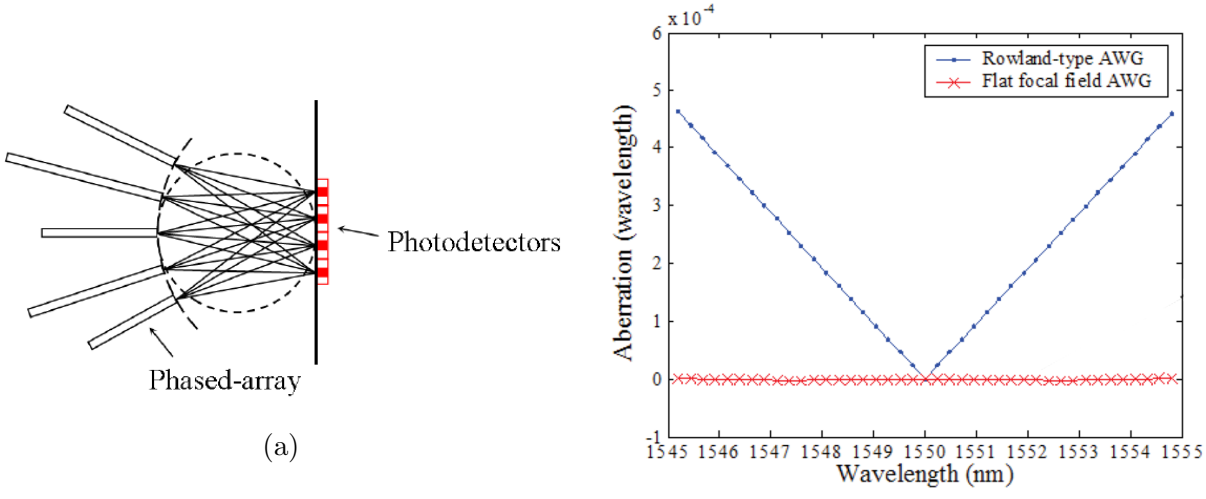

(a) (b)

Figure 3.9: (a) Output of a flat focal field AWG directly coupled to a photodetector. (b) Aberration curve of a polymeric four channel 400Ghz spacing flat focal field AWG compared with a Rowland circle type AWG [89].

Another type of AWG is known as the MMI-AWG [86]. In MMI-AWGs, both star couplers are replaced with MMI couplers. These devices exploit self imaging to split the power into the arrayed waveguides. Such devices are not suitable for low loss spectrographs.

3.3 AWG fabrication

Commercial AWGs are manufactured using photolithography. Photolithography uses light to transfer a device design from a photomask onto a light sensitive photoresist placed on a substrate.

Mask manufacturing Lithographic photomasks are typically fused silica covered with an opaque film of chrome metal. The chrome layer is covered with a photoresist resin, the device design is then written into the photoresist resin using an electron beam. The photoresist is then developed and etched. This etching transfers the device design into the opaque film, leaving a 1:1 image of the device layout. The accuracy of the mask is extremely important as it directly corresponds to the accuracy of the device. Due to this fact, the fabrication of the photomask is the most expensive part of the manufacturing process. A single high quality mask can cost €$10 - 15$ k, while the wafer imprinting only costs € $\approx 5 - 10$ k, with each wafer containing multiple AWGs. The high initial cost of mask manufacturing makes the use of photolithography for one off devices extremely expensive. However, the mask can be used multiple times making it suitable for mass manufacturing.

Chip manufacturing For the device a wafer is used as a substrate. This substrate (typically silicon) acts as a physical surface onto which the actual guiding materials is deposited. The composition of the guiding layers depends on the required wavelength and index change. Refer to Figure 3.10 for a graphical representation of the following manufacturing process. For commercial AWGs.

Initially pure silica is deposited using flame hydrolysis deposition, this layer acts as the undercladding. Next a layer of germanium doped silica is deposited in the same way to act as the core. The germanium increases the refractive index and makes the material sensitive to etching. A photoresist is then applied and the photomask is aligned with the wafer. The mask and wafer are exposed to UV light, removing any photoresist not covered by the mask. The mask is removed and the exposed core layer is etched away using reactive ion etching. The photoresist is then removed. Finally the upper cladding is deposited. Deposition of this final layer is problematic, as deposition is not uniform especially at the edges of the structure. To solve this issue, the wafer is heated so the material can flow and deposit evenly around the core structures. To prevent the whole structure from melting during this process the cladding material is doped to reduce the softening point. This enables the material to flow before the core and undercladding melt. In some cases this doping can cause the top cladding to have a slightly different refractive index, then the undercladding.

3.3.1 AWG fabrication errors

Even with the great care taken to fabricate the AWGs to a high precision, unavoidable processing errors result in fluctuations of the effective index and width of individual waveguide which results in phase errors. To measure the phase errors of each waveguide a Fourier transformation of an optical low coherent interferometer can be used [92]. A simpler but more destructive method to measure the phase errors is to remove the output FPZ. This method however is only effective for free space AWGs [93] (see Figure 3.11a). Using this phase information, AWGs fabricated using a photosensitive germanium doped silica can be UV trimmed. UV trimming translates a focused UV spot along a waveguide within the

waveguide array to finely adjust the refractive index by 1×10^{-3} in order to correct for the phase error [94] (see Figure 3.11b).

The fundamental mode contains two orthogonally polarised components, the TE and TM modes. For perfectly symmetric waveguides the propagation constant of the two orthogonal components are identical, however fabrication errors and stress introduce birefringence. The stress induced birefringence ranges from $\Delta n = 10^{-4}$ to 10^{-3}, depending on the material composition, deposition conditions and processing [95]. To reduce the stress birefringence devices have been fabricated on a silica substrate and half-wave plates have been inserted into the middle of the waveguide array [96]. A recent and more elegant approach has been demonstrated using an angled star coupler [97]. Figure 3.12 shows the measured spectra of a uncompensated and angle compensated AWG.

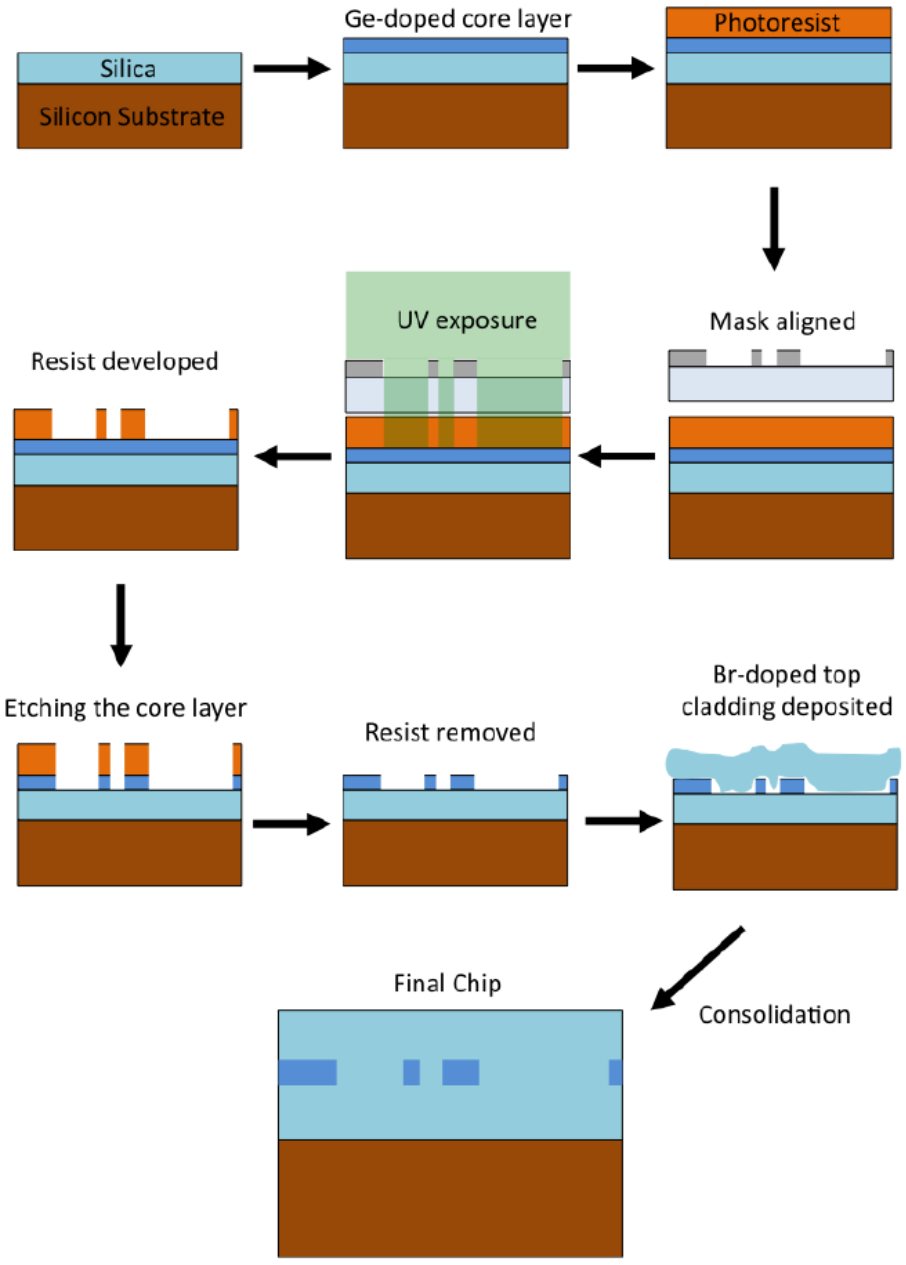

Figure 3.10: Photolithographic fabrication process for planar waveguide devices [91].

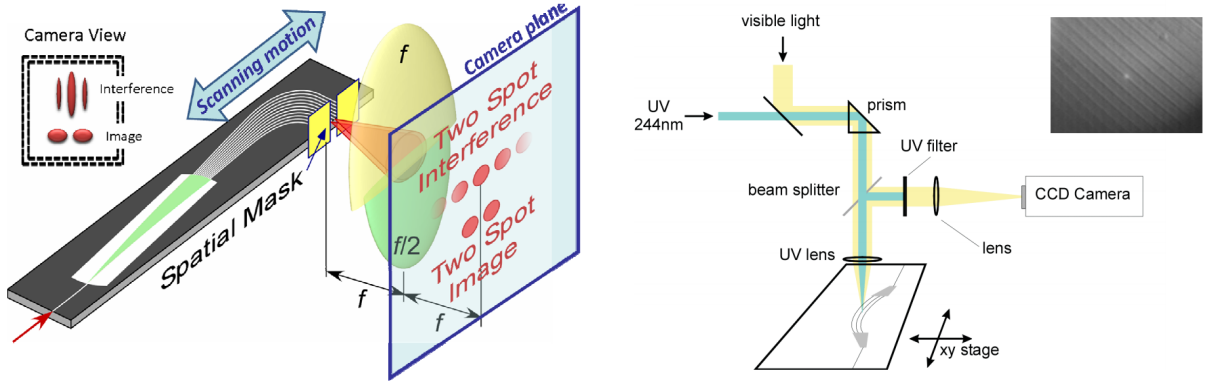

(a) (b)

Figure 3.11: (a) Layout of a free space error evaluation system. A slit is placed at the AWG output blocking all except for two adjacent waveguides. The slit is then scanned to measure all the waveguide pairs [93]. (b) Experimental set-up of the UV trimming procedure [94]. UV light is focused onto the waveguides in the array enabling fine adjustment of the refractive index to correct for phase errors.

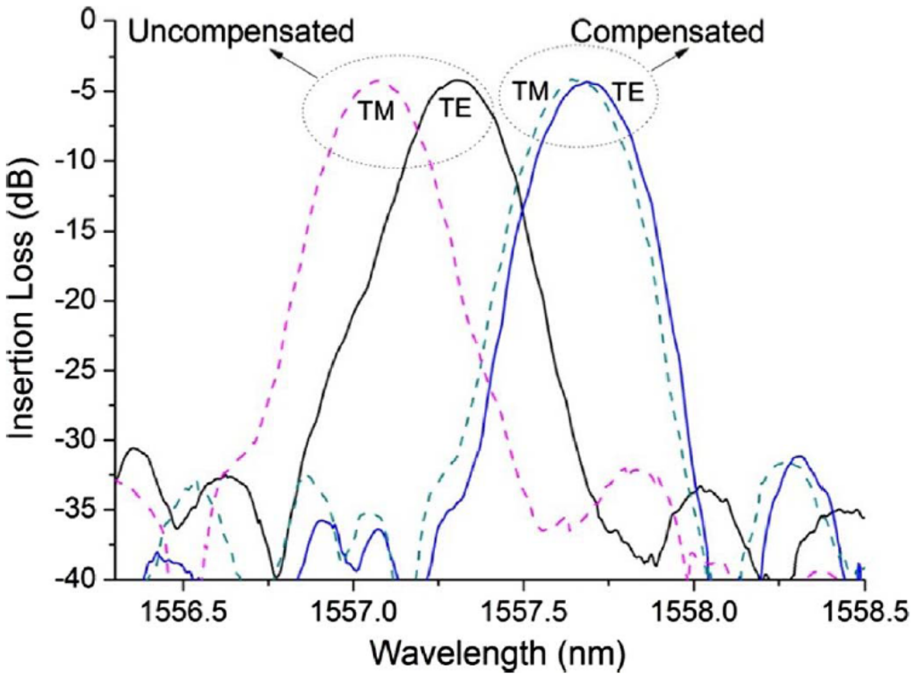

Figure 3.12: Measured spectra of birefringent AWG compared to a birefringence compensated AWG using an angled star coupler [97].

4
Experimental Methods

This chapter outlines the laser fabrication process. Explaining how the pre-existing laser set-up, post processing and the optical visualisation tools are used to fabricate and characterise these devices. Finally the software personally used to design AWGs is discussed.

4.1 Laser Writing Setup

The fabrication setup consists of 3 main parts, the laser, the beam path and finally the translation stages.

4.1.1 Laser

The fabrication system is built around a commercial mode-locked titanium doped sapphire (Ti:sapphire) femtosecond oscillator (FEMTOSOURCE XL500, Femtolasers GmbH, Vienna, Austria). Compared to a standard femtosecond laser which produces 10s of nJ of pulse energy at a repetition rate of 80–100 MHz, the chirped pulsed oscillator emits 550 nJ pulses with a repetition rate of 5.1 MHz and a pulse duration less then 50 fs. To increase the pulse energy the cavity length is increased, decreasing the repetition rate while maintaining the average power [98]. As a result, the increased cavity peak power induces non-linearities, such as self-phase modulation causing pulse collapse, multi-pulsing and increased pulse noise [99]. To overcome this the cavity is operated in a positive dispersion regime [100]. By chirping the intra-cavity pulse, the peak pulse energy is reduced as the pulse is stretched. The positive dispersion creates a dissipative soliton [101], which produces a characteristic output spectrum of rectangular shape as seen in Figure 4.2.

The optical cavity layout is shown in Figure 4.1. A diode pumped intra-cavity frequency doubled continuous wave (CW) Nd:YVO_4 laser (Spectra Physics Millennia XV) operating at 12.2 W pumps a Ti:sapphire (Ti:AL_2O_3) crystal inside the x-folded cavity. Ti:sapphire

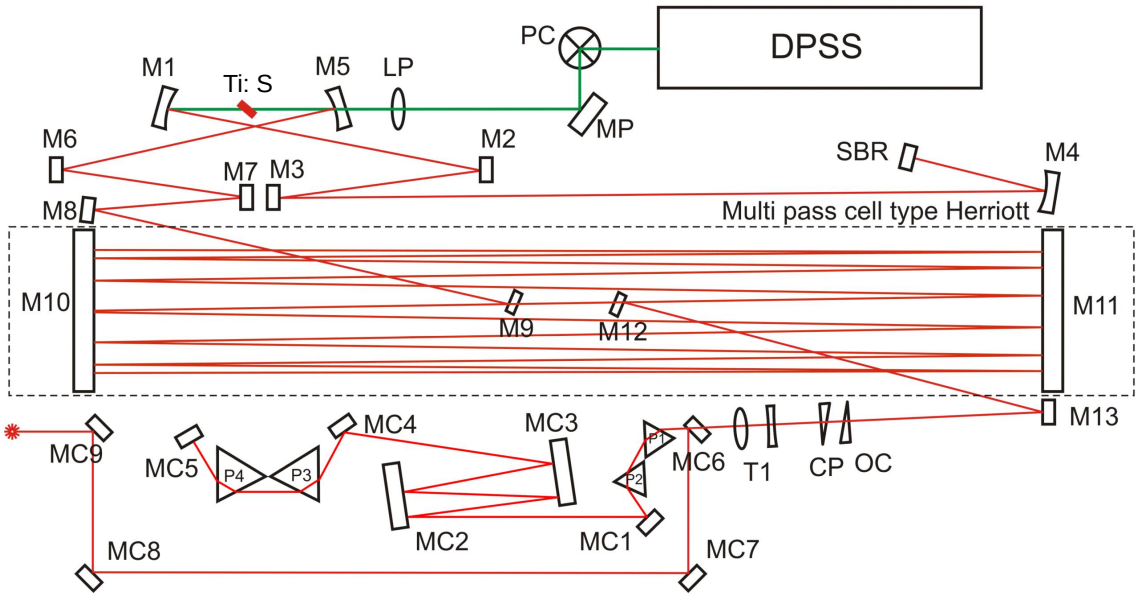

Figure 4.1: Schematic of the Ti:sapphire FEMTOSOURCE XL500. DPSS - diode pump laser, Ti:S - laser crystal,M# - Mirrors, SBR - saturable Bragg reflector (image courtesy of Femtolasers GmbH).

is used for the generation of ultra short pulses due to its large gain bandwidth centred at 800 nm. Due to the high pump power, the crystal is thermoelectrically cooled to -25° to reduce thermal lensing. In the short arm of the x-folded cavity a saturable Bragg-reflector passively mode-locks the laser at high pulse energies [102]. The other arm includes a Herriott multipass cell (MPC)[1] that increases the total cavity length to 30 m. Chirped mirrors are used within the cavity to make the laser operate in a positive dispersion regime[2]. To correct for the positive dispersion a pulse compressor with a negative group dispersion compresses the pulses after the cavity. This is achieved by using 2 prism pairs with a separation of 1.2 m [104]. The second pair of prisms can be translated in and out of the beam path, allowing for fine adjustment of the output pulse duration. The typical output spectrum and corresponding interferometric autocorrelation are shown in Figure 4.2.

4.1.2 Beam path

The beam path is shown in Figure 4.3. After the laser, the beam passes through an Aerotech ADR75 motorised rotation stage. This rotation stage contains a 800 nm half-wave plate.

[1]MPCs are designed to increase the cavity length while maintaining the cavity mode size. This is accomplished by using two mirrors with an ABCD transfer matrix of unity [103]. The beam is reflected 12 times off each mirror in a circular pattern.

[2]Chirped mirrors are comprised of layers designed to reflect different wavelength at different depth. Light reflected from a lower layer travels a longer distance and thus chirping the pulse.

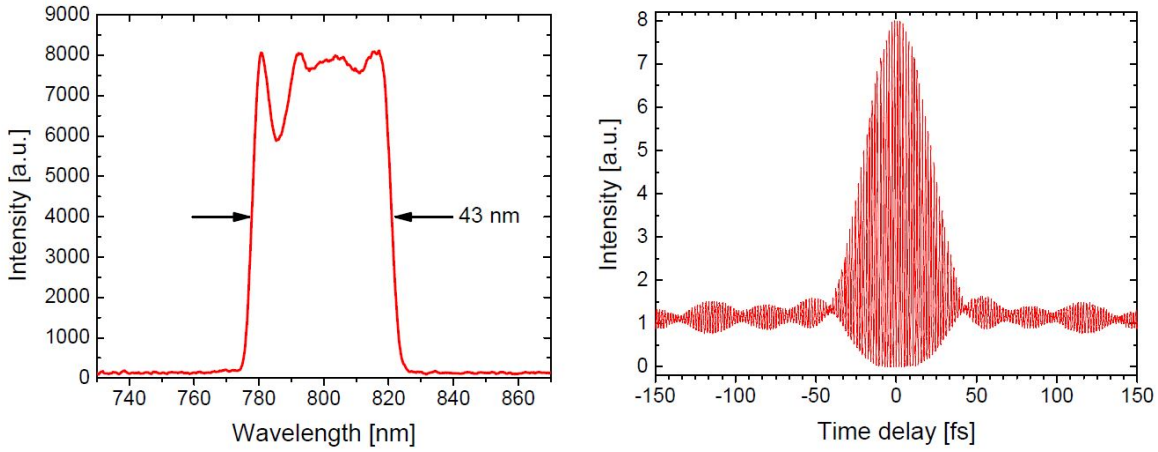

Figure 4.2: Output spectrum of the CPO and the corresponding interferometric autocorrelation. The pulses are *sinc*-shaped due to the rectangular spectrum [43].

Two polarising beam splitters used in reflection then act as a periscope to reduce the beam height to 50 mm. The combination of the rotatable half-wave plate and the two polarising beam splitters creates a variable attenuator. The beam is then directed by a 45° turning mirror into a 2:1 beam contractor which is used to reduce the beam size before passing through a Pockels cell (Section 4.1.3).

Once the beam has passed through the Pockels cell a beam expander is used to adjust the beam size. Depending on the material or device to be fabricated, different pre-aligned magnification ratios (1:2, 2.5, 3, 3.5, 4, 5) can be used to adjust the beam sizes between 2–5 mm. By changing the beam size the effective numerical aperture of the focusing objective can be adjusted. For the majority of this work the 1:5 telescope was used.

The beam is then transmitted through another half-wave plate and a polarising beam splitter. The half-wave plate can be adjusted to allow the beam to pass straight through the polarising beam splitter cube or to be reflected onto a safety screen, depending on whether a voltage is applied across the Pockels cell or not. Light that is allowed to go through the polarising beam splitter cube is directed onto a turning mirror. The turning mirror is positioned on a removable magnetic base. By removing the turning mirror, light enters an interferometric autocorrelator, allowing the pulse duration to be measured. With the turning mirror in position the beam passes through a second iris and a quarter wave-plate. The iris is the main alignment reference for setting the beam perpendicular to the translation stage plane and aligning the focusing objective. While the quater wave-plate changes the beams polarisation to circular. Circular polarisation is used as it gives a higher photoionisation rate and avoids nanograting formation [44].

A periscope is used to increase the beam height and direct light across to a dichroic 45° turning mirror positioned directly above the translation stages. A CCD beam profiler and a power meter are used to measure the beam profile and the average power,they are placed between the periscope and the dichroic mirror. The dichroic mirror is reflective for the laser wavelength and transmissive in the visible, thus allowing a vision system to be placed above

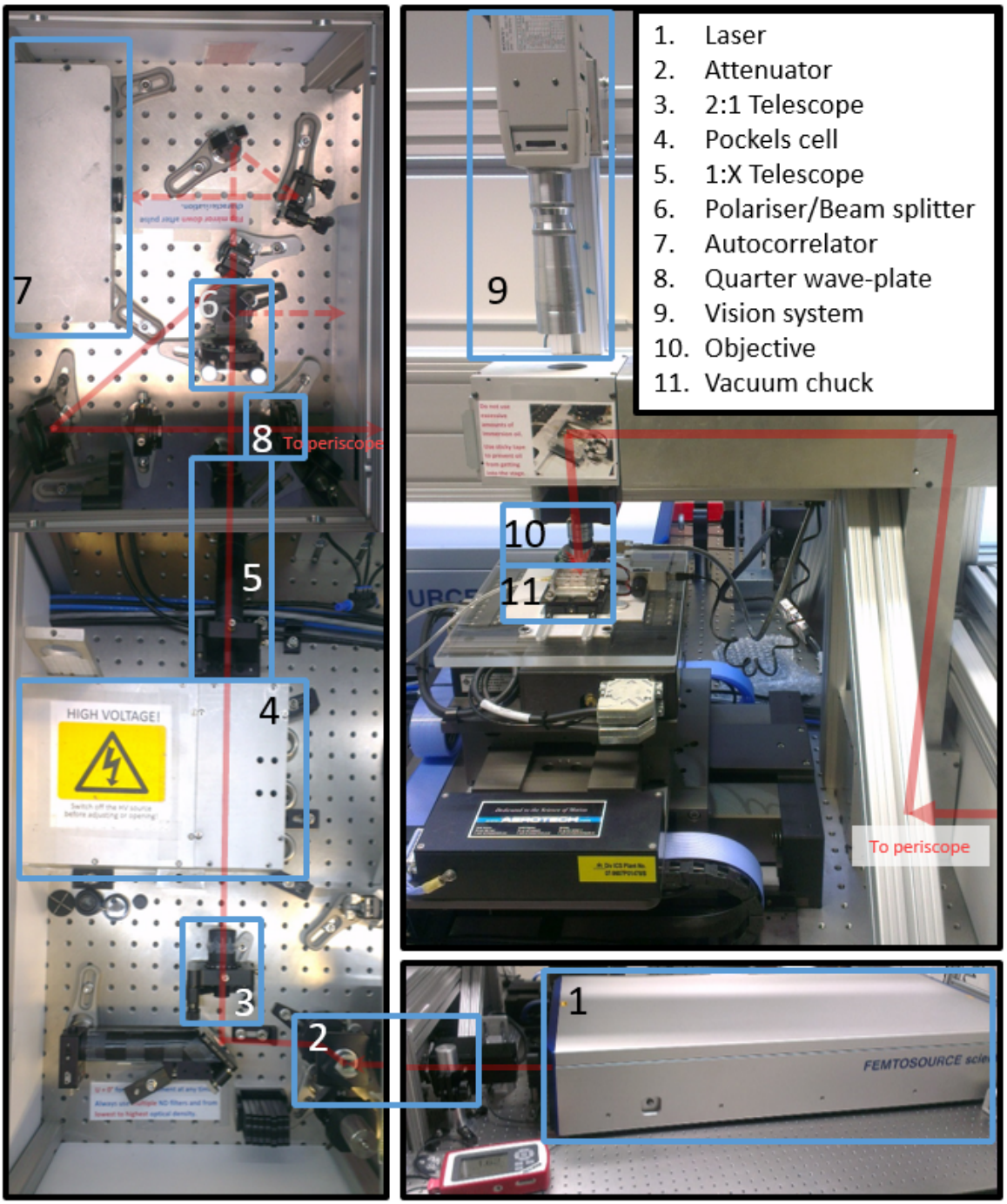

Figure 4.3: Beam path.

the dichroic mirror to monitor the writing process. The beam then finally passes through a 6-axis mount that is used to hold the focusing objective. The 6-axis stage enables the objectives optical axis to be aligned co-linear with the laser beam.

4.1.3 Pockels Cell

Pockels cells use the electro-optic effect to induce birefringence in an optical medium. When a high voltage is applied across a Pockels cell, the polarisation state of the beam is changed. By applying a voltage at the correct time across the Pockels cell, the polarisation of the pulses can be changed. This in conjunction with the polarising beam splitting cube, allows the user to actively pick single pulses from the lasers 5.1 MHz pulse train and thereby change the repetition rate of the laser. The selectable repetition rate facilitates switching between the athermal and cumulative heating regime. The pulse picker uses a 3 mm clear aperture rubidium titanyl phosphate ($RbTiOPO_4$−RTP) Pockels cell (Leysop Ltd., UK). The Pockels cell's timing electronics are connected to the position feedback output of the stages, enabling the lasers output to be blocked nanometre precision. This allows for the inscription of Bragg-gratings for instance.

4.1.4 Stages

The motion control setup consists of 3 Aerotech linear translation stages. The stages allow for motion in XYZ for the fabrication of 3 dimensional optical devices. The base stage is an Aerotech ABL2000 air bearing direct drive linear stage that controls the X-axis. Placed on top is a more compact Aerotech ABL1000 air bearing direct drive linear stage that controls the Y-axis. Finally an Aerotech WaferMax Z Mechanical Bearing direct drive lift stage is used for the Z-axis.

The stages have travel ranges of 100 mm, 100 mm and 5 mm, respectively. This limits the maximum device size. The stages have maximum velocities of 3000 mm/min for the X, Y-axes and 240 mm/min in Z. The position resolution is 2 nm in the X,Y and 0.8 nm in the Z. The accuracy is ± 0.5 μm, ± 0.2 μm, ± 1.5 μm for X,Y,Z and the repeatability is ± 0.2 μm, ± 50 nm, ± 0.3 μm again for X,Y,Z. The stages are controlled by an Aerotech U500 Ultra PCI motion controller. This controller also controls the Aerotech ADR75 mechanical bearing rotary stage (U-axis), enabling computer controlled power adjustment. Computer programs written in G-code are interpreted by the U500 motion controller, allowing control of the position and speed of the stages. By controlling the stages the position and power of the lasers focus within the sample is adjusted. Mounted on top of the three translation stages is a mirror mount with a vacuum chuck attached. The mirror mount is used to align the sample surface parallel to the stages, while the vacuum chuck secures the sample, ensuring it does not move during fast acceleration and deceleration. To align the samples surface parallel the stages, the laser is focused onto the surface of the sample. The mirror mount can then be adjusted so that the lasers focal point is on the samples surface across the sample.

4.2 Postprocessing

4.2.1 Thermal treatment

Laser induced refractive index modifications can be altered by thermal annealing [49]. If the waveguides are annealed correctly, the bend losses and coupling efficiency can be improved [105]. To thermally anneal a laser written structure, the glass sample is heated above the annealing point of the glass. Once above the annealing temperature the sample is slowly cooled to below the strain temperature of the material. Slowly reducing the temperature of the material avoids inducing stress fields. Figure 4.4 shows the refractive index distribution of a waveguide before and after thermal annealing. Before thermal annealing there are 3 clear regions of refractive index change; a positive central region, a ring of negative change, and an outer positive index change. After thermal annealing the outer region of positive index change has been removed.

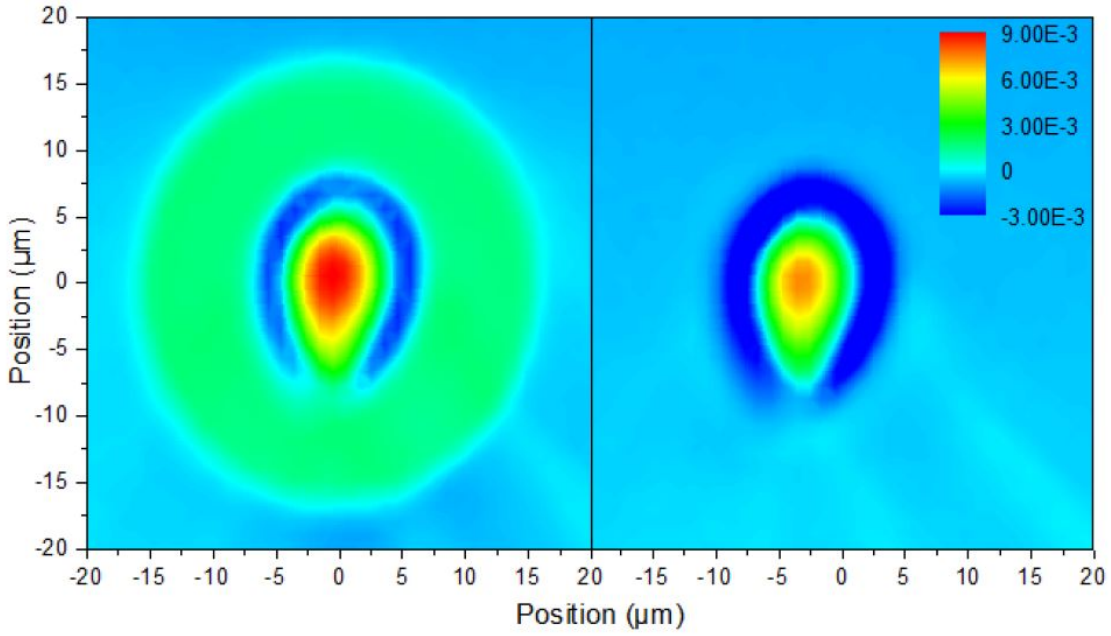

Figure 4.4: A refractive index profile of a laser written waveguide before (left) and after (right) thermal annealing [105].

The laser induced refractive index change is attributed to ion migration [106, 107], while the outer region appears to be caused by a visco-elastic deformation [108]. Elemental migration needs temperatures higher than the thermal annealing point of the material, therefore thermal annealing effectively removes only the outer refractive index region.

The thermal properties of Eagle2000 can be seen in Table 4.1. Using a commercial heat treatment furnace and an integrated Shimaden FP21 temperature profile controller (Shimaden Co. Ltd), samples were heat treated following a specified heat profile. Initially the Eagle2000 sample was slowly heated to 750°C, which is just beyond the thermal annealing

Material	Eagle2000
Strain point	666° C
Annealing point	722° C
Softening point	985° C

Table 4.1: Thermal characteristics of Corning Eagle2000 [58].

point and below the softening point. The material temperature is then slowly reduced over multiple hours until the sample temperature is below the strain point.

4.2.2 Grinding and polishing

Once the laser written structures have been fabricated, the waveguide ends need to be exposed to characterise the device. When a laser written waveguide approaches the edge of a sample, the waveguide begins to taper. Tapering occurs as the focused beam no longer completely passes through the samples surface. This reduces the intensity of light at the focal point and hence decreases the waveguide size. Tapering typically begins ≈ 200 μm from the edge of the sample. As tapering effects the size of the waveguide, all structures need to be written 200 μm away from the edge, or the tapered region must be ground away. Either way the samples edges need to be ground back to reveal the structure.

To grind and polish samples quickly, a simple hand polishing technique was used. This enables prototypes to be quickly evaluated. Initially ≈ 120 μm was removed using a diamond bench grinder. Next Thorlabs diamond fibre polishing/lapping sheets of $30, 5, 3, 1$ μm and a final silicon dioxide lapping sheet was used to carefully polish the endfaces. An alternative method that was also used was to grind back the samples 200 μm using the diamond bench grinder to remove any waveguide tapering. Then when optically characterising these chips an index matching oil was used removing the need for polishing, with only a small reduction in measurement accuracy.

4.3 Device Characterisation

4.3.1 Visual inspection

After fabrication, an Olympus (IX81) Motorized Inverted Microscope (Figure 4.5b) was used to inspect the samples. As the structures are transparent, typical bright field illumination techniques are ineffective in visulising the structures. To enhance the contrast between sample and structure, the microscope is equipped with Transmission Differential Interference Contrast (T-DIC) capabilities. A T-DIC microscope converts optical path length gradients (e.g. small refractive index changes) into intensity differences [110].

In a T-DIC microscope, light emitted from the light source passes through a polariser. The light is then passed through a Nomarski or Wollaston prism with its optical axis at 45°

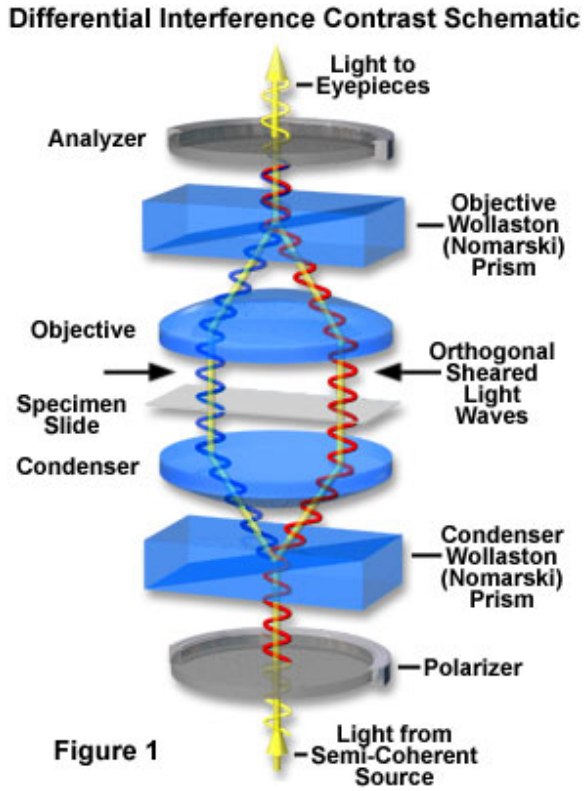

(a)

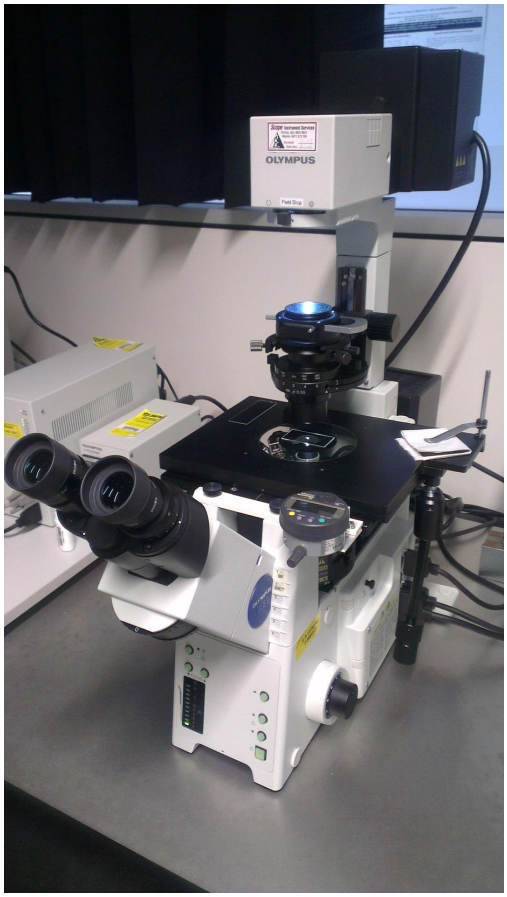

(b)

Figure 4.5: (a) Schematic showing Differential Interference Contrast optical processing [109], (b) Photo of the Olympus IX81 DIC microscope.

to the polariser. This splits the light into two linearly-polarized components (Figure 4.5a), known as the ordinary and extraordinary rays. The two orthogonally polarised wavefronts are then focused through the sample by a condenser. Since the two wavefronts are spatially separated by the Wollaston prism. When one passes through a refractive index modification it experiences an optical path difference. This path difference creates a phase shift between the two wavefronts. The microscope objective then collects the two wavefronts which are re-combined using an inverted second Nomarski or Wollaston prism. Light then passes through a second linear polariser (analyser) orientated orthogonally to the first polariser. Light that has passed through a homogeneous medium will be linearly polarised and blocked by the analyser, whereas light that has passed through an area of changing refractive index will recombine as elliptically polarised and pass through the analyser. Therefore regions with a refractive index change appear darker or brighter depending on bias retardation on the second prism. An Olympus DP72 CCD camera is attached to the side port of the microscope enabling imaging.

4.3.2 Optical Characterisation

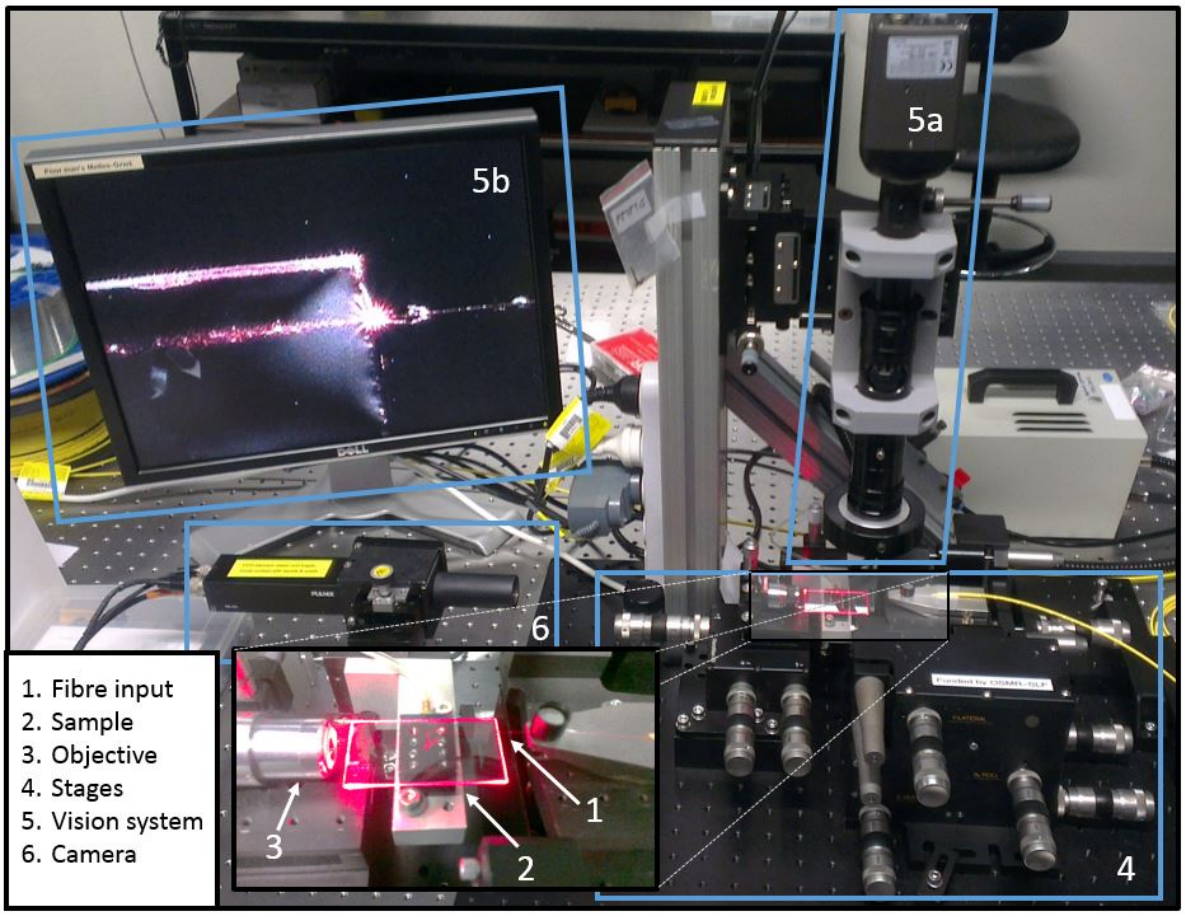

Figure 4.6: Optical characterisation set-up.

To characterise the propagation of light through different laser written structures, it is important to have a facility with the ability to precisely position optical fibres, devices and objectives to a sub-micron precision. The facility seen in Figure 4.6 consists of a 6-axis flexure stage (Thorlabs NanoMax 600 series) seen on the bottom right. This stage allows for accurate fibre positioning to inject light into devices. A 3-axis stage is positioned in the centre, with a vacuum chuck to secure the sample. On the left a 3-axis flexure stage (Thorlabs NanoMax 300 series) has an additional pitch/yaw platform placed on top. This effectively creates a 5-axis stage that can be used to position an output fibre or objective to characterise the output of the device. Above the sample is a vision system which allows for fibre positioning. The vision system can also be used to view scattering and fluorescence from samples. When viewing fluorescence at 633 nm, a Thorlabs notch filter is placed inside the objective tube to suppress the scattered HeNe light and the vision system camera is replaced by a Thorlabs DCC1645C USB camera (Table 4.2) to capture images of the fluorescence or scattering.

4.3.3 Output Measurement

The slab and waveguide array mode-field profiles were recorded by launching 633 nm light (Becton Dickinson Lab Helium-Neon HeNe laser) via a single-mode fibre (Thorlabs SM600) into the device. The samples were butted against a microscope slide with index matching immersion oil. Using index matching oil removes the need to polish the samples end-faces and therefore enables characterisation immediately after fabrication and grinding. Immersion oil was also used on the input fibre to reduce coupling losses. Finally a microscope objective imaged the output onto a camera (Pulnix TM-745E, see Table 4.2). The Spiricon LBA-PC software was used to capture the output mode-profiles for post processing. Different objectives, as described in Table 4.3, were used in order to maximise the camera illumination depending on the mode size of the structure . The magnification of each objective was calibrated for each measurement using either one of the following two methods.

- Measuring the known separation between two waveguides within the sample. Light is injected into one waveguide and its central pixel position recorded. The input fibre is then moved to inject light into the second waveguide and its central pixel position recorded. The known separation of these two waveguides is used as pixel scale calibration.
- Similarly, slabs with multiple output guides have known output waveguide separations. When imaging these output guides the separation of the outputs can be used as a pixel scale calibration.

Model	**Sensor**	**Dynamic Range**	**Resolution**	**Spectral Response**
Pulnix TM-745E	2/3" CCD	67 dB	768 x 493, 11 x 13 μm	0.4–1.1 μm
Thorlabs DCC1645C	1/3" CMOS	NA	1280 x 1024, 3.6 x 3.6 μm	0.4–0.65 μm

Table 4.2: Camera Specifications.

4.3.4 Transmission measurements

To measure the losses of the laser written devices the Spiricon LBA-PC softwares aperture measuring tool was utilised. The software allows the user to draw an aperture over an area of interest. The program then integrates the intensity of each pixel to calculate the total power. This power value can be calibrated by measuring the output power from the input fibre with a power meter. This input fibre is then also measured with the Pulnix camera and the integrated aperture is calibrated to this power value. Measurement uncertainties arise from variations in the laser output power, the size of the aperture and stray background

Magnification	Supplier	Type	Numerical Aperture(NA)
4x	Olympus	NA	0.1
32x	Leitz	NA	0.6
50x	Olympus	M S Plan	0.8
100x	Olympus	M S Plan	0.95

Table 4.3: Microscope objectives.

light. However, this technique allows structures with multiple outputs or broad outputs to be characterised quickly and easily within the accuracy required.

4.3.5 Reverse Helmholtz Equation

The Helmholtz equation relates the refractive index profile of an optical waveguide and the field distribution of that optical waveguide. If the optical waveguide is single mode, the Helmholtz equation can be rearranged to determine the refractive index of the optical waveguide from the near-field profile [111].

$$n^2(x,y) = (n_b + \Delta n(x,y))^2 = n_{eff}^2 - \frac{\lambda^2}{4\pi^2}\frac{\nabla^2 E(x,y)}{E(x,y)} \tag{4.1}$$

By numerically solving Equation (4.1) the refractive index profile can be recovered and has been shown to match refractive index profile calculated through other methods [112]. Due to the second order differential, the refractive index profile obtained is highly sensitive to noise in the near-field profile. The technique has also been found to have reduced accuracy with smaller mode profiles. Using mode profile images the structure and index of single mode guides were determined using a reverse Helmholtz Matlab program courtesy of Friedrich Schiller Uni, Jena, Germany.

4.4 Arrayed Waveguide Grating Design and Modelling

AWGs were designed using a commercial Computer Aided Design (CAD) package by RSoft. The RSoft program contains an AWG design utility that can automatically generate full AWG layouts using only a few user defined parameters. As these parameters are integrated, the AWG design is automatically recalculated after each parameter change.

The automatic layout recalculation enables the user to visually see how small adjustments affect the layout, and to ensure the design is physically sensible. Once a design is established, RSofts simulation engine BeamPROP is used to simulate the design performance.

4.5 AWG layout generation

Parameter	Typical value
Material refractive index	1.505
Refractive index contrast	1.5×10^{-3}
Number of input waveguides	1
Number of output waveguides	0
Number of PSFs at the chips output	9
Number of waveguides in the waveguide array	41
Diffraction order	16
PSF size at output	4.5 nm
Central operating wavelength	632.8 nm
Free Spectral Range(FSR)	40.5 nm

Table 4.4: Generation parameters and their typical values.

The AWG design utility uses an auto generating script known as STARGEN. This script calculates the complex geometry using a few parameters to determine the topology of the device. These parameters and typical values can be seen in Table 4.4. A brief description of selected parameters are given below.

Output waveguide Since the AWGs are being fabricated for spectrographic purposes output waveguides are not required to directly record the spectrum at the output FPZ.

Number of array waveguides The number of waveguides was kept low. The benefits of keeping the number of waveguides in the array low are reduced chance of phase errors in the waveguide array, higher throughput and a smaller slab width. However the disadvantage is a low resolution. Despite this, obtaining a working prototype was considered more important than achieving high resolution.

Number of output PSFs Determines the FSR of the device.

PSF size Is related to the AWGs resolving power R. The number of PSFs and the PSF size determines the size of the device and FSR and R becomes a trade-off.

After the key parameters have been determined other secondary parameters can be adjusted to fine tune the design. The separation between waveguides can be varied. This is normally selected to be large enough to prevent cross talk between the waveguides and

small enough to reduce the size of the FPZ. Another parameter that can be adjusted is the curvature for the first waveguide in the array. Compared to silica-on-silicon devices that have bend radii of 5 mm with low losses, laser written waveguides have a lower refractive index contrast and therefore the bend radii must be increased to values larger than 25 mm and higher in order to reduce losses [113].

Finally the user can define the angle between the two FPZs. The angle is restricted by the curvature of the array and the length increment (ΔL) between waveguides. Typically the angle of designs is restricted to 8–15° for visible laser written AWGs. This makes designs relatively narrow in the x-axis meaning many AWGs can be placed close together on a single chip. This also ensures that direction dependent writing properties do not effect the device performance [114].

The input waveguide taper was omitted as this has been shown to be detrimental to the spectrograph's resolution. The length of the slab/waveguide array transition taper can also be adjusted to maximise throughput. Figure 4.7 shows the typical layout generated by the AWG utility. These parameter give a FSR of 40.5 nm and an R of ≈ 440 with dimensions of 3.7 $\times$ 2.7 cm and a theoretical throughput 25% for the central order.

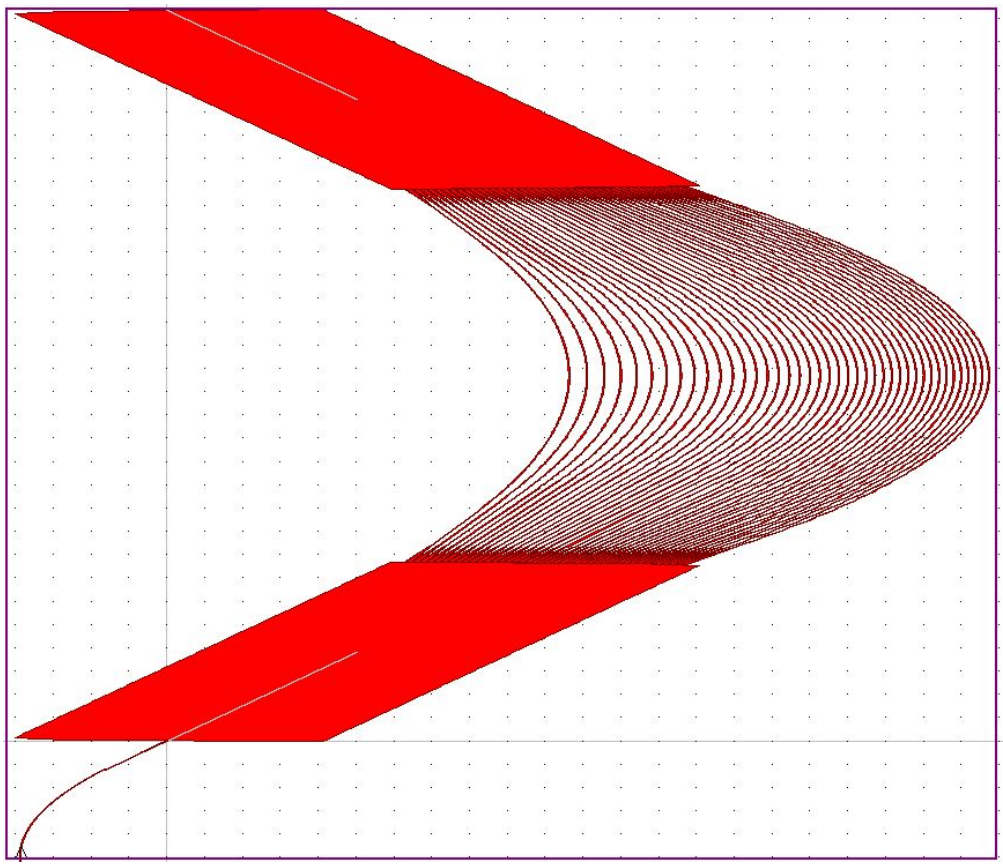

Figure 4.7: An example of a typical full AWG CAD layout. The design parameters are identical to the fabricated AWGs. To view the whole structure, the aspect ratio of the figure is set to 18.1:1.

4.6 AWG simulation

4.6.1 BeamPROP

BeamPROP is a simulation module of the RSoft Photonics suite software. BeamPROPs simulation engine is specifically made for computing the propagation of light waves in arbitrary waveguide geometries [79]. BeamPROP uses the finite difference beam propagation method (BPM) [115–120]. This technique solves the well-known parabolic or paraxial approximation of the Helmholtz equation using finite difference methods.

A fundamental limitation of solving the Helmholtz equation using the parabolic approximation is the inability to simulate backward reflections. To solve this issue RSoft has the capability to use a more accurate approximation to the Helmholtz equation known as the bidirectional BPM algorithm [121]. By using this algorithm forward and backward travelling waves can be simulated meaning structures such as gratings and ring resonators can be modelled. However the cost of simulating back reflections is a large increase in computational time. As AWGs do not contain any reflective components bidirectional BPM was not used. However this restricts the simulation of AWGs to angles less then approximately 15° [91] as the waveguide array requires the simulation of back reflection to guide light. To avoid using the bidirectional BPM algorithm the simulation is spilt into parts, as discussed in section 4.6.2.

To solve physical propagation problems BPM requires two key pieces of information, the refractive index distribution $n(x, y, z)$ and the input wave field $u(x, y, z = 0)$. The algorithm also requires numerical simulation parameters which include a finite computational domain, transverse grid step size (Δx, Δy) and the longitudinal simulation step size (Δz). BPM's computational time is essentially proportional to the number of grid points used in the simulation.

To solve the wave equation, BPM applies two approximations, a scalar field and paraxiality e.g. polarisation effects are neglected and propagation is restricted to a narrow range of angles (a brief mathematical description of these approximations can be found in Appendix A.2). The benefits of these approximations are as follows; by using a slowly varying field the grid size in the z direction can be longer than the wavelength. By removing the second derivative term the boundary value problem is reduced from a second order boundary value problem requiring iteration or eigenvalue analysis, to a first order problem that can be solved by integration. These benefits however can limit modelling. The limitations include fast variations of the refractive index in the z direction and complicated superposition of phase e.g. multi-mode interference devices. Simple AWG designs do not include complex rapid refractive index changes, however complex designs that include rapid tapers such as a segmented taper could be affected.

There was valid concern that using the slow varying field approximation would negatively effect the simulation of the light interference in the second slab that is essential for AWG operation. To check this, a simulation of an AWG was run using a wide-angle BPM[3]. However there was no visible difference between simulations. It is also important to note

[3]Wide-angle BPM allows large angles, high index contrast and complex mode interference to be modelled more accurately. BeamPROP uses the multistep Padé-based wide angle technique [122].

that in simulations involving slab refractive index variations the wide-angle BPM was used with a small grid size.

4.6.2 AWG Simulation

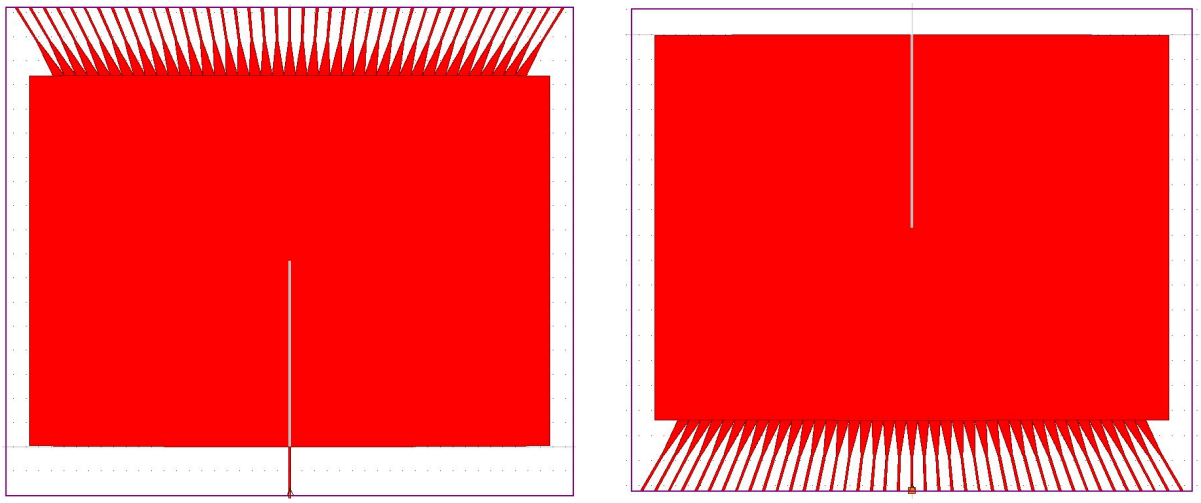

(a) (b)

Figure 4.8: The CAD layout files for the (a) input and (b) output FPZ's. The pale lines seen within the FPZs are virtual markers required by the BeamPROP program to correctly position components from.

Typical AWGs used in telecommunications have large angles in the order of 45°. Due to simulation constrains (Section 4.6.1), AWGs of large angles cannot be simulated as a whole. To avoid this issue a WDM Router Simulation Utility generates two design files for the input and output FPZ, respectively. The input file includes the input waveguide, the first FPZ and the start of the waveguide array (Figure 4.8a). The output file contains the end of the waveguide array and the second FPZ (Figure 4.8b). By separating the AWG into two parts the simulation complexity is reduced. Even though it is possible to simulate the design as a whole for designs with small angles as seen in Figure 4.9, the simulation utility was used due to its simplicity and speed.

For the simulation light is launched into the input waveguide. Light propagation is then simulated through the first FPZ and into the start of the waveguide array as seen in Figure 4.10a. At this point the mode field is recorded and should already be a series of discrete single modes. Next a script called PHASECOR applies a phase shift to each of the discrete single modes that corresponds to the length increment of *Delta L* of the waveguide array. By applying a virtual phase shift computational time is reduced since simulation of the waveguide array is avoided. Unfortunately PHASECOR does not automatically calculate bend losses. However the user has the ability within the PHASECOR script to include bend losses and random phase errors for more accurate device performance analysis. The phase adjusted file from PHASECOR is then saved as a launch field file using a script called FIELDGEN. This mode field can then be launched into the second FPZ and the propagation

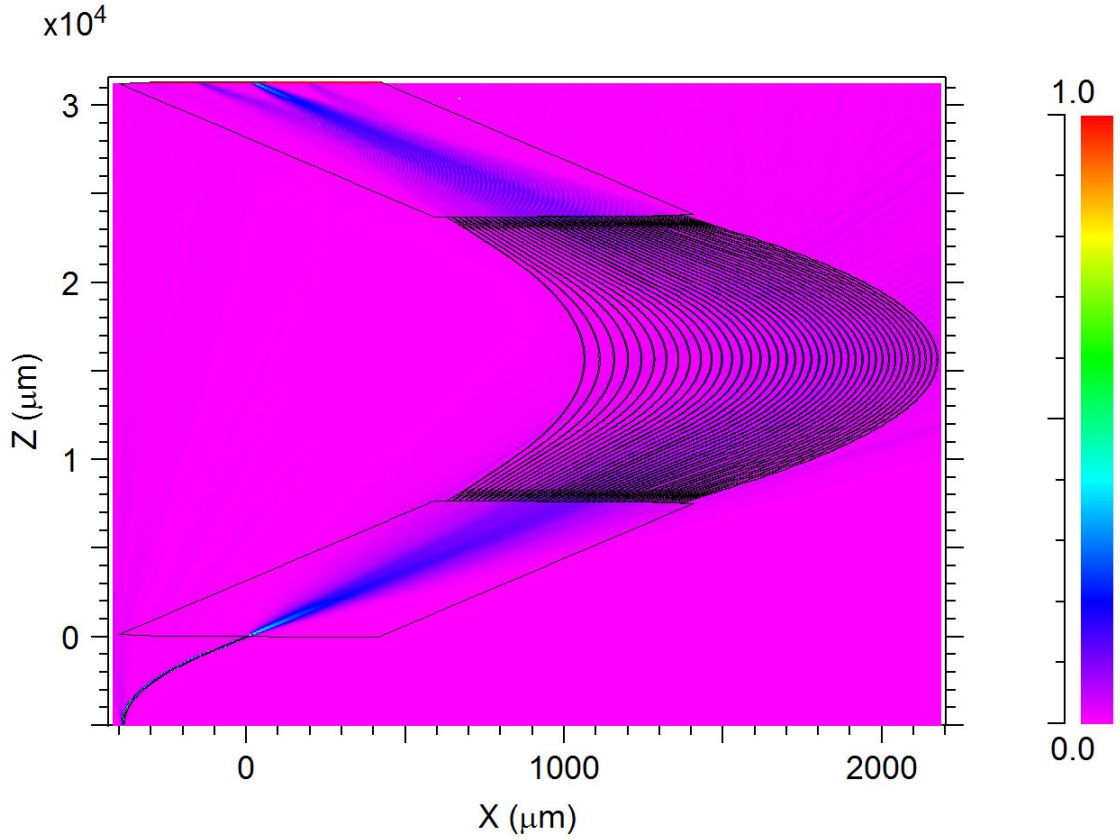

Figure 4.9: Full AWG simulation at 633 nm. The colour bar represents the field amplitude. To simulate the AWG as a whole the wide-angle BPM was used along with a small grid size. This simulation takes approximately 20 mins to run using an Intel core i7-4770 CPU, 3.40 GHz, 16 Gbit RAM.

can be simulated (Figure 4.10b). A cross section of the final simulated position can also be taken, this is consistent with how our AWGs are polished back flat to the end of the FPZ for visual inspection. When the output field of the full simulation is compared to the output field of the utility simulation at 633 nm, the outputs are shown to have peaks in the exact same location.

A script call SCRIPGEN can be used to perform a scan over a range of wavelengths. The final simulation output is displayed as a transmission loss in (dB) for each channel. When simulating the AWGs over a range of wavelengths the script simulates the input FPZ at a single wavelength. This approximation is sensible as the FPZ is only weakly wavelength dependent. For devices with large FSR it is possible to simulate both FPZs over all wavelengths to obtain more accurate results.

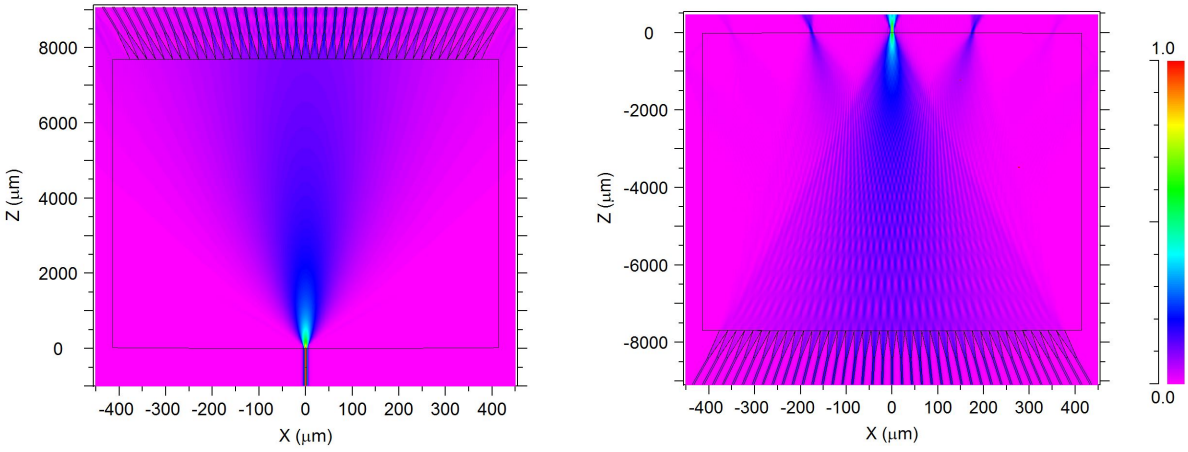

(a) (b)

Figure 4.10: Beam propagation simulation of the (a) Input FPZ and (b) Output FPZ. In the output FPZ, the main central interference order is clearly visible. Either side of this central interference order additional orders can be seen. This essential shows the physical size of the FSR of the device. In the simulation light is propagated from the bottom of the page to the top.

5 Free propagation zone studies

The FPZ is a smooth medium in which light can diffract and interfere. If the FPZ has a non uniform refractive index, these processes can break down, destroying the functionality of the AWG. FPZs fabricated using photolithography have a typical refractive index uniformity ranging from 1×10^{-5} to 3×10^{-4} [69]. To fabricate functional laser written AWGs, methods to inscribe large areas of uniform refractive index must be developed. As previously discussed, relatively little work on laser fabricated slab waveguides has been reported so far. Therefore this chapter explores the fabrication of uniform slab waveguides using the femtosecond direct write technique.

5.1 Slab waveguides in fused silica

Suprasil was initially chosen for slab fabrication for two main reasons: Firstly, slab fabrication has previously been demonstrated in fused silica [63]. Secondly, fluorescence visualisation techniques can be utilised for laser written structures in Suprasil. Fluorescence enables light propagation within slab structures to be analysed and compared to theoretical simulations. Also interference can be visualised within the second FPZ in order to identify fabrication errors.

Using the laser writing system described previously 6 μm wide waveguides were fabricated using the multi-scan technique. Waveguides were inscribed using a 50 $\times$ microscope objective, pulse energies of $20 - 100$ nJ, writing speeds of $12 - 1200$ mm/min, repetition rates of 250 kHz $- 5.1$ MHz and a multi-scan spacing of 0.4 μm. Additionally 20 and 30 μm wide slabs were inscribed using a 500 kHz repetition rate, matching the repetition rate used by Ghosh *et al.* [63], in order to evaluate the multi-mode interference. Figure 5.1a shows a top down image of 30 μm wide slabs inscribed at 60 and 40 nJ, respectively. The slabs were found to have a granular micro-structure. This granular micro-structure appeared to be more distinct for with higher pulse energies. However the actual size of the granular

features was determined to be constant. The micro-structures also appeared under DIC observation to be brighter with increasing repetition rates. Figure 5.1b shows the slab visually inspected end on. Slab waveguides fabricated with a repetition rate of 500 kHz and pulse energy of 60 nJ exhibited have smooth core regions, while those fabricated using 40 nJ pulse energies appear to have some periodic structure. This periodic structure was attributed to interference pattern caused by the slab waveguides small width. End on observations of the 6 μm wide guides also showed that repetition rates of 500, 728 and 1019 kHz have similar guiding properties, while those produced at 5.1 MHz showed large areas of damage.

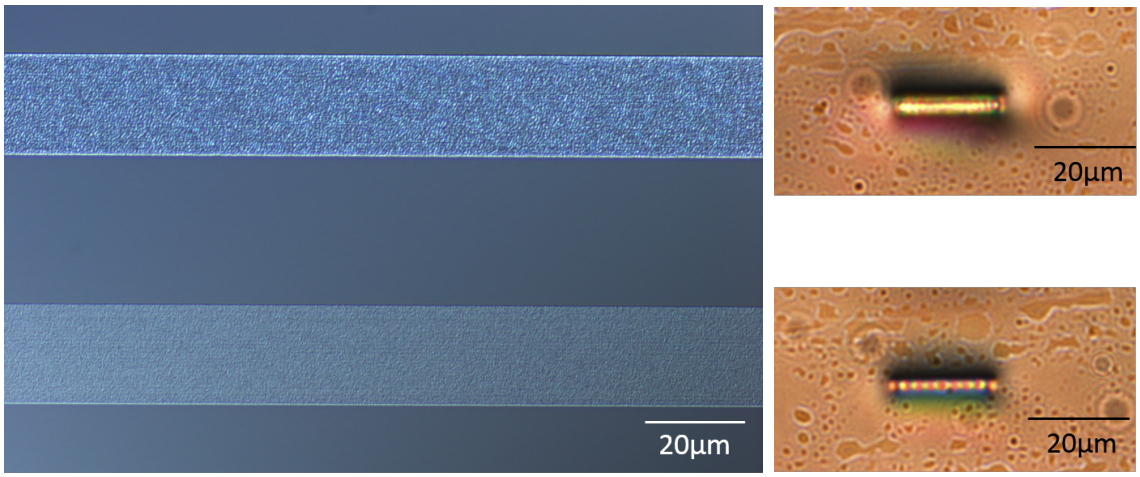

(a) (b)

Figure 5.1: (a) Top down view of 30 μm wide slabs written in Suprasil at 500 kHz repetition rate using 60 nJ (top) and 40 nJ (bottom) pulse energy respectively. A granular micro-structure is clearly visible. (b) End on images of 20 μm wide slabs 60 nJ (top) 40 nJ (bottom).

Light was injected into the 6 μm waveguides using the optical characterisation setup. Figure 5.2a shows the observed scattering causing high losses, while Figure 5.2b shows the observed fluorescence excited by light propagation down the waveguide. The fluorescence supports smooth propagation within waveguides inscribed with a 500 kHz repetition rate and 60 nJ pulse energy. All laser written structures, independent of the writing parameters, had observable fluorescence. However, at high pulse energies the propagation losses within the waveguides increased, resulting in a rapid decay in fluorescence intensity.

The 6 μm wide waveguides had the best guidance at a repetition rate of 500 kHz, 60 nJ pulse energy and a feedrate of 120 mm/min and a repetition rate of 728 kHz using 60 nJ pulses and a feedrate of 240 mm/min. Even with optimised writing parameters, waveguides written in Suprasil exhibited high losses. Due to these high losses, no further work was undertaken to fabricate waveguides in Suprasil.

Corning 7780 HPFS was selected as a possible alternative to Suprasil. A parameter scan was was undertaken using a 20 $\times$, 0.46 NA focusing objective, pulse energies of $200-400$ nJ, writing speeds of $75-3000$ mm/min and repetition rates of 728 kHz and 5.1 MHz. These parameters were centred around the fabrication parameters used to write in Suprasil by

Dreisow *et al.* [56]. This time the micro-structures previously observed were no longer present, however the high losses remained. As these losses where too high to create a functional device, it was decided an alternative substrate material was required. The laser system used has 50 fs pulses centred around 800 nm this is vastly different to other systems that have previously shown success writing low loss waveguides in fused silica that have pulses of 400 fs and are centred around 1030 nm wavelength.

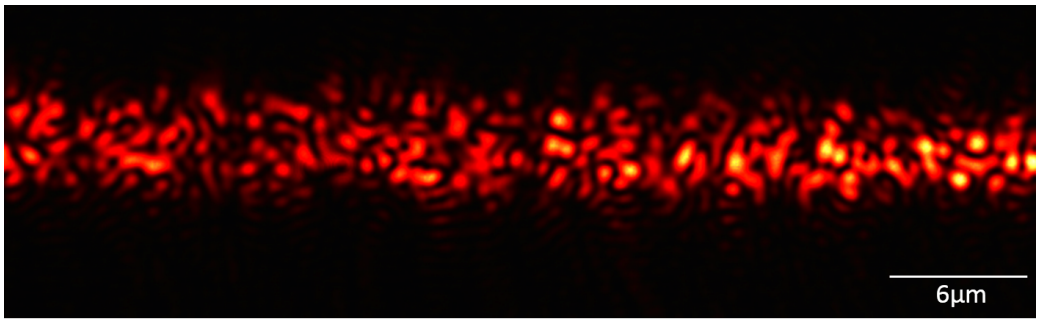

(a) Scattering

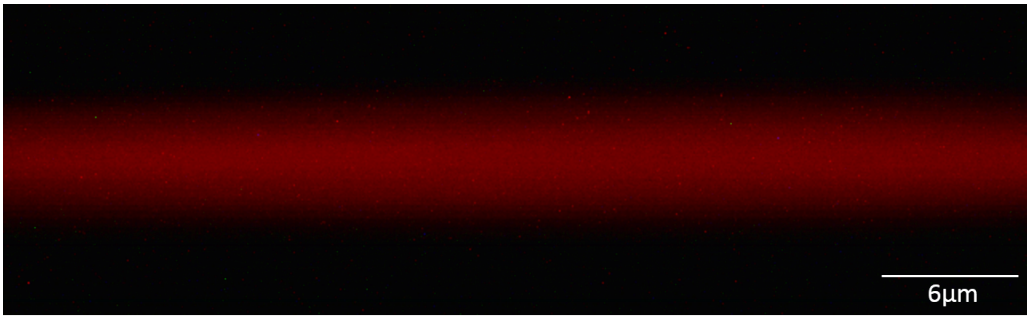

(b) Fluorescence

Figure 5.2: Micrographs viewed from above of the observed scattering (a) and fluorescence (b) of 6 μm wide waveguides inscribed with 500 kHz, 60 nJ.

5.2 Slab waveguides in Eagle 2000

5.2.1 Strong cumulative heating regime

Eagle2000 was selected because high quality waveguides can be inscribed at 5.1 MHz repetition rate. The ability to write waveguides at a high repetition rate allows fast stage translation, enabling large devices such as an AWG to be inscribed in only a few hours. For lower repetition rates large multi-scan slabs could take a whole day to write, increasing the susceptibility to laser instabilities. A disadvantage of Eagle2000 is its lack of fluorescence. Without fluorescence, light propagation evaluation of the device is limited to near-field imaging. Another disadvantage is that the typical modifications inscribed in Eagle2000 at 5.1 MHz have regions of both positive and negative index change [105], caused by ion migration [106, 107]. The formation of a negative region around the laser written waveguide

is problematic especially for slab inscription as multiple waveguides are required to be overlapped. These negative regions could potentially compromise the formation of a smooth refractive index change across the slab waveguide.

Using an Olympus 100 ×, 1.4 NA objective at 54 nJ pulse energy, 5.1 MHz repetition rate and a feedrate of 1200 mm/min, symmetrical waveguides were fabricated. Slab waveguides were written by overlapping waveguides in either a symmetric or asymmetric sequence with a line-spacing of $3 - 7$ μm as shown in Figure 5.3. Symmetrically written slabs have the first waveguide written in the centre of the slab and each successive waveguide is written on either side, building up the slab structure from the inside out. Asymmetrically written slabs are built by continuously overlapping waveguide in a singular direction. When viewed end on it can be seen that each waveguide overlaps the previously written waveguide. This is visible because the depressed cladding appears as a dark ring, as light from the microscope is only guided down the positive refractive index cores. The waveguides were then thermally annealed as discussed in Section 4.2.1. Annealing removed the outer region, while the depressed cladding rings remains clearly visible. Thermal annealing can not remove the depressed cladding as the annealing temperature is not high enough for ion migration.

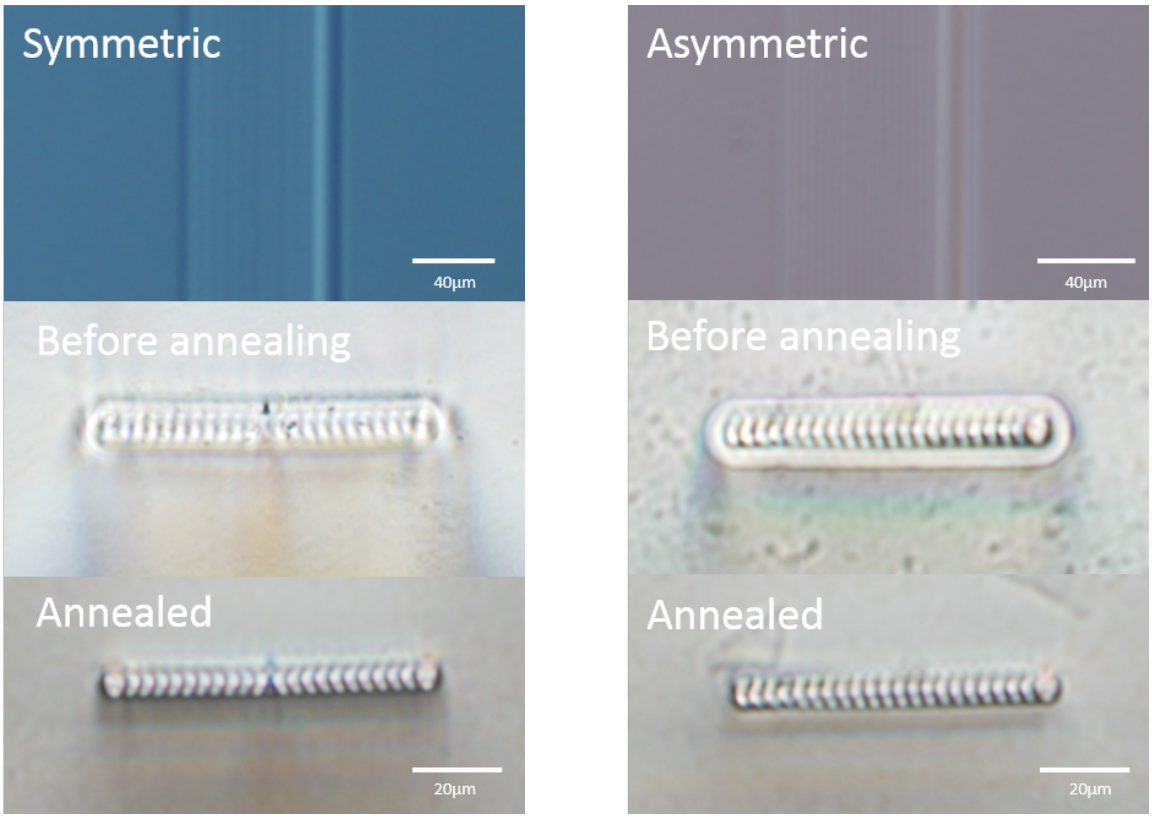

(a) (b)

Figure 5.3: (a) Symmetrically written waveguides with 3 μm spacing (written inside out). (a) Asymmetrically written waveguides with a 3 μm spacing written (left to right). (top) is a DIC top view, (middle) slab waveguides without thermal annealing, (bottom) thermally annealed slab waveguides.

The light injected into these slab waveguides was found to be strongly guided down the individual high index cores. As these parameters did not yield a successful slab waveguide it became clear that a different approach was necessary. The key issue faced in the cumulative heating regime is the depressed cladding. One option was to decrease the waveguide spacing further. The second option was to move to a different writing regime. At the time it was decided to move to a new writing regime as these waveguides were occasionally showing vertical multi-mode guidance at 632.8 nm, an unwanted feature in AWGs.

5.2.2 Weak cumulative heating regime

It was previously observed whilst undertaking power-scans that just above the cumulative heating threshold the depressed cladding and the vertical waveguide size was reduced. Since the depressed cladding is minimised the overwriting effect is diminished, ideally allowing the fabrication of a smooth refractive index slab waveguides without the depressed cladding observed in Section 5.2.1. Since the vertical waveguide size is decreased, light guided within the slab will be single mode in the vertical direction. A preliminary study was undertaken to find conditions that efficiently guide a single mode at 632.8 nm.

5.2.3 Inscription of single-mode waveguides

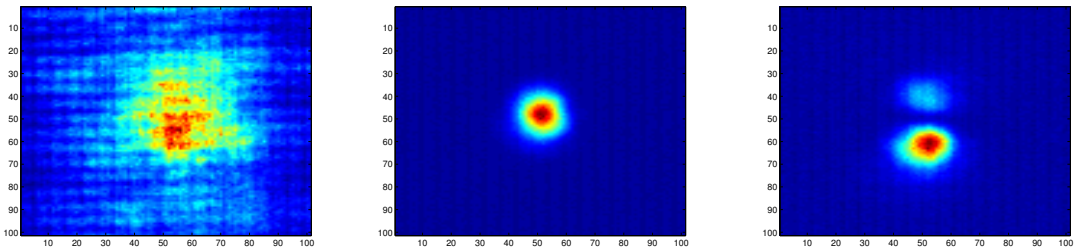

(a) Below threshold (b) Just above threshold (c) Well above threshold

Figure 5.4: (a)Shows that below the cumulative heating threshold the laser written modification weakly guides light, (b) 2 nJ above threshold a single guided mode is observed. (c) 5 nJ above the cumulative heating threshold multi-mode propagation can be observed. All images are of the same scale, as the modification in (a) is below the cumulative heating threshold the refractive index change is low, therefore the guided mode is weakly confined.

Circular waveguides are desirable for slab fabrication as it allows input and output waveguides to be incorporated easily from the slab region by extending one structure from the multi-scan region in order to form a single waveguide. Waveguides with high throughput and circular mode fields were fabricated using an Olympus 40 $\times$, 0.65 NA focusing objective, a translation speed of 2000 mm/min and $1 - 4$ nJ pulse energy above the cumulative heating threshold which is at a pulse energy of 53 nJ (Figure 5.4b). When the pulse energy is below the cumulative heating threshold the refractive index change is minimal and only a weakly guided mode is observed (Figure 5.4a). Alternatively if the pulse energy exceeds

the heat accumulation threshold by 5 nJ or more, multi-mode waveguides are created (Figure 5.4c). The threshold for cumulative heating is observed as a sudden change in the size of the waveguide under DIC imaging (Figure 5.5a). This effect can also be seen end on in Figure 5.5b.

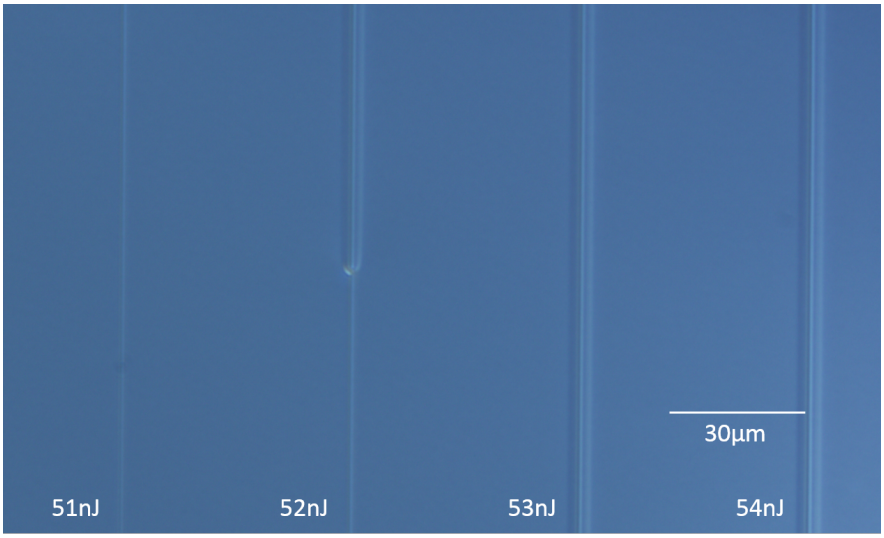

(a)

(b)

Figure 5.5: (a) Power scan showing the laser threshold as a sudden increase in waveguide size. (b) Corresponding end on image showing how the onset of heat cumulation forms a larger circular waveguide core that guides light.

A challenge writing so close to the cumulative heating threshold are surface impurities, dust and laser fluctuations which can cause the intensity at the focus to decrease, resulting in an abrupt interruption to the cumulative heating writing process. To reduce the possibility of this happening, the writing power is typically set $2-3$ nJ above threshold. Due to minute changes in the laser cavity the pulse and repetition rate of the laser can change slightly. These changes can cause the pulse energy required to write waveguides in Eagle2000 to shift on a day to day basis by $4-6$ nJ. To find the threshold a parameter scan is preformed each time before writing a device. At the cumulative heating threshold the appearance of a bright plasma can be observed. This bright plasma is clearly visible through the in-line vision system allowing the threshold to be found.

Using the reverse Helmholtz technique, the refractive index profile of waveguides written at pulse energies 2 nJ above the cumulative heating regime were obtained (see Figure 5.6a). The profile shows that a weakly depressed cladding surrounds a positive index core. The

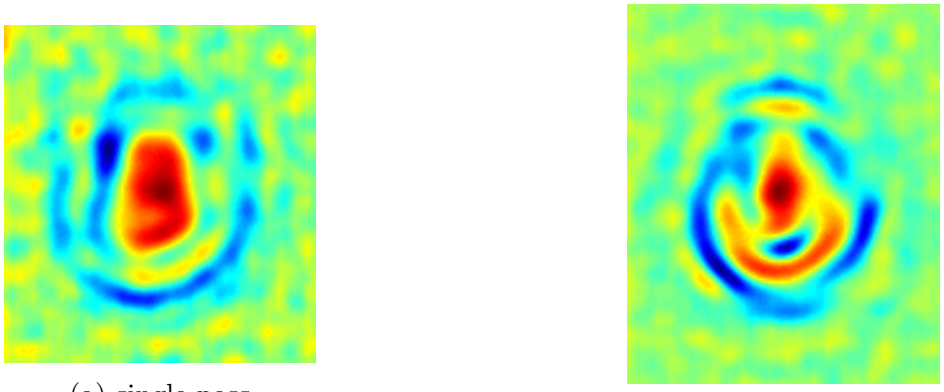

(a) single pass

(b) multipass

Figure 5.6: (a) Calculated refractive index profile of a waveguide inscription using a single laser pass, with a peak index change of $\Delta n = 1.5 \times 10^{-3}$. (b) Calculated refractive index profile of a waveguide inscribed with two laser passes. The core region is seen to have an increased index change of $\Delta n = 2 \times 10^{-3}$ and has an increased depressed cladding. The refractive index profiles were calculated using the reverse Helmholtz equation.

maximum refractive index change ranged from 1.2×10^{-3} to 1.5×10^{-3}. As this value is lower than the typical refractive index contrast in photolithograpically fabricated AWGs, laser written AWGs require a larger chip footprint as the bend radius needs to be increased to reduce bend losses.

One method that has previously been used to increase the refractive index contrast is multipassing the waveguide. Multipassing is where a waveguide is written directly over a previous waveguide thus increasing the refractive index of the waveguide. Figure 5.6b shows the refractive index profile of a double pass waveguide. Waveguides fabricated using the multipass technique were found to increase the maximum refractive index contrast to 1.5×10^{-3} to 2×10^{-3}. This increase in refractive index contrast could reduce the footprint of a laser written AWG. However, double passing was found to increase the depressed cladding which negatively affect the fabrication of smooth slabs. Multiple passes also increases the chance of stage depth errors and increases the writing time of large structures. Therefore multipass waveguides were not pursued for slab inscription.

5.2.4 Inscription of slab waveguides

Using an Olympus 40 ×, 0.65 NA focusing objective, a translation speed of 2000 mm/min and a pulse energy 2 nJ above the cumulative heating threshold, 500 μm wide and 6mm long slabs were fabricated via the multi-scan technique[1] using spacings of $0.3 - 0.8$ μm. Using the optical characterisation stages, 633 nm light was injected into the centre of these slabs using a single-mode fibre and the near-field output was recorded (see Figure 5.7). If the light is freely able to diffract then the near-field output is expected to be a broad Gaussian. A

[1]The multi-scan technique writes multiple waveguides with a small offset, this technique is typically used with highly elliptical waveguides to form a square waveguide for more efficient guiding. However by continually writing a large number of waveguides a slab can be fabricated.

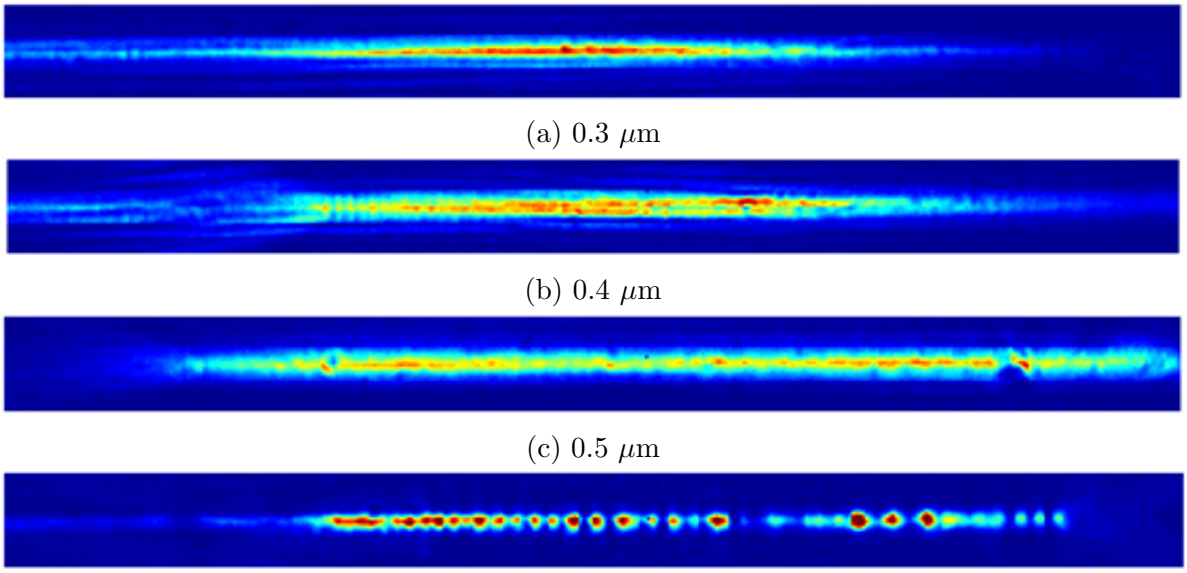

(a) 0.3 μm

(b) 0.4 μm

(c) 0.5 μm

(d) 0.7 μm

Figure 5.7: Near field images of slabs inscribed with varying multi-scan spacing.

Gaussian profile was fitted to the cross sections of the near field outputs.

The output mode-field for multi-scan spacings of 0.3 and 0.4 μm were shown to exhibit a relatively smooth Gaussian output with R^2 values of 0.9644 and 0.8806 respectively (Figures 5.8a and 5.8b). At a multi-scan spacing of 0.5 μm, the measured near-field profile no longer fits a Gaussian profile, (see Figure 5.8c). At this spacing light no longer spreads out in a Gaussian distribution and some points appear to have limited light guidance. Figure 5.7d shows the near-field output profile of a multi-scan spacing of 0.7 μm, this output no longer resembles a wide Gaussian mode, with individual single mode outputs visible across the slab structure. This means that light at this multi-scan spacing no longer spreads smoothly within the slab, and is being individually guided. A multi-scan spacing of approximately $0.5 - 0.6$ μm is the cut-off for smooth slab construction.

The 0.4 μm multi-scan spacing has a Gaussian fit of a reduced quality when compared to the 0.3 μm multi-scan spacing profile. However, the 0.4 μm multi-scan cross section suggests that an artefact on the left hand side has reduced the quality of the fit. During the fabrication of these large slabs it had become clear that the fabrication of a complete AWG would take at minimum over 2 hours with at multi-scan spacing of 0.4 μm and even longer for a 0.3 μm spacing. During the process of writing these large slabs it was found that the laser could drift over a few hours causing the laser writing to fall the cumulative threshold, rendering the slab useless. Since the 0.3 μm and 0.4 μm slabs had similar qualities a multi-scan spacing of 0.4 μm was chosen for future slab fabrication,due to the faster manufacturing speed. Further testing using the 0.4 μm spacing showed Gaussian fits with R^2 values regularly above 0.95 but for a shorter propagation length.

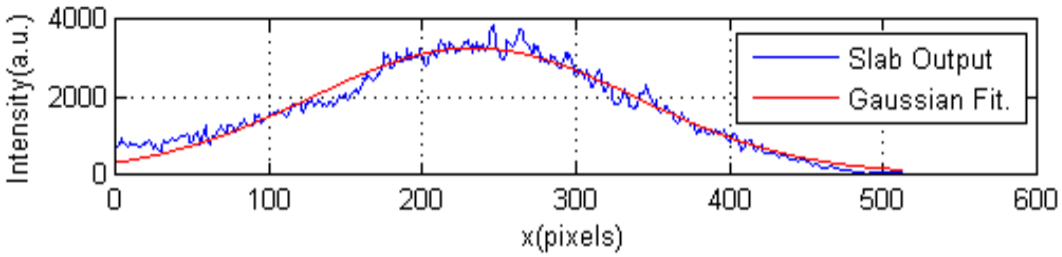

(a) 0.3 μm, $R^2 = 0.9644$

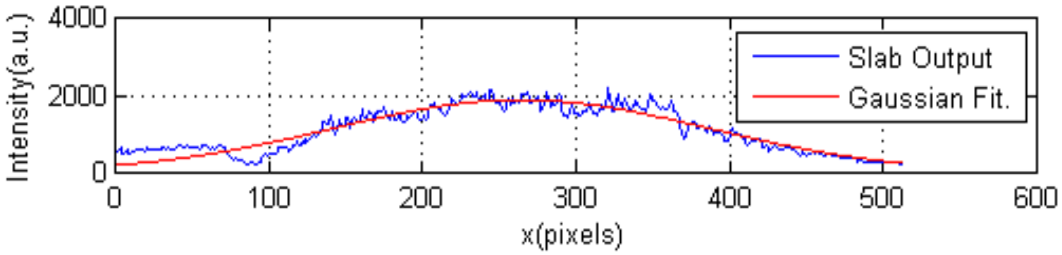

(b) 0.4 μm, $R^2 = 0.8806$

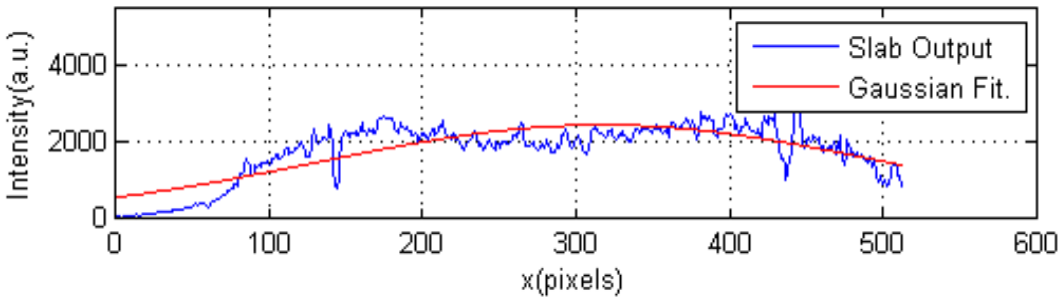

(c) 0.5 μm, $R^2 = 0.6872$

Figure 5.8: Gaussian fit to the cross section of the near field output of slabs fabricated with varying multi-scan spacings.

5.2.5 Slab characterisation

To evaluate the refractive index uniformity of the slab waveguides, light was injected close to the side walls of the slab. This causes light to reflect back into the slab of the side walls resulting in interference patterns as shown in Figure 5.9a.

The observation of these interference patterns suggests that the slab is relatively smooth and highlights that interference in the second FPZ is possible. Since this interference is essentially how MMI couplers operate, MMI couplers could potentially be quickly produced using the femtosecond laser direct write technique. Due to difficulties in accurately measuring the fibre input location compared to the slabs edge, interference was not used to retrieve the refractive index contrast of the slab.

Figure 5.10a shows an example of an end view of a 200 μm wide slab. The central guiding region appears to be smooth with no depressed cladding affecting light propagation. This

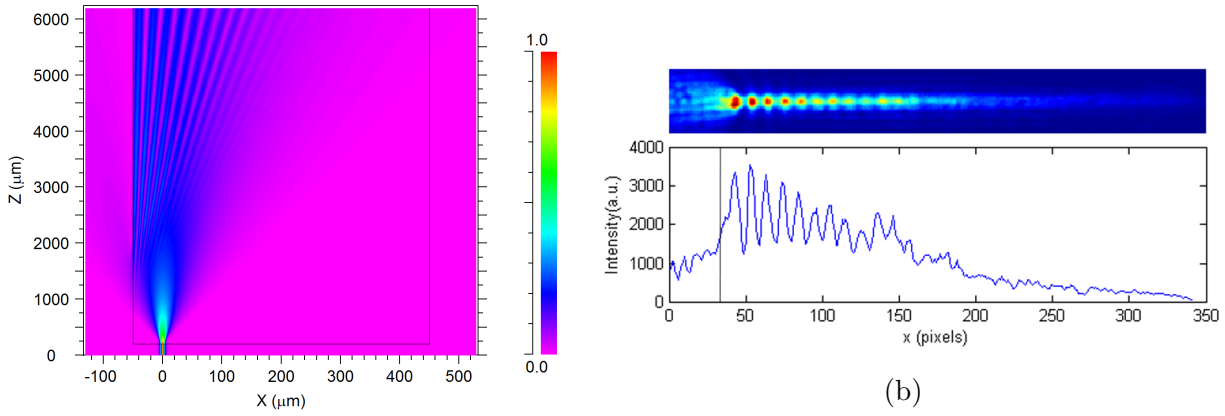

(a) (b)

Figure 5.9: (a) Simulated 2D amplitude distribution of the interference off the side walls when light is injected 50 μm from the edge of a slab. (b) Experimental edge interference within a slab waveguide of 0.4 μm multi-scan spacing. The black line represents the approximate position of the edge of the slab.

end on image shows small ripples along the top of the laser written region. It is believed that these ripples are either caused by the writing depth of the incident laser beam varying slightly over the 500 lines required to create the slab or slight changes in the waveguide size caused by laser fluctuations. The small ripples can also be seen in the slabs in the top-view DIC images as seen in Figure 5.10b, the small line variations close together can cause moire patterns in DIC images.

To evaluate the refractive index and the propagation of light, slabs of varying lengths ranging from $110 - 770$ μm were fabricated. To accurately inject light into the centre of the slab, the central multi-scan line within the slab was extended to act as a input waveguide (see Figure 5.10b). In Figure 5.10b the input boundary from single mode to slab waveguide is seen to be coarse, this is caused by mechanical shutter timing issues. Even though this looks like a surface that could cause scattering, no scattering was observed through the vision system. This implies that since the waveguide is formed as part of the slab, light transitions smoothly into the slab.

Figure 5.11b shows the near-field outputs from slabs of varying lengths. These near field outputs were then fitted with a Gaussian profile using a non-linear least squares fit, using this fit the FWHM was calculated with 95% confidence bound error bars. To calculate the refractive index contrast, RSoft's BeamPROP was used to model slabs of the same length (see Figure 5.11a) and the FWHM was calculated using the same method. The best fit for the refractive index contrast of the slab, to an accuracy of 1×10^{-4} due to model resolution, was given by a refractive index contrast of $\Delta n = 1.5 \times 10^{-3}$ with a 4 μm step index input waveguide (see Figure 5.12). It can be seen that the experimental data points follows the theoretical model closely. As only one data point was taken per slab length using individual slabs not a single polished back slab the variation is considerably small, and believed to be within 1×10^{-4}. A 4 μm step index was chosen as it accurately fits the output FWHM from a single-mode guide. Since the slabs measured are all independent, and

(a)

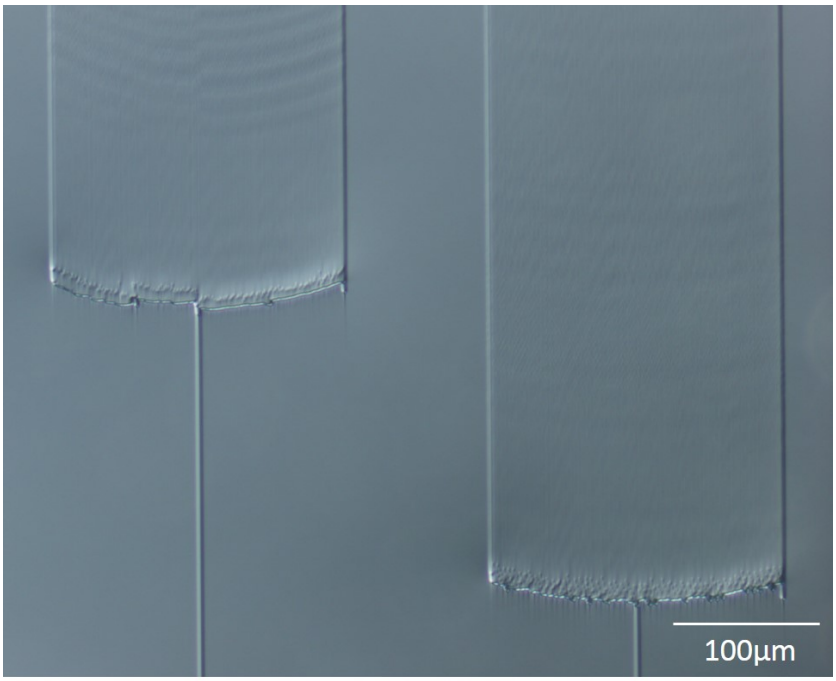

(b)

Figure 5.10: (a) End on view of a laser written slab waveguide.(b) Example of two slabs of different lengths viewed from the top. The features at the start of the slab are due to the mechanical shutter used to control the laser writing as the electro-optical modulation system was unavailable at this time.

the 170, 370, 570, 770 μm long slabs were written a few hours later on the same day using a slightly different pulse energy, meaning the index change was highly reproducible.

To ensure that the small structures in the raw output do not correspond to any fine refractive index variations within the slabs, the output needs to be compared to a refractive index cross section of the slab. Qualitative Phase microscopy [2] was used to obtain a refractive index profile. However, Qualitative Phase microscopy was unable to provide the accuracy required to get a meaningful refractive index profile of the slab as the fluctuations could not be resolved over the background, meaning the slab is smooth to an accuracy of 5×10^{-4} [124].

An alternative approach is to use a cross section from the DIC. The DIC however is known to only provide a gradient of the refractive index change. However using this method should give some valuable information when compare against the output profile. The variations

[2]QPm uses the inverse Abel transform of an qualitative phase image. To obtain a quantitative phase image one collects an in-focus image and very slightly positive and negatively defocused images [123].

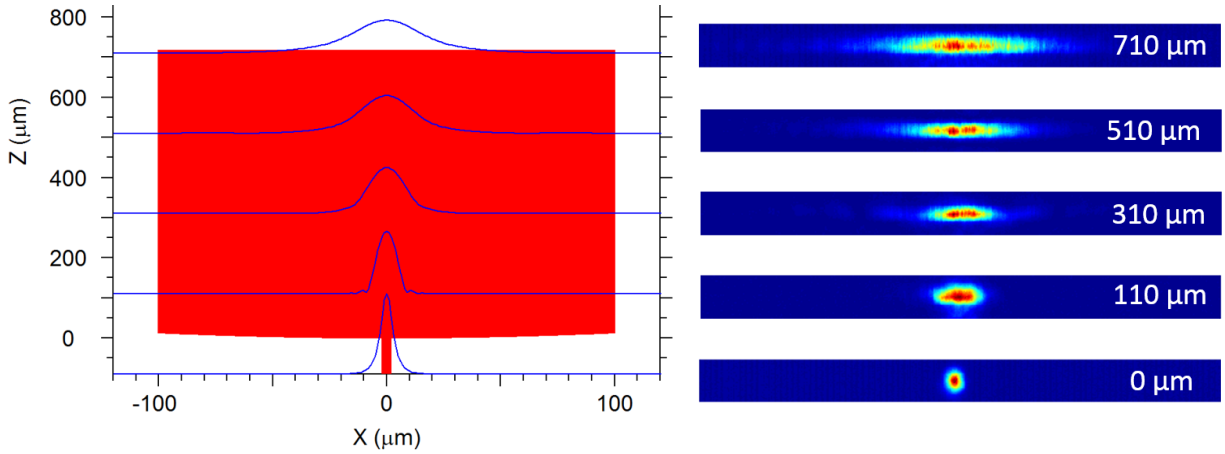

(a) (b)

Figure 5.11: (a) RSoft simulation showing the amplitude of light propagating in a slab. (b) Experimental results showing the near-field profile of slabs of different lengths. These correspond to the RSoft simulation lengths in (a). The slab lengths range from 0 μm eg. single mode guide output. and $110 - 710$ μm in 200 μm increments.

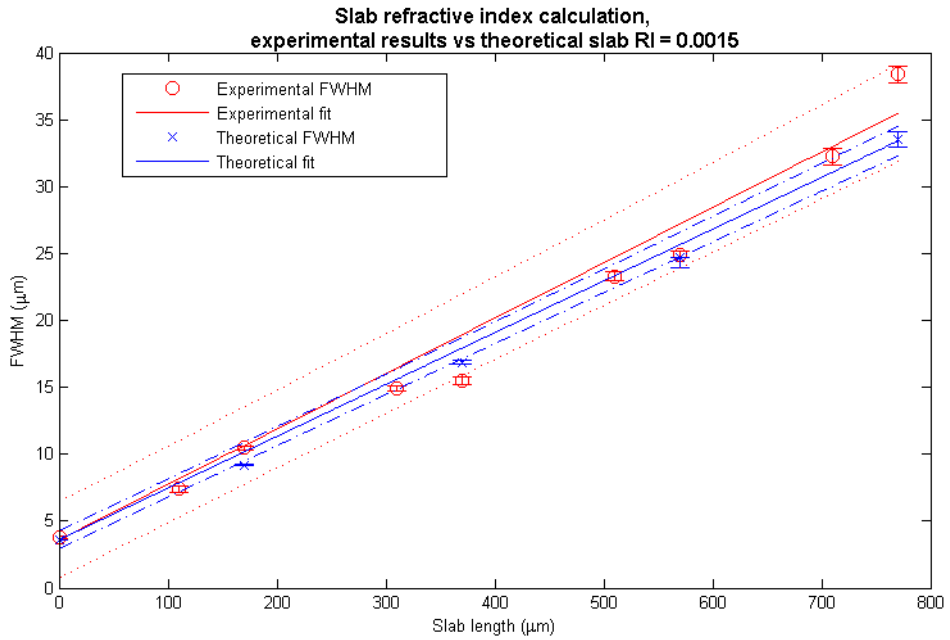

Figure 5.12: Using slabs of varying lengths, the near-field output was fitted with a Gaussian profile and the FWHM of the near-field was calculated. These FWHM values were then compared to theoretical FWHM values from slabs of the same length. A correlation was found when the slabs index contrast was 1.5×10^{-3}. A linear fit was taken instead of a parabolic fit because over such a small propagation distance a linear approximation of diffraction is acceptable. The dash lines represent 95% confidence bounds of the fit.

in the slab has no correspondence to the peaks and troughs in the output profiles, which are possibly due to surface errors at the output, (Figure A.1). Unfortunately we currently have no accurate measurement of evaluating the refractive index variations across the slab waveguide.

5.3 Waveguide tapers

5.3.1 Taper design

As discussed in Section 3.2, there are multiple taper designs that can be used to reduce the mode profile mismatch at the slab/waveguide array interface. The feasibility of fabricating these taper types was evaluated.

Vertical tapers are one of the most efficient tapers commercially available. Despite this, they are difficult to fabricate lithographically due to the height variation or index variation. Laser fabrication therefore has an intrinsic advantage in the creation of such structures. Laser fabrication has the ability to vary the size of the laser written modifications simply by changing the writing speed or the pulse power. However use of these techniques were limited for the chosen writing regime. In particular, since the fabrication is close to the heat accumulation threshold, increasing the writing speed or reducing the pulse power immediately causes the deposited energy per unit time and space to decrease below the energy associated with the cumulative heating regime. This would result in a sudden reduction in size and refractive index of the modification region, making a smooth height transition challenging. Even if the writing regime was further away from the threshold, reducing the size of the modification would also cause the waveguide overlap to decrease, which could affect the slab uniformity. Fabrication of vertical tapers could be possible using laser writing however they would be difficult to practically realise.

Segmentation is the main taper design used by industry, and could be inscribed using the laser writing technique. The issue facing the practical fabrication of a segmentation taper is the requirement to laser write multiple small areas of index modification with a high precision. Due to laser windowing restrictions [3], fabricating these structures on our laser writing set-up would be extremely challenging. Another issue for laser writing segmentation tapers is the formation of micro-voids [42], bubbles or defects that cause scattering i.e. a source of loss (see Figure 5.13a). These defects are believed to be a result of the sudden onset and offset of cumulative heating within the sample however the formation process is unknown.

Due to the fabrication difficulties associated with vertical and segmentation tapers, simple planar adiabatic tapers were chosen for laser inscription. A linear design was chosen for simplicity, however a parabolic adiabatic taper design is theoretically more efficient. The taper length was chosen by modelling the throughput of a simple taper at varying lengths. The maximum throughput was found for approximately 700 μm taper length (Figure 5.14a).

5.3.2 Taper fabrication

To create the linear adiabatic tapers as seen in Figure 5.13a, waveguides that form the slab were extended. The length of this extension is related to the lateral distance from the closest waveguide in the waveguide array, and the actual length of the total tapered

[3]The stages and the Pockels cell can be used in conjunction to allow laser writing within a certain area. This is an effective way to stop writing at a precise location. Unfortunately to set this writing area the stages must be stationary at a precise location, hence the fabrication of small consecutive modifications is extremely challenging to code as the stages much be stopped before each segment can be fabricated.

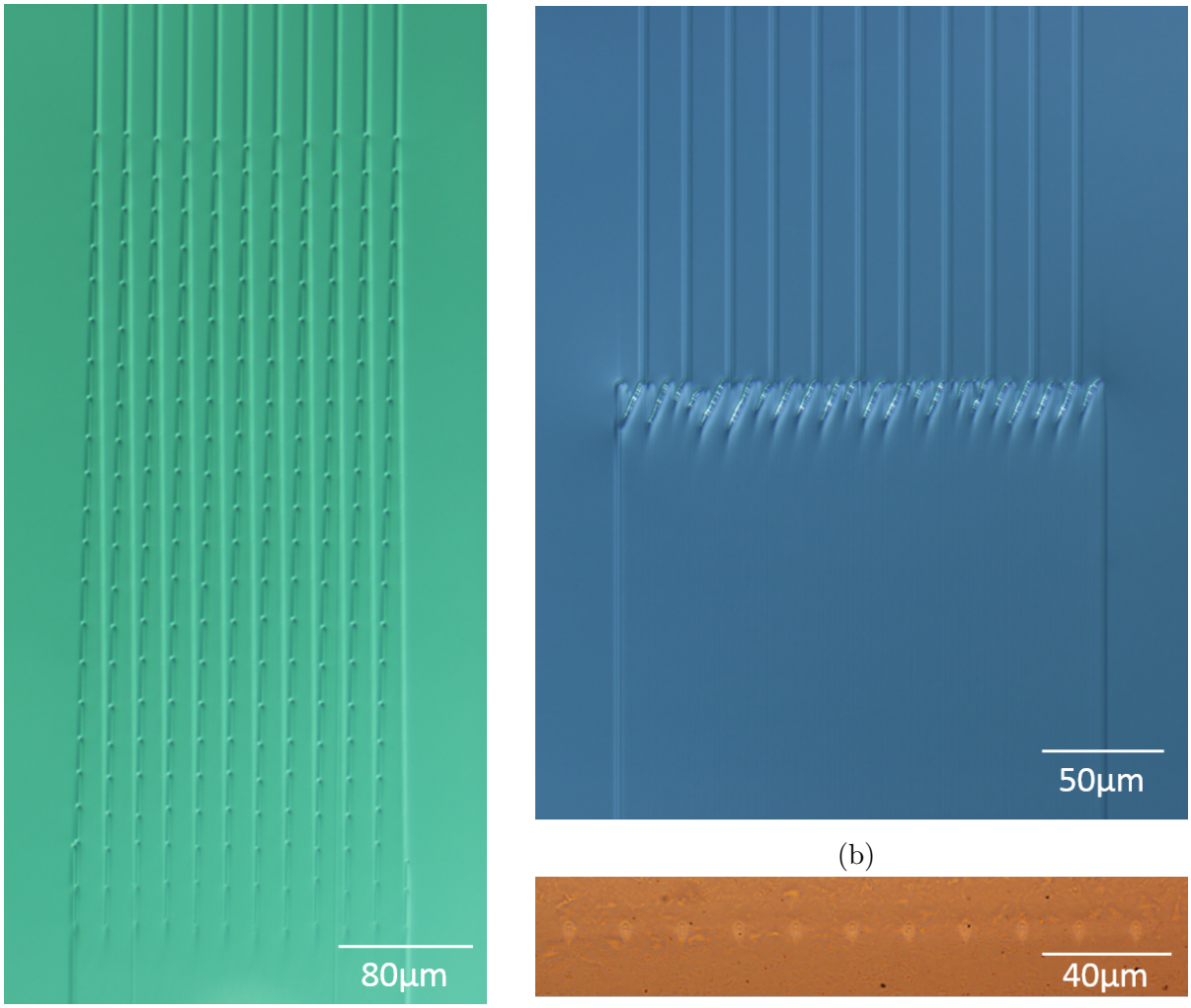

(a) (b) (c)

Figure 5.13: (a) Slab waveguide with linear adiabatic tapers improving the transition to the waveguide array. The small dots seen on the tapers are index defects caused by shuttering off the laser. (b) Slab with a waveguide array directly coupled to the end.(i.e. no tapers) (c) End on view of the output of the waveguide array. For (a) and (b), light is injected at the bottom of the page, it then diffracts within with slab waveguide and is coupled into the waveguide array with tapers (a) and without tapers (b).

region. The extended waveguides form a triangular extension to the slabs uniform refractive index contrast acting as a linear taper, funnelling the light into the waveguides. To test the effectiveness of laser written tapers in reducing the coupling loss at the slab/waveguide array transition, simple slabs where inscribed with 11 waveguides coupled to the end of the slab as seen in Figure 5.13b. These slabs were tested against slabs written with 11 untapered waveguides coupled to the end of a slab, Figure 5.13a.

In commercial AWGs the slabs have a curved output with tapers perpendicular to the curvature. However, for intial tests of the effectiveness of laser written tapers, slabs where

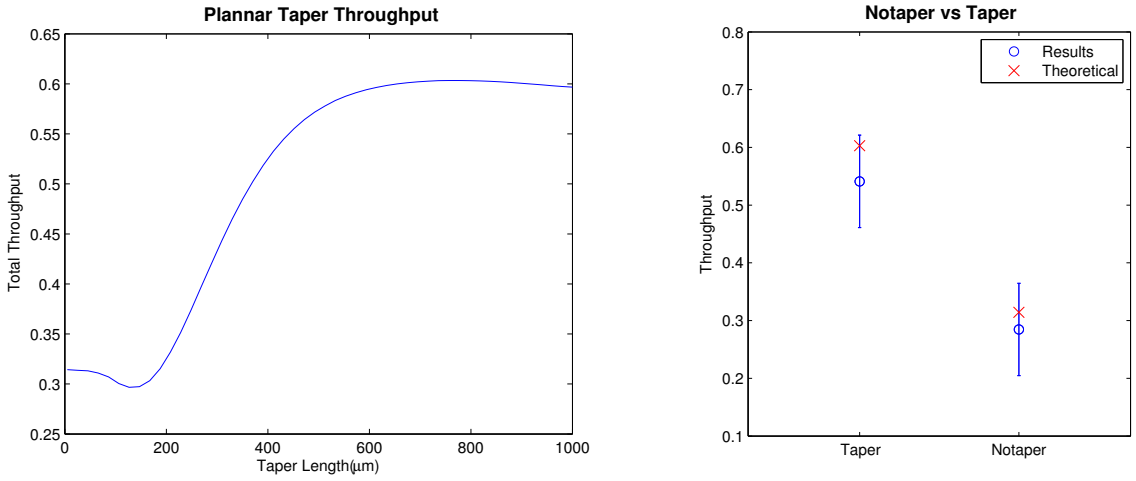

(a) (b)

Figure 5.14: (a) Shows the simulated throughput of a simple linear adiabatic taper of varying lengths, calculated using taper lengths of 1 μm increments. (b) Experimental results comparing the throughput of output guides from a slab with and without tapers.

fabricated with flat outputs and straight tapers for inscription simplicity.

Using the throughput measurement technique described in Section 4.3.4, the effectiveness of tapers was evaluated. Figure 5.14b compares the averaged experimental throughput of a slab with 2 sets of 11 output waveguides, either with or without tapers. The graph shows that laser written tapers improve the measured throughput by 80%. The simulated modelled throughputs were within uncertainties suggesting micro-voids are not a major source of loss.

5.4 FPZ

In the previous section, slabs up to 770 μm long were used to evaluate the refractive index contrast. These measurements only evaluated the propagation over a short slab length. While evaluating the effectiveness of tapers at the interface between the FPZ and waveguide array larger length were used as required for light to couple into multiple waveguides. Therefore slabs of $800 - 2000$ μm length were fabricated with coupled waveguides. The output profiles were compared to the simulated outputs, an example of a simulation can be seen in Figure 5.15. By comparing the results the accuracy of our simulation parameters can be assessed over a larger propagation length, gaining information about slab propagation characteristics as a function of length.

5.4.1 FPZ without tapers

Figure 5.16a shows a typical experimental output with the simulated output overlayed. The intensity of both plots has been normalised. This figure shows that the experimental and simulated positions of the peaks are aligned and the intensities of the coupling are similar.

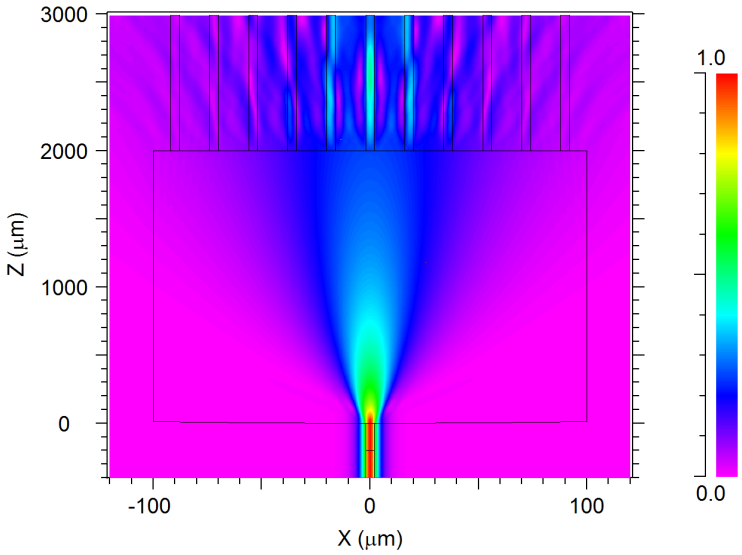

Figure 5.15: Simulation of light propagation from a slab waveguide into a waveguide array. light is injected from the bottom of the page and then freely diffracts within the slab region. Light is then coupled into the waveguide array. At this transition light that has not coupled into the waveguide array can be seen to continue diffracting between the waveguides.

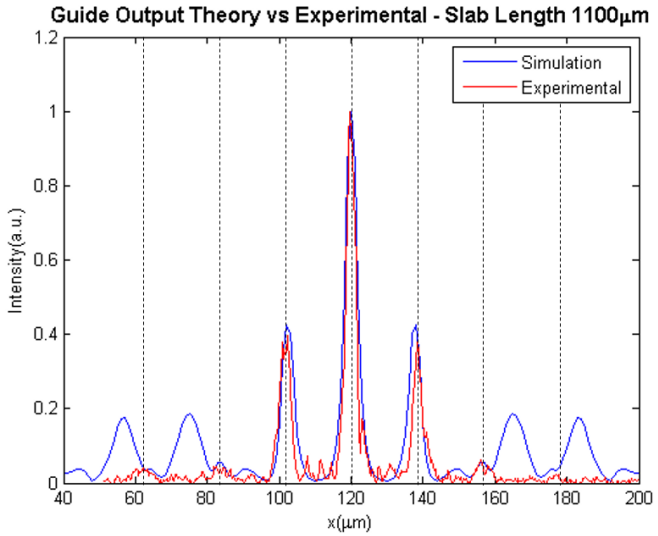

(a)

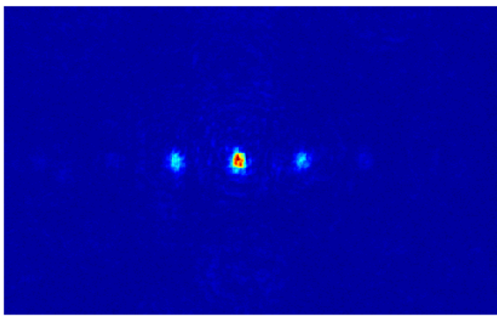

(b)

Figure 5.16: (a) Simulated and experimental intensity distribution recorded at the end of the waveguide array without tapers. The two plots have been normalised. The overlaid dotted lines indicate the location of the output waveguides. (b) Near-field image of the output from the same structure.

The corresponding near-field output is shown in Figure 5.16b, this is intended to aid the reader to interpret the observed output.

The simulated data shows large amount of light that was not coupled at the interface. This non-coupled light in reality is scattered by defects at the slab/waveguide interface shown in Figure 5.13b. The defects are caused by the use of a mechanical shutter instead of the Pockels cell.

As the waveguides are coupling light from a Gaussian profile, the peak intensity of light coupled into each individual waveguide should follow a Gaussian profile. By fitting the simulated and experimental data peaks with a Gaussian profile (Fig 5.17a) and calculating the full width half maximum (FWHM), a basic understanding of the diffraction of light within the slab can be inferred.

Since the diffraction rate within the slab is dependent upon the refractive index, the FWHM fit directly relates to the diffraction within the slab. Figure 5.17b shows the experimental and simulated FWHM plotted against different slab lengths. The simulated FWHM is larger than the experimental FWHM for larger slab lengths. This result suggests multiple possibilities. One possibility is that the coupling into the outer waveguides is more sensitive to the coupling angle than the simulation suggests. Another possibility is that the light within the slab is not diffracting as quickly as expected, this could be due to the refractive index of the slab being lower then previously calculated, which is the likely cause as variations of only 3×10^{-4} from the expected could account for this change. A further possibility is that the diffraction is being affected by small refractive index variations caused by the raster scan used to inscribe the index modifications.

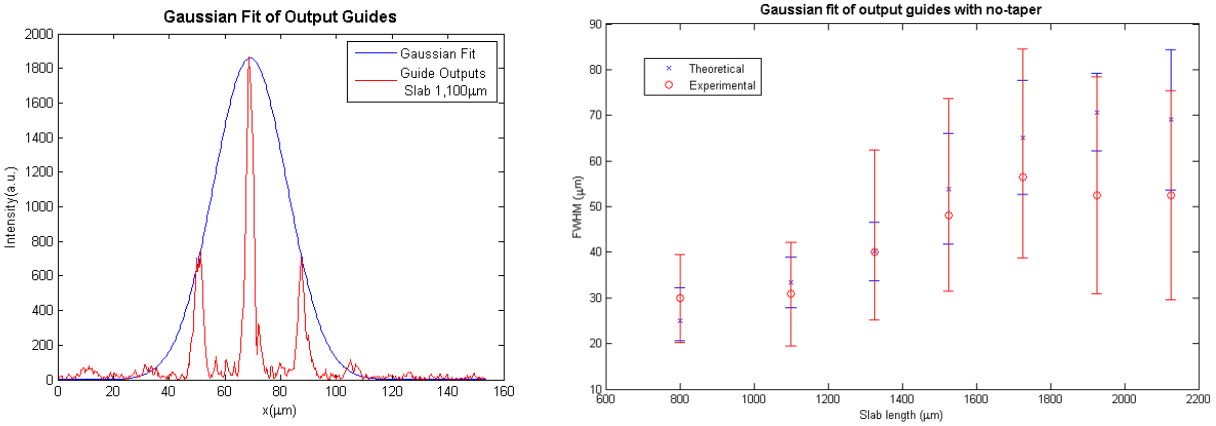

(a) (b)

Figure 5.17: (a) To evaluate the diffraction of light within the slab waveguide. A Gaussian fit is applied to the output waveguides peaks. This fit is used to calculate the FWHM of the output waveguide coupling. (b) This FWHM is then used to compare the experimental and theoretical FWHMs of non tapered couplers to evaluate coupling and diffraction of the slab at larger lengths. The error bars are 95% confidence bounds of the fit. As the Gaussian fit is using only $3-5$ points and only one measurement per point the errors are large.

5.4.2 FPZ with tapers

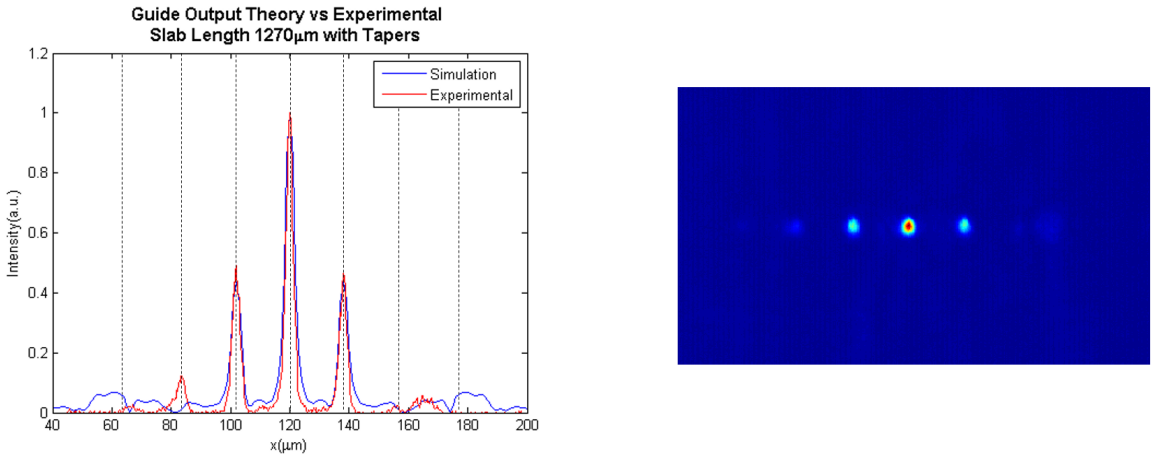

(a) (b)

Figure 5.18: (a) Graph showing the simulated and experimental intensity distrubution in the waveguide array for a device that had a slab/waveguide interface with tapered couplers. The two plots have been normalised to easily compare results. The overlaid dotted lines are positioned at the location of output waveguides indicated by the doted lines. (b) Shows the near-field output from the same structure plotted in (a).

Figure 5.18a shows the experimental output of a slab with coupling tapers. In contrast to the non-tapered results, the near-field output profiles show an improved agreement between the experimental and simulated values. This is due to the fact that at the slab/waveguide transition a larger portion of light is coupled into the waveguide array.

Once again the output profiles of the experimental and simulated data were fitted with a Gaussian profile and the FWHM recorded. Figure 5.19b shows the experimental and theoretical FWHM plotted against different slab lengths. In contrast to the results without tapers, the FWHMs are slightly larger than the theoretical results. This suggests that the refractive index of these slabs is slightly larger than the simulated values by approximately 1×10^{-4}. Since these slabs where written in the same sample on different days it could be possible that the refractive index of the slabs could varies slightly depending of the laser alignment. No action was taken to remeasure the refractive index of the slab as minor variations in the slab refractive index contrast 3×10^{-4} have only a minimal effect on AWG design [69]. Both FPZ with and without tapers showed results suggesting that the index variations are approximately within this range.

5.4.3 Tapers for AWGs

For a more complete analysis, a whole AWG structure was modelled to calculate the optimum taper length. Using a standard 41 waveguide AWG design, the throughput of each waveguide was measured for different taper lengths. Figure 5.20a shows that each waveguide has its own optimum taper length depending on the distance from the central waveguide, which is

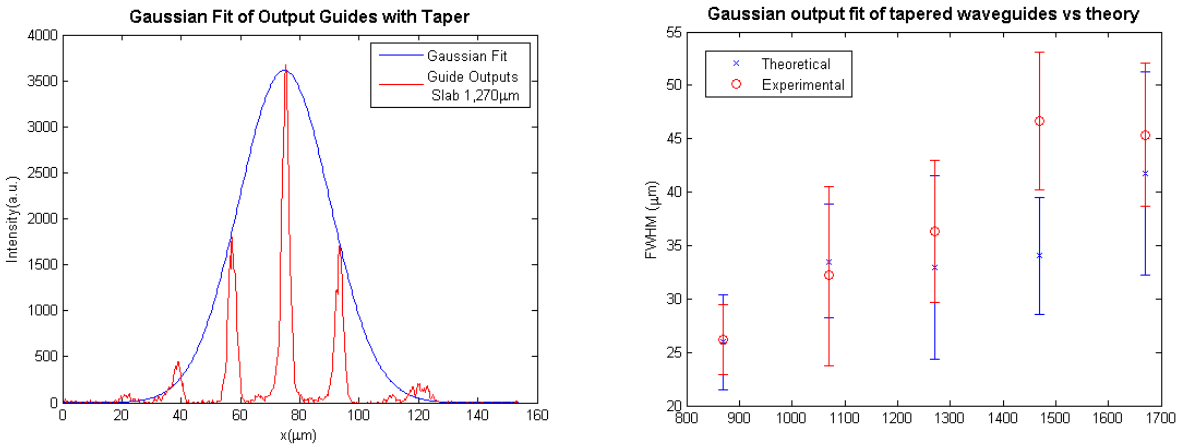

(a) (b)

Figure 5.19: (a) To evaluate the diffraction of light within the slab waveguide. A Gaussian fit is applied to the output waveguides peaks. This fit is used to calculate the FWHM of the output waveguide coupling. (b) The FWHM is then used to compare the experimental and simulated FWHMs of tapered couplers to evaluate coupling and diffraction of the slab at larger lengths. The error bars are 95% confidence bounds of the fit. As the Gaussian fit is using only $3-5$ points and only one measurement per point the errors are large.

represented by the white line. Therefore an AWG could be fabricated with each waveguide having an optimised taper length for maximum coupling. Such a design change is difficult to implement as the optimum taper length doesn't follow a simple function. For simplicity the taper length with the greatest throughput was calculated, as shown in Figure 5.20b. For this AWG design a taper length of 700 μm gives a total maximum throughput of 58%, which is close to the theoretical total maximum throughput of 60%. Since the fabrication of variable taper lengths have minimal impact on total throughput only a single taper length was used.

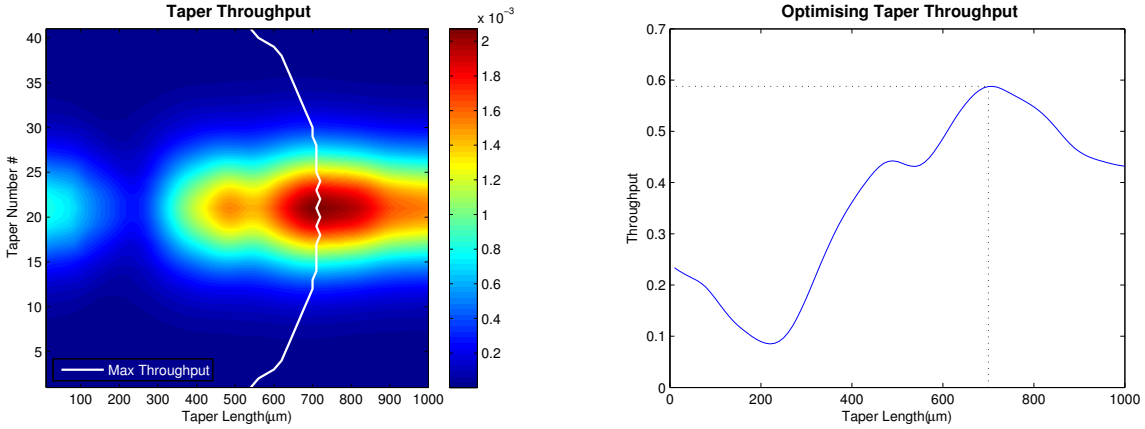

(a) (b)

Figure 5.20: (a) Shows the throughput of each taper in an 41 waveguide array AWG for different taper lengths. The white line represents the taper length that gives the highest throughput for each taper. (b) Shows the total throughput of an AWG FPZ/waveguide transition for a set waveguide taper length. A taper length of 700 μm was found to have a throughput of 58%.

"What we usually consider as impossible are simply engineering problems... there's no law of physics preventing them."

Michio Kaku

6 AWG fabrication

An AWG is a complex structure requiring large slabs, tapers and waveguide arrays to be fabricated to a high precision. Therefore the fabrication of a laser written AWG is a challenging task. This chapter briefly discusses the AWG G-code to control the stages followed by design and glass substrate challenges. Finally, preliminary results of a laser written AWG are presented.

6.1 AWG G-code

To enable the fabrication of complex AWG designs, a G-code algorithm was written that controls the motion control equipment. G-code is a common name for a widely used programming language used to control automated machining tools by simply telling the machine where to move and at what speed.

The G-code has been written to fabricate the AWG as a continuous structure, this has the advantage of making sure all transitions between slab and waveguides are uniform. Alternatively the FPZs and the waveguide array can be fabricated separately and stitched together. The major limitation of stitching is the formation of bubbles and defects at the slab waveguide transition. The advantage of stitching is the removal of tight bends at the slab to waveguide transition which are a source of stage position errors. Additionally it allows both FPZs to be fabricated separately, avoiding shutter restrictions.

For simple post processing the AWGs were designed with the output FPZ perpendicular to the edge of the chip. This simplifies the polishing process as the chip can be aligned perpendicular to a side edge and then polished back to the output surface for imaging the output spectrum.

For the interested reader, the complete AWG G-code is attached in the appendix. For completeness the following is a brief description of the variables required by the G-code, design and motion control restrictions.

6.1.1 Variables

The AWG G-code requires 9 key parameters taken from the RSoft AWG design utility. Using these parameters the complete AWG structure can be replicated (see Table 6.1).

Parameters	**Typical value**	**Description**
Slab width	800 μm	The width of the FPZ.
Number of waveguides	41	The number of waveguides in the waveguide array.
Waveguide spacing	18.4 μm	The spacing between waveguides at the input and output of the waveguide array.
Slab angle	10.3	Angle between the two FPZs.
Ro	6965 μm	The radius of curvature of the first FPZ output.
ΔL	8.4 μm	The incremental length change of each guide in the waveguide array.
Rz	30,000 μm	The radius of curvature of the first waveguide in the array.
Taper length	700 μm	The Length of the FPZ/waveguide linear transition taper.
Extra length	200 μm	Adds extra length between the two FPZs to enable the fabrication of a working design.

Table 6.1: List of parameters required by the G-code to fabricate an AWG.

6.1.2 Design restrictions

When using the AWG utility to design AWGs it is important to understand the intrinsic restrictions of the G-code in order to obtain usable parameters. The G-code is written symmetrically around the central axis of the slabs. At the central axis the input waveguide and the central waveguide of the array are written (shown as a white line in Figure 6.1). Therefore the number of waveguides in the array must be set to an odd value. The possible values for the waveguide spacing and the slab width are restricted to an integer value of the multi-scan spacing which has been set to 0.4 μm. This ensures waveguides can be written at the correct spacing and the FPZs have the correct width.

6.1.3 Stage movement

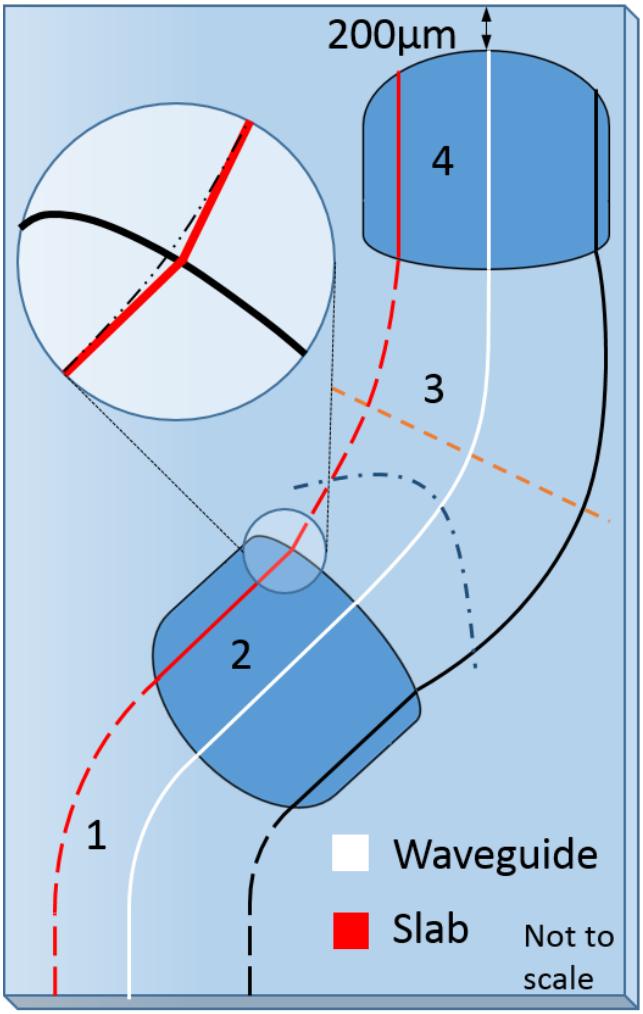

Figure 6.1: Geometry of laser writing. The red line represents the path taken when fabricating part of the FPZ and tapers. The white line represents the path taken when writing the input and central waveguide, in the waveguide array. The black line represents a typical written waveguide. The insert demonstrates the discontinuity at the interface between the FPZs and the waveguides or tapers. The black dotted line in the insert represents the smoothing of this transition made by the stages. The dark blue dashed line represents the stage stopping position to reset the shutter coordinates, while the orange dashed line represents the improved stopping position. Coloured dashed lines represent paths where no laser writing occurs or a virtual position.

To fabricate an AWG the stages follow the same path. For each pass the lateral offset of this path is increased, slowly building the FPZs/tapers (and the waveguide array when required) by switching the laser writing on and off at the appropriate positions. The basic path is illustrated in Figure 6.1. For each laser pass the shutter on and off position, radius of

curvature and extra length is calculated. The G-code uses two different subroutines that are implemented depending on whether an array waveguide is to be inscribed or another part of the FPZ is to be fabricated.

The slab subroutine is as follows (see red line in Figure 6.1). The stages move perpendicularly in from the edge of the chip. The length of this straight segment is calculated to position the output FPZ 200 μm from the chip edge. The stages then move in a circular arc aligning the writing direction parallel to the orientation of the first slab (1).

At the start of the first FPZ the shutter opens and the laser writing begins. The laser is translated through the sample to inscribe the first free propagation zone. At the end of the first FPZ the stages are translated perpendicular to the output FPZ curvature, forming part of the waveguide taper. The laser writing is then terminated via the Pockels cell at the end of the waveguide taper (2).

The stages continue to follow the red line in (3) to the virtual stopping position represented by a dark blue dashed line. At this point the stages stop and reset the laser shutter region for the second FPZ. The stages then continue to follow the red line to the input taper on the second FPZ. The input taper and second FPZ are fabricated in reverse to the first FPZ (4).

For array waveguides the stages follow the same pattern (see black line in Figure 6.1) except in Section (3) a continuous waveguide is constructed, with no shuttering or interruption to the motion of the positing stages. An exception to this occurs for the central waveguide where an additional input waveguide is written in Section (1) (see white line).

6.2 Integration Challenges

Integrating all the parts of an AWG is a challenging task. What follows is a brief overview of these challenges and how they were solved. At the slab/waveguide transition, waveguides are not parallel with respect to the slab axis. This non-continuous transition cannot be smoothly manufactured using mechanical stages at high translation speeds, as the stages require smooth continuous motion. If waveguides are written with no attempt to improve this transition, the stages position feedback mechanism over corrects for the position error at the transition resulting in the fabrication of wavy waveguides as seen in Figure 6.2b. To solve this issue a look-ahead filter was used to smooth the transition. The improved path taken at the FPZ/waveguide transition is shown in Figure 6.1 insert as a black dashed line. The issue with smoothing this transition is the effect it has on the waveguide array lengths. As this smoothing effect is larger in waveguides further away from the the central axis there is a possibility this could effect the phase delay of the waveguide array. Even though the delay would be minimal future work is planned to modelling this phase delay so it can be removed.

When using the laser windowing technique described previously, the laser must stop at a precise location to reset the laser writing coordinates before the second FPZ can be fabricated. This shutter/stage limitation means that great care has to be taken when operating the stages at high velocities of 2000 mm/min to make sure the stages stop smoothly. Initially the dark blue dashed line in Figure 6.1, was used as a position to reset the shutter coordinates. However this position was found to be unsatisfactory as it caused shuttering at

incorrect positions as seen in Figure 6.2a where the white dashed line represents the correct starting position for the taper structures.

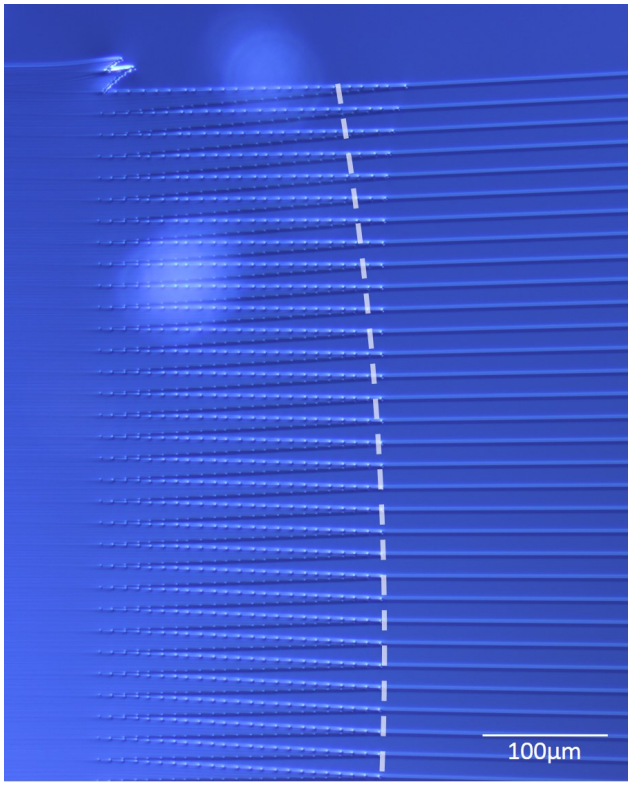

(a)

(b)

Figure 6.2: (a) Microscope image showing an example where the waveguide tapers start too early due to a poor placement of the shutter reset position, causing waveguides further away from the central axis to have an increased error. (b) The effect of non-continuous transitions on the waveguides within the array. The wavyness is caused by an over correction of the position feedback loop.

6.3 Challenges associated with the glass substrate

As discussed in Section 2.9, Eagle2000 is a technical glass made via a fusion drawing process. Since Eagle2000 is fabricated mainly as a substrate for LCDs, a ±10% variation in thickness and small surface errors are acceptable for its intended applications. These variations and surface errors can influence the ability to fabricate a working AWG prototype in three ways.

Surface flatness: As the devices themselves are 2.5 cm long, a small variation of 25 μm across the structure is enough so that the laser writing process can suffer variations due to spherical aberrations across the chip.

Surface imperfections: Small imperfections in the samples surface affect the lasers focusing conditions causing the incident energy density to decrease below that required for

the cumulative heating regime (see Figure 6.3a).

Dust particles: Dust particles are known to be a serious issue. Even after rigorous cleaning of the sample using fiberless tissues and acetone, the remaining dust particles can cause fabrication errors. When the laser passes over these dust particles the beam is obstructed reducing the power at the focus to below that needed for the cumulative heating regime (see Figure 6.3b).

These errors have been found to completely destroy the smooth propagation of light in the slabs and effectively stop guiding in the waveguide array. Therefore it is important that solutions to avoid these issues are discussed for future fabrication. To improve the surface flatness samples could be polished using a polishing Jig. The PP5 polishing jig (logitech, Scotland) available at Macquarie University can polish a sample to a total thickness variation of $\pm$ 1.5 μm, total removing any spherical aberration issues. Even after surface polishing surface imperfections could still be present due to impurities in the glass, however any surface imperfections from transport would be eliminated by polishing the sample. An alternative could be to fabricate AWGs in a higher grade of glass. The dust particles effecting fabrication are most likely due to particles within the air falling onto the sample over the large AWGs fabrication time(up to 3 hours). To remove this issue it has been proposed to construct a miniature clean room on the laser writing stages to reduce the possibility of dust fabrication errors.

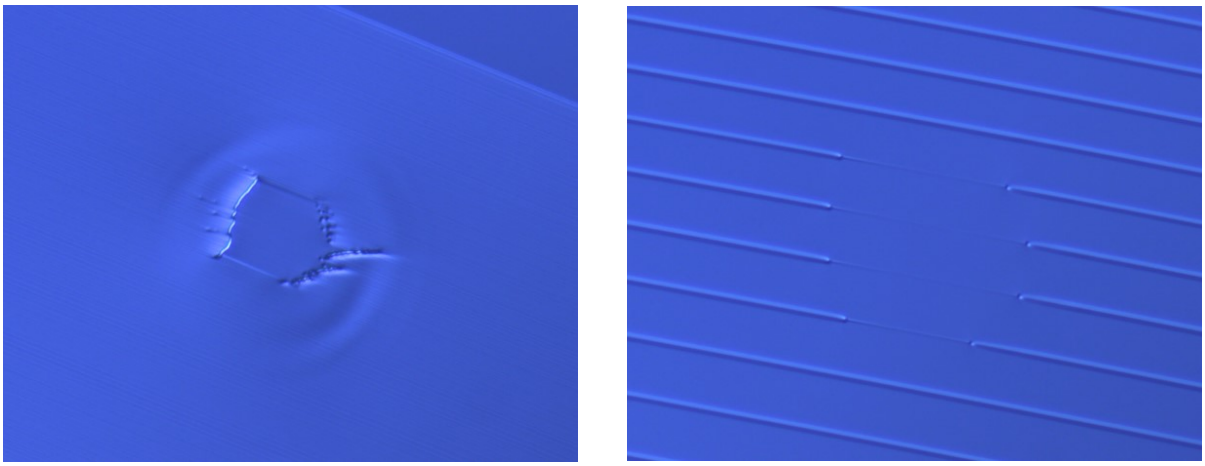

(a) (b)

Figure 6.3: (a) A small surface error within a FPZ. (b) A defect in the waveguide array caused by a dust particle blocking the laser beam.

6.4 First results

An initial AWG prototype was made with the following design features, a single input waveguide, a 7,000 μm long FPZ, 41 waveguides, and a minimum radius of curvature of 17,000 μm and no output waveguides. The output from the first laser written AWG prototype when

probed at 633 nm can be seen in Figure 6.4a and Figure 6.4b. The output contains three double peaks containing a large portion of the output power. This was initially thought to be a highly positive outcome as the simulated output (see Figure 6.4c) also has 3 main peaks corresponding to 3 different diffraction orders. However the output also contains other larger peaks making this similarity a coincidence. The output pattern however does appear to be an aperiodic interference pattern formed by various phase errors in the waveguide array. Interestingly, all the output power is concentrated within the central 400 μm of the output FPZ, and the single mode outputs shows no correlation to the input positions of the waveguide array into the second FPZ. This initial outcome is positive, as it demonstrates that some form of interference is occurring at the output FPZ. Demonstrating that with more characterisation and design improvements laser written AWGs could be a future possibility.

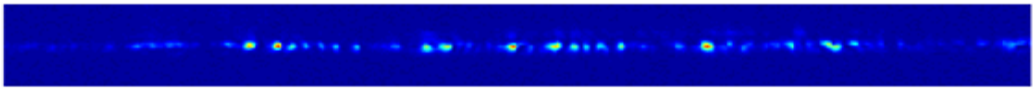

(a)

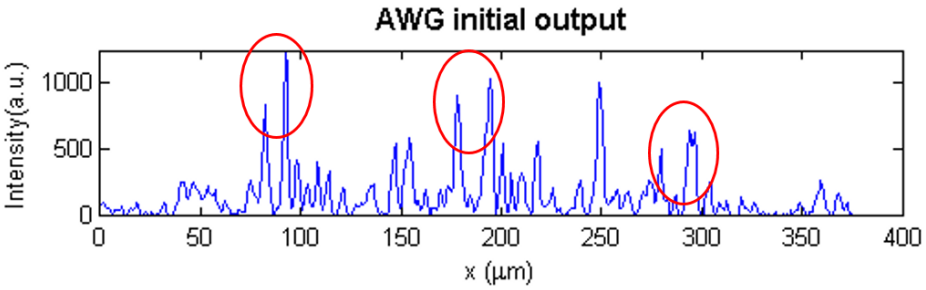

(b)

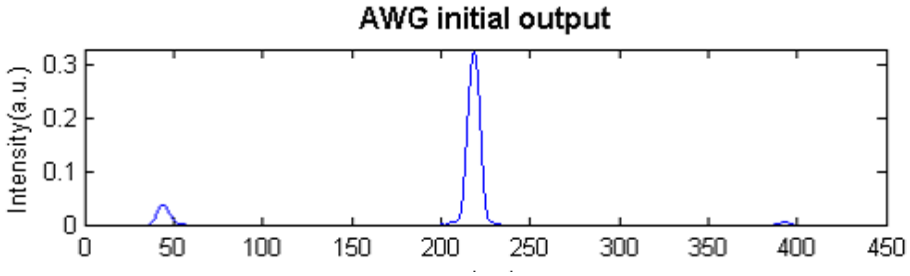

(c)

Figure 6.4: (a) Near-field output from the initial AWG design. It can be seen that the output has multiple single mode outputs. (b) A cross section of (a) showing multiple peaks. (c) Shows the simulated output of the AWG design.

6.5 Design improvements

6.5.1 AWG Losses

When light was injected into the first laser written AWG a large amount of scattering at an angle to the plane was observed, suggesting the loss was from the slab/waveguide array transition or from the waveguide array itself. For future AWGs it will be important to improve the design to reduce these losses.

Initially the minimum radius of the waveguide array was set to $17,000$ μm to reduce the footprint of the AWG. However it was found that this was extremely lossy. Therefore, the minimum radius of curvature was set to $\approx 27,000$ μm for future AWGs. The tapers are formed with multiple waveguides all orientated perpendicular to the FPZs radius of curvature. When long tapers are fabricated the waveguides fanout towards the end of the taper. Therefore light is guided out of the tapers, instead of coupling light into the waveguide array. To improve the taper spreading issue, a constant angle for each waveguide within the taper was calculated. A schematic is shown in Figure 6.5 illustrating this concept.

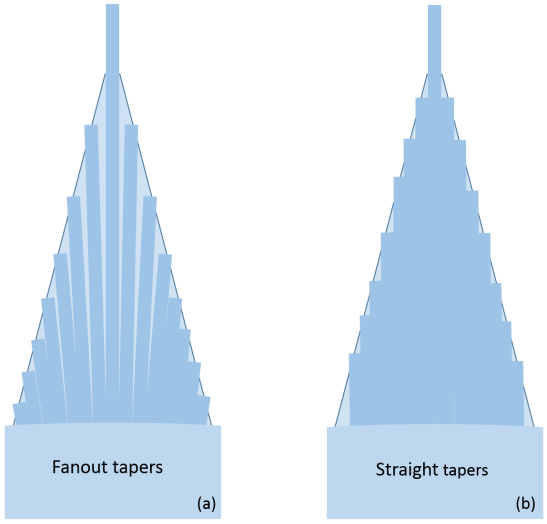

Figure 6.5: Schematic showing an exaggerated example of the waveguides fan-out when fabricated perpendicular to the FPZ curvature (a) and an example of how using parallel waveguide to fabricate the tapers reduces this problem (b).

6.5.2 Further design improvements

As seen in Figure 6.6a, the first AWG prototype had multiple fabrication errors. By improving these fabrication errors it was hoped that the AWG performance would be enhanced. Following is a brief description of how two fabrication errors have been improved.

A major error seen in Figure 6.6a (see white ovals) is the regions to the left and right of the FPZ. To improve this error the stages for these regions are now programmed to move from the start of the first slab in a straight line to an interception position between the two

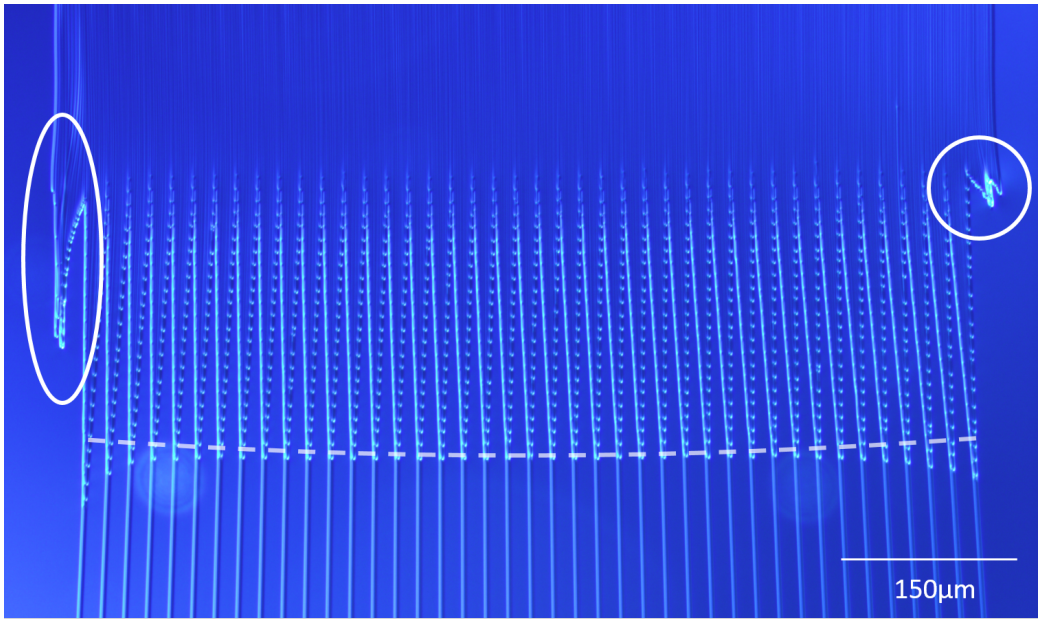

(a)

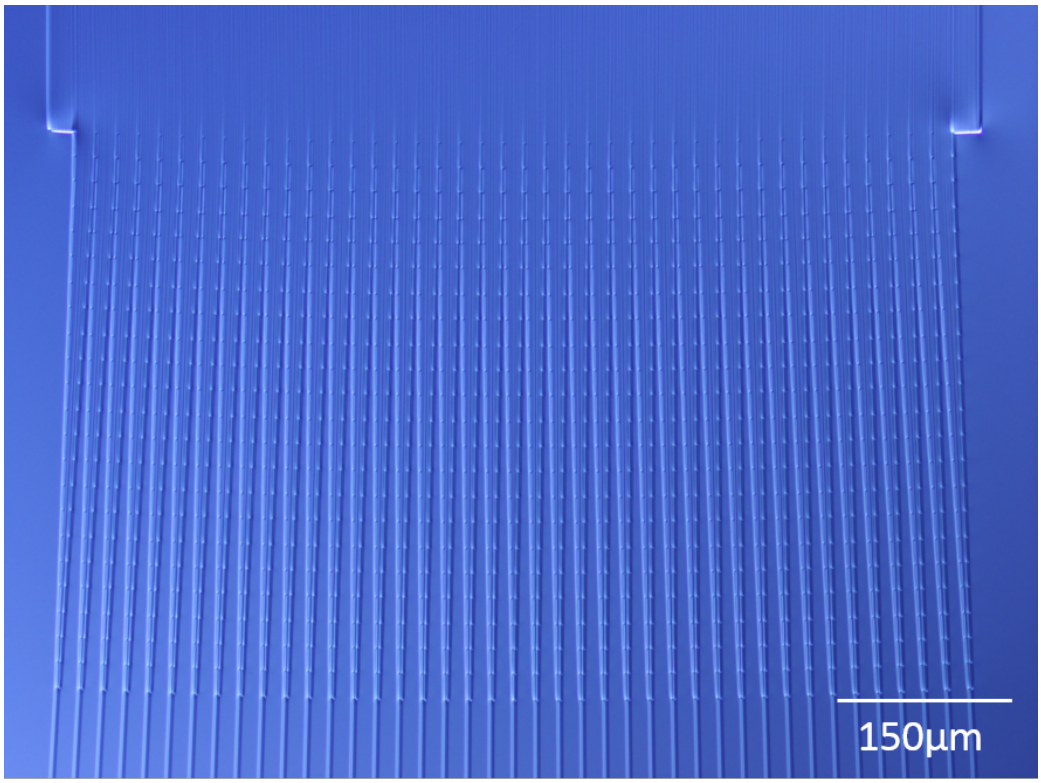

(b)

Figure 6.6: (a) Initial AWG design, waveguide array/ output FPZ transition. The white circles highlight large fabrication errors, the white dashed line displays the approximate correct curvature. (b) Improved AWG design, waveguide array/ output FPZ transition. the errors highlighted in (a) are no longer visible.

FPZ, represented as an orange dashed line in Figure 6.1. At this central position the stages stop and reset the laser window to trigger on for the second FPZ. Stages then move straight to the edge of the chip.

To solve the shutter reset position errors, the same concept as the outer slab regions above was used by using a virtual intercept position represented again by the orange dashed line. At this location the stages can slowly and accurately stop to reset the laser writing coordinates for the second FPZ and taper. Figure 6.6b shows how this correction improved the design.

6.5.3 Improved AWG device output

Using the same parameters as the initial design (except for a larger radius of curvature and a larger taper length) new improved AWG devices,(seen in Figures 6.7a and 6.7b) were fabricated and probed with 633 nm. The improvements to the AWG design had no positive effect on the AWG output, however a larger throughput was visually observed. On reflection, these result have provided valuable information for potentially improving AWG devices and designs further. The output is seen to have a periodic structure, however the number and positions of the outputs are not related to the waveguide array positions thus individual guiding within the slab region was immediately ruled out. Again it appears the output is an interference pattern meaning there is definite phase errors within the waveguide array. One major change from the previous designs is the increased minimum radius of the waveguide array. This has increased the length of the waveguide array increasing the chance of phase array errors. The phase errors within the waveguide array are now most likely due to small changes in the refractive index and small changes in the waveguides widths not length as the design improvements have ensured the waveguide array is fabricated to a higher (length) position accuracy. Therefore it appears only small changes to the refractive index or size of the waveguides could be affecting the designed phase delay, leading to the interference patterns observed in both AWG outputs.

6.6 AWG fabrication summary

The fabrication of a working laser written AWG has currently not been demonstrated. However this chapter has demonstrated that all the necessary parts of an AWG can be integrated onto a single chip. Table 6.2, illustrates that all the key components of an AWG can be manufactured. However, it has been seen that the final requirement to fabricate an AWG is understanding the phase within the waveguide array. By measuring the output phase of each array waveguide it is hoped the cause of the phase errors can be determined. Using this information the AWG design could be improved or a post tuning process could be utilised to correct the phase errors.

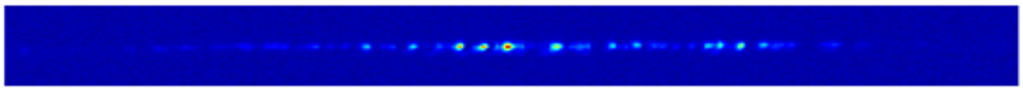

(a)

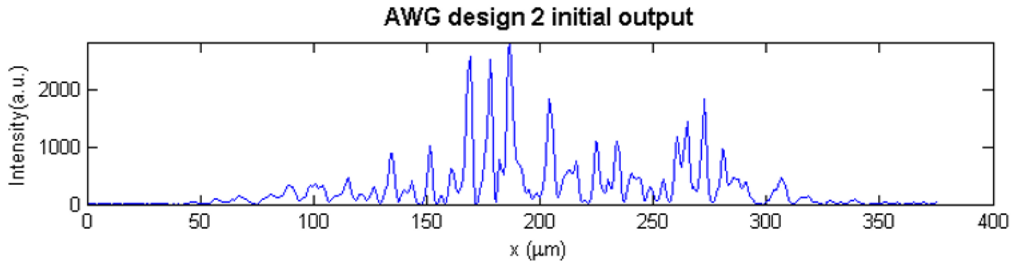

(b)

Figure 6.7: (a) Output from the improved AWG design. (b) Cross section of the output in (a). The outputs have an interference pattern caused by phase errors within the waveguide array.

Component	Outcome	Description
FPZ	✓	Fabrication of smooth refractive index regions that act as FPZs have been demonstrated.
Tapers	✓	Laser written tapers have been shown to effectively improve the coupling of light into a waveguide array.
Waveguide array	✓	Output profiles from waveguide arrays have shown effective single mode coupling of light into multiple waveguides. Improvements to the G-code have ensured that each waveguide in the waveguide array has been fabricated with the correct length and delicate curvature requirements.
Integration	✓	The simultaneous fabrication of all key components of an AWG simultaneously has been demonstrated to the high position accuracy required. However it appears other fabrication properties have restricted device functionality.
Phase	✗	Initial output results indicate that accurate phase control within the waveguide array, to the accuracy required to fabricate a working AWG device, has not yet been achieved. However, since waveguide array fabrication has been shown to such high accuracy, laser stability and post processing maybe required to acheieve the required phase control.

Table 6.2: Shows the current fabrication state of different AWG components.

7

Conclusions & future work

In this thesis the feasibility of femtosecond laser written AWGs in a glass substrate for spectrographic purposes was explored. To make an AWG three key components must be fabricated; a FPZ, FPZ/waveguide tapers and waveguides for the waveguide array. Since there is minimal previous work on laser direct write fabrication of FPZs, initial efforts where focused on the formation of smooth slab waveguides that could act as a FPZ.

Initial slab fabrication was attempted in two different kinds of fused silica, Suprasil 1 and HPFS 7980. Fused silica was chosen as a suitable substrate for two reasons. Firstly, fabrication of slabs has previously been shown in fused silica. Secondly, high OH content fused silica enabled visualisation of light propagation due to the formation of colour centres. Waveguides were successfully inscribed in both glasses and fluorescence was observed in waveguides fabricated with repetition rates ranging from 250 kHz to 5.1 MHz. Unfortunately the waveguides fabricated with our laser set-up in these glass types were extremely lossy. Therefore a different glass was chosen which is known to be suitable for the available laser system.

Eagle2000 was selected as a substrate for laser written slabs. Eagle2000 has been previously shown to be well suited to waveguide writing at 5.1 MHz repetition rate. This high repetition is beneficial as it allows for fast translation stage speeds which can fabricate large devices such as AWGs in only a few hours. Slab waveguides were written in a strongly cumulative heating regime. Slabs were created by overlapping waveguides with a separation of $3-7$ μm. Slab waveguides fabricated in this regime had the issue of a depressed cladding causing light to be individually guided within the slab. To eliminate the depressed cladding, a regime just above the cumulative heating threshold was chosen. Single mode waveguides were inscribed using an Olympus 40 $\times$, 0.65 NA focusing objective, a translation speed of 2000 mm/min at approximately $53-55$ nJ pulse energy. Using the same parameters, a multi-scan method with spacings ranging from $0.3-0.8$ μm, was used to fabricated 500 μm wide and 6 mm long slabs. Light was then injected into these slabs and the near-field output

was observed and compared to Gaussian fits. From these results slabs of 0.4 μm spacing was chosen as it exhibits a smooth Gaussian propagation. Using this spacing slab waveguides of varying lengths($110 - 770$ μm) were fabricated and the near-field output was fitted with a Gaussian. The diffraction (as a function of slab length)was then used to evaluate the refractive index contrast, which was found to be $1.5 \times 10^{-3} \pm 1 \times 10^{-4}$. This development enables the fabrication of devices that require large areas of smooth refractive index to be fabricated via laser direct write at an unprecedented rate.

To create FPZ/waveguide tapers, waveguides that form the FPZ were extended to form a linear adiabatic taper, enabling the slab mode to be smoothly coupled into multiple single mode outputs. These laser written tapers were found to increase the coupling efficiency by 80%, matching the simulated improvement in throughput. FPZs and tapers were then compared to simulated waveguide coupling and found to show a strong correlation.

Finally the ability to integrate all the components to fabricate a complete AWG was investigated. Integrating the different components involved solving various stage and material limitations. However, it was shown that a complete laser written AWG can be inscribed to match the design to a high precision. The AWG took approximately 2.5 hours to manufacture, and is approximately 3.7 $\times$ 2.7 cm and is designed to have a FSR of 40.5 nm, centred at 633 nm and an R of 440. Initial outputs from the first laser written AWG of 632.8 nm showed an interference pattern, unfortunately this interference pattern was aperiodic and not the pattern expected from a working AWG of these specifications. However, due to the high precision of the AWGs waveguide array waveguide lengths. It is believed that the incorrect output interference pattern is caused by phase errors in the waveguide array. These phase errors are believed to be a result of refractive index variations within the waveguide array. At this stage the phase errors have not been investigated.

7.1 Future work

This thesis has opened the potential for a large sweep of future work, however the discussion will be limited herein to just AWG applications. To help reduce the small variations in waveguide size and refractive index seen in the FPZs and the waveguide array, laser stability must be improved for future work. Actively stabilising the average output power of the laser could potentially reduce these issues and remove a possible source of phase errors. Modelling is also planned to improve our understanding of phase error tolerances. To improve the writing speed multiple laser spots created by a spatial light modulator. This could effectively half the writing time by using two spots, reducing the susceptibility to fewer laser fluctuations. A key problem that needs to be be investigated are the phase errors in the waveguide array. To do this it is planned to remove the output FPZ and evaluate the array output in free space. After the phase errors have been characterised, post tuning techniques similar to UV trimming could be trialed using the laser writing set-up in order to fine tune the refractive index in each waveguide. If such a technique enables the fabrication of working laser fabricated AWGs, there is possibility to extend the idea to the fabrication of birefringent corrected AWGs and different flat focal field output designs. Another fabrication difficulty that could be improved in future work is the refractive index bubbles seen in the tapers that could be causing small losses. Instead of abruptly switching the laser writing off, a smooth

power transition to one that drops below the threshold for the cumulative heating regime could reduce this fabrication error.

Once a working laser written AWG is demonstrated there are multiple applications including quick prototyping of astronomical AWGs for on-off observations at specific wavelengths. Laser written AWGs also have the possibility to be coupled with other laser written integrated photonic devices such as photonic lanterns and OH suppression Bragg gratings, on a single monolithic chip. Laser written AWGs also have great potential for sensing applications with the possibility to integrate micro-fludic channels on the same substrate.

In this thesis AWGs were fabricated with a central wavelength of 632.8 nm. This wavelength was initially chosen for slab guidance, characterisation ease and the potential for visible sensors. However the inscription of AWGs in the visible spectrum require a high precision. It is speculated that further writing studies in the strongly cumulative heating regime with a smaller multi-scan spacing could allow slabs to be written with a higher refractive index contrast and guidance at telecommunication wavelengths. Fabrication of laser written AWGs could have a future potential for cheap multiplexers and demultiplexers for specialised applications.

A An Appendix

A.1 Rowland Curvature

For the readers benefit how the Rowland curvature is calculated is shown below. The FPZ parameters can be solved using the wavelength dispersion equation (3.8). To solve this equation $n_g \approx n_a$, where n_g & n_a are the group refractive index and array refractive index. This approximation however does not account for the slab and waveguides having a different refractive index contrast.

$$\frac{\partial \theta_o}{\partial \lambda} = \frac{m}{dn_s} \tag{A.1}$$

Then if the FPZs are identical, Equation's (3.3) & (3.4) can be combined to give: $\theta = \frac{\Delta x}{L_f}$. Allowing the Output Rowland curvature can be solved:

$$R_o = L_f = \frac{n_s \Delta x d}{m \Delta \lambda} \tag{A.2}$$

The input radius is then defined as half R_o.

A.2 Beam Propagation Method

By assuming a scalar field the wave equation can be written as the Helmholtz equation for a monochromatic wave.

$$\frac{\partial^2 \phi}{\partial x^2} + \frac{\partial^2 \phi}{\partial y^2} + \frac{\partial^2 \phi}{\partial z^2} + k(x,y,z)^2 \phi = 0 \tag{A.3}$$

The scalar electric field has been written as $E(x,y,z,t) = \phi(x,y,z)\, e^{-i\omega t}$ and using the notation $k(x,y,z) = k_o n(x,y,z)$ with k_o being the wavenumber in free space. Next a slowly

varying field u is introduced. $\phi(x,y,z) = u(x,y,z)\, e^{i\bar{k}z}$, this is used to factor out the rapid phase variation in the propagation direction. Where $\bar{k}$ is a constant value chosen to represent the average phase variation of the field.

$$\frac{\partial^2 u}{\partial z^2} + 2i\bar{k}\frac{\partial u}{\partial z} + \frac{\partial^2 u}{\partial x^2} + \frac{\partial^2 u}{\partial y^2} + \left(k^2 - \bar{k}^2\right) u = 0 \tag{A.4}$$

Now it is assumed that the variation of u with z is sufficiently slow, so the first term can be neglected. This is known as the slowly varying, paraxial or parabolic approximation as referred to earlier.

$$\frac{\partial u}{\partial z} = \frac{i}{2\bar{k}}\left(\frac{\partial^2 u}{\partial x^2} + \frac{\partial^2 u}{\partial y^2} + \left(k^2 - \bar{k}^2\right) u\right) \tag{A.5}$$

This is the basic BPM equation in 3D, Since typical AWGs have no circuitry change in the 3rd dimension, the above equation can be reduced to 2D by omitting any y dependence. The equation can now be given an input field (typically a Gaussian input field from a SMF) and the propagation of the field in the z direction will be calculated.

A.3 Slab Variations

A.4 G-code

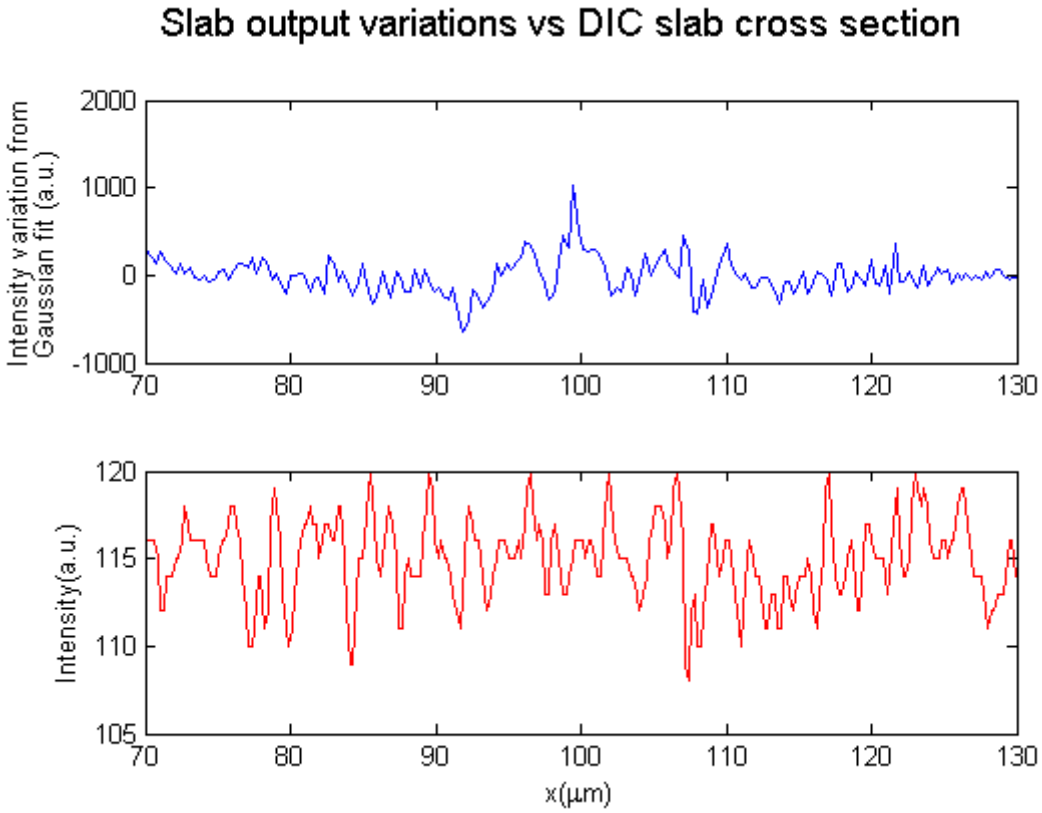

Figure A.1: Compares the variations in a slabs output to a cross section taken from a DIC of the same slab. The figure shows that the variations in the slab are small and do not appear to be related to the variations in the output. The slabs output is from $80 - 120$ μm.

```
; VARIABLES
; units are in mm and feedrate in mm/min
;-----------------------------------------------------------------
;-----------------------------------------------------------------

SampleLength   = 41                     ;Sample length
LeadInOut = 0.5                         ;line before and after the sample
WaveguideDepth = 0.17/1.505             ;waveguide writing depth.
FilterConstant = 16                     ;in ms for exponential filter for velocity profiling
EdgeBoarder = 0.1                       ;the distance inside the sample before writing begins, to avoid laser tapering.
DistanceFromRightEdge = 0.5             ;distance input waveguide is from edge of chip.
WaveguideSpacing = 0.02                 ;inital spacing of scale guides.

SpeedGroupSpacing = 1.2                 ;Spacing of the Speed group/spacing between AWGs
PowerGroupSpacing = 0                   ;Spacing of the Power group
FinalSpacing = 0                        ;Spacing at the end (additional to previous ones)

NumberSpeeds  = 1                       ;Number of parameters for spacing
NumberPowers  = 2                       ;Number of power sets U8-12.5 mW: 255 278 302

;;bringt plasma at p1
; strong tracks visible

;Broad area waveguide parameters
GeoSlabWidth = 0.800                            ;Width of the slab
GeoNumberOfWaveguides = 41                      ;number of wavguides
GeoLineSpacing = 0.0004                         ;spacing of the lines, geowaveguidespacing and this need an intiger rela
GeoWaveguideSpacing = 0.0184                    ;spacing of the waveguides at the output of the slab.--varry to get intig

GeoSlabAngle = 7.7                      ;angle from rSoft: a value in glens code
GeoCurvatureRadiusSlab1Out = 6.9299
GeoDL = 0.006723556851                          ;parameter DL from rSoft
GeoRz = 70                                              ;parameter Rz from rSoft
GeoTaperLength = 0.5                            ;taper length from Rsoft

TaperExtra = 2*GeoTaperLength                   ;changed so taper length defined the same as rsoft.

Lextra = 0.5                                    ; adds a length to the awg, A will need to be changed if varied. increas

GeoRadius2 = 30                                 ; =R2: radius of the waveguides in section 2

ParamInitialPower = 15                  ; power found from power scan. 293mW 10.7
ParamPowerIncreaseFactor = .1                   ; addition
ParamInitialSpeed = 2000                ; writing speed -- NORMALLY 2000
ParamSpeedIncreaseFactor = 1            ; multiplication
```

```
;-----------------------
;Calculations
Length = 2*LeadInOut + SampleLength
SpeedGroupSpacing = SpeedGroupSpacing + GeoSlabWidth


; MAIN PROGRAM
;---------------------------------------------------------------------
;---------------------------------------------------------------------

;ROT X,Y,DEG(ATN(-0.01928/6.7000))

G92 XZY                                         ;Sets actual position to zero
G91                                             ;Incremental

WINDOW 1 DISABLE
WINDOW 2 DISABLE
FIRE OFF                                        ;Reset

;set the zero position to be the right bottom of chip, then moves to a position outside the chip and too writing depth.
G1 X DistanceFromRightEdge Y -LeadInOut Z WaveguideDepth F100

;now set this position as new home position
G92 XYZ

;set initial power
Power = ParamInitialPower

;need to write some waveguides just as a marker/scale. only needed once in a sample.
;SUBROUTINE: SCALE_WAVEGUIDES
;laser should now be 160um away from last scale line
;set this position as new home position
G92 XYZ


MESSAGE FILE (coordsOfLastProcess.txt,w) "Start writing AWG"

;start powerscan loop
LOOP NumberPowers
        ;set inital speed
        Speed = ParamInitialSpeed
        ;start speed scan loop
        SUBROUTINE :LASON

    LOOP NumberSpeeds
                ;calculations for the slab
                SUBROUTINE :CALCULATIONS_AWG
                SOFTWARE POSITION XY
```

```
LOOP NumberSpeeds
        ;calculations for the slab
        SUBROUTINE :CALCULATIONS_AWG
        SOFTWARE POSITION XY

        LOOP (2*UtilNumberOfLines +1)
                SUBROUTINE :LASON
                ;Calculations for each line
                SUBROUTINE :CALCULATIONS_LINE

                IF ((UtilCounter >= -(UtilPositionOfOuterWaveguide+0.5*UtilWaveguideAtEveryLine)) && (UtilC
                        ;continuous lines including starting line, slab1, waveguides, taper, and excitation
                        IF UtilModulo = 0 THEN
                                ;connecting lines and starting line
                                IF UtilCounter = 0 THEN
                                        ;starting line
                                        ;setting shutter coordinates, overwriting values from calculations subr
                                        UtilLaserOnCoordinateY = LeadInOut + EdgeBoarder
                                        UtilLaserOnCoordinateX = CX0

                                        ;laser off is now end of slab2
                                        UtilLaserOffCoordinateY = LaserOff2
                                        SUBROUTINE :WRITE_WAVEGUIDE
                                ELSE
                                        ;waveguides
                                        ;laser off is now end of slab 2
                                        UtilLaserOffCoordinateY = LaserOff2
                                        SUBROUTINE :WRITE_WAVEGUIDE



                                ENDIF
                        ELSE
                                ;this is a taper line.
                                ;taper slab1
                                UtilLaserOffCoordinateY = CY42
                                ;no taper on 1st slab
                                ;UtilLaserOffCoordinateY = CY3

                                ;taper slab2
                                LaserOn2 = LaserOn3
                                ;no taper on 2nd slab
                                ;LaserOn2 = CY7

                                SUBROUTINE :WRITE_SLAB

                        ENDIF

                ELSE
```

```
                    ELSE
                        ;outer slab - 1st slab finish
                        UtilLaserOffCoordinateY = CY3
                        ;outerslab - 2nd slab start
                        LaserOn2 = CY7

                        SUBROUTINE :WRITE_OUTER_SLAB

                    ENDIF
                    UtilCounter = UtilCounter + 1

                NEXT
                SUBROUTINE :LASOFF

                ;move to home position
                G1 X0 Y0 F2500

                ;writes a marker on the surface to help find inputguides.
                SUBROUTINE :SLINE_MARK

                ;make sure at central position
                G1 X0 Y0 F2500

                ;increase speed variable/filter constant
                ;Speed = Speed * ParamSpeedIncreaseFactor
                ;FilterConstant = FilterConstant * 4

                ;Reset filter
                FL X0 Y0 Z0 U0

                G90
                ;moves typically 1.5mm ready for the next AWG
                G1 X ((SpeedGroupSpacing)) F2500
                ;make this the new home position
                G92 XYZ

            NEXT
            ;increase power variable
            ;Power = Power + ParamPowerIncreaseFactor

            ;spacing for new power group+little extra so can tell apart -CURRENTLY SET TO ZERO
            G1 X ((PowerGroupSpacing)) F2500
            G92 XYZ
NEXT
;just incase extra spacing required -CURRENTLY SET TO ZERO
;G1 X (FinalSpacing) F100

;move laser back up+sets position as home
G1 Z -(WaveguideDepth) F100
```

```
;subroutine for waveguides-this should work fine.

:WRITE_WAVEGUIDE
        SUBROUTINE :WRITE_FILE
        G90
        ; move to x0, y0
        G1 XCX0 YCY0 F3000
        SOFTWARE POSITION XY
        G1 XCX0 YCY0 F2500

        ;set the shutter for waveguides
        WINDOW 1 Y0 LOW (UtilLaserOnCoordinateY) HIGH (UtilLaserOffCoordinateY) ENABLE ABS
        FIRE WINDOW ON

        ;velocity profiling on
        SUBROUTINE :VEL_ON

        ;move section 1      - straight line, excitation
        G1 YCY1 FSpeed

        ; move section 2 - curved line to enter perpendicular in slab
        G2 XCX2 YCY2 RCR2 FSpeed

        ; move section 3 - slab 1
        G1 XCX3 YCY3 FSpeed

        ; move section 4 - straight line taper incomplete-is this step even needed for the waveguide subroutine
        G1 XCX4 YCY4 FSpeed

        ; move section 5 - straight line taper complete + extra Length
        G1 XCX5 YCY5 FSpeed

        ; section 6 curved waveguides
        G3 XCX6 YCY6 RCR6 FSpeed

        , section 7 straight elements before slab
        G1 XCX7 YCY7 FSpeed

        ; section 8 - slab to sample end
        G9 G1 Y Length      FSpeed

        ;velocity profiling off
        SUBROUTINE :VEL_OFF

        ;turn of windowing when moving backwards
        WINDOW 1 DISABLE

RETURN
```

```
;subroutine for writing the slab
:WRITE_SLAB
        SUBROUTINE :WRITE_FILE
        G90
        ; move to x0, y0
        G1 XCX0 YCY0 F3000
        SOFTWARE POSITION XY
        G1 XCX0 YCY0 F2500

        ;set the shutter for the first section
        WINDOW 1 Y0 LOW (UtilLaserOnCoordinateY) HIGH (UtilLaserOffCoordinateY) ENABLE ABS          ;Set Window
        FIRE WINDOW ON

        ;velocity profiling on
        SUBROUTINE :VEL_ON

        ;move section 1      - straight line, excitation
        G8 G1 YCY1 FSpeed

        ; move section 2 - curved line to enter perpendicular in slab
        G2 XCX2 YCY2 RCR2 FSpeed

        ; move section 3 - slab 1
        G1 XCX3 YCY3 FSpeed

        ; move section 4 - straight line taper -off controlled by utilLaserOffcoord
        ;G1 XCX42 YCY42 FSpeed

        ; move section 5 - straight line extra Length
        G1 XCX52 YCY52 FSpeed

        ;move to central position of the slab
        G9 G1 XArrayCenterX YArrayCenterY FSpeed

        ;at this point the 1st window can be disabled and the 2nd window can be enabled. Velocity profiling will need to be turne
        ;velocity profiling off
        SUBROUTINE :VEL_OFF
        ;DWELL 250
        WINDOW 1 DISABLE

        ;set window for second slab
        WINDOW 1 Y(ArrayCenterY) LOW (LaserOn2) HIGH (LaserOff2) ENABLE ABS   ;Set Window
        FIRE WINDOW ON

        ;velocity profiling on
        SUBROUTINE :VEL_ON

        ;position of full 2*geotaper
        G1 XCX62 YCY62 FSpeed
```

```
                                -

        ; section  - position that the second slabs input tapers start
        G1 X LaserOn3X Y LaserOn3 FSpeed

        ;section 7  -  start position of slab 2.
        G1 XCX7 YCY7 FSpeed

        ; section 8 - slab to sample end
        G9 G1 YLength FSpeed

        ;velocity profiling off
        SUBROUTINE :VEL_OFF

        ;turn of windowing when moving backwards
        WINDOW 1 DISABLE

RETURN
------------------------------------------------------------------
subroutine for writing outerslab
WRITE_OUTER_SLAB
        SUBROUTINE :WRITE_FILE
        G90
        ; move to x0, y0
        G1 XCX0 YCY0 F3000
        SOFTWARE POSITION XY
        G1 XCX0 YCY0 F2500

        ;set the shutter for the first section
        WINDOW 1 Y0 LOW (UtilLaserOnCoordinateY) HIGH (UtilLaserOffCoordinateY) ENABLE ABS
        FIRE WINDOW ON

        ;velocity profiling on
        SUBROUTINE :VEL_ON

        ;move section 1        - straight line, excitation
        G1 YCY1 FSpeed

        ; move section 2 - curved line to enter perpendicular in slab
        G2 XCX2 YCY2 RCR2 FSpeed

        ; move section 3 - slab 1
        G1 XCX3 YCY3 FSpeed

        ;RAMP 500
        ;move to centre of array.
        G9 G1 XouterX YouterY F Speed

        ;at this point the 1st window can be disabled and the 2nd window can be enabled. Velocity profiling will
        ;velocity profiling off
```

```
;velocity profiling on
SUBROUTINE :VEL_ON

;move section 1        - straight line, excitation
G1 YCY1 FSpeed

; move section 2 - curved line to enter perpendicular in slab
G2 XCX2 YCY2 RCR2 FSpeed

; move section 3 - slab 1
G1 XCX3 YCY3 FSpeed

;RAMP 500
;move to centre of array.
G9 G1 XouterX YouterY F Speed

;at this point the 1st window can be disabled and the 2nd window can be enabled. Velocity profiling will need to
;velocity profiling off
SUBROUTINE :VEL_OFF
;DWELL 300
WINDOW 1 DISABLE

;set window for second slab
WINDOW 1 Y(outerY) LOW (LaserOn2) HIGH (LaserOff2) ENABLE ABS              ;Set Window ... ABS doe
FIRE WINDOW ON

;velocity profiling on
SUBROUTINE :VEL_ON

;section 7  - curved start position of slab 2.
G1 XCX7 YCY7 FSpeed

; section 8 - slab to sample end
G9 G1 YLength FSpeed

;velocity profiling off
SUBROUTINE :VEL_OFF

;turn of windowing when moving backwards
WINDOW 1 DISABLE

TURN
-----------------------------------------------------------------------

broutine for parameter calculations for each AWG
ALCULATIONS_AWG
        ; half the number of lines in one slab
        UtilNumberOfLines = CVI( (GeoSlabWidth+0.000001) /(GeoLineSpacing*2)) ;half the number of lines
```

```
;resetting the counter
UtilCounter = - UtilNumberOfLines

;calculation of the number between lines —> should be 46 for 18.4 um waveguide spacing and 0.4 um line spacing
UtilWaveguideAtEveryLine = CVI((GeoWaveguideSpacing+0.000001)/GeoLineSpacing)

;position where the last taper ends, used for distinguish between slab only or waveguide/taper
UtilPositionOfOuterWaveguide = CVI(UtilWaveguideAtEveryLine*0.5*GeoNumberOfWaveguides-0.5*UtilWaveguideA

;curvature radius for input.
GeoCurvatureRadiusSlab1In = GeoCurvatureRadiusSlab1Out / 2

;calculation for the tilting of the first slab depending on rSoft Values
UtilA = GeoSlabAngle * 2
; add here a certain value, when the whole structure needs tilting needs work.
AS3 = UtilA

;calculating the angle between the lines in the slab: UtilWaveguideAtEveryLine*UtilAngleBetweenLines gives matlab Ao.
;this definition is used as helpful later.
UtilAngleBetweenLines = DEG(GeoWaveguideSpacing/GeoCurvatureRadiusSlab1Out/UtilWaveguideAtEveryLine)

;angle of 1st waveguide, simplified version of my matlab with asa included.
;(UtilWaveguideAtEveryLine*UtilAngleBetweenLines) because need an angle between waveguides not lines.
UtilA0 = -(GeoNumberOfWaveguides-1)* 0.5 * UtilWaveguideAtEveryLine*UtilAngleBetweenLines + AS3 - GeoSlabAn

;outer rowland curve + taper length
UtilRend = GeoCurvatureRadiusSlab1Out+TaperExtra

;length from start to half way point of AWG (eg the centre of the array.)
Utillg = Lextra + UtilRend*COS(RAD(UtilA0))+GeoRz*SIN(RAD(UtilA0))


;Input line is sample length minus AWG length - curved section at beginning.
CorrectionLength = SampleLength-(2*EdgeBoarder)-(2* Utillg*COS(RAD(GeoSlabAngle)))-GeoRadius2*(SIN(RAD(AS3)
IF (CorrectionLength < 0) THEN
        MESSAGE DISPLAY "Sample to short"
        EXIT                                    ;End of program
ENDIF

;length of the inputline
GeoLengthInputLine = EdgeBoarder + CorrectionLength + LeadInOut

;position of central input into slab 1.
CX20 = GeoRadius2*(1-COS(RAD(AS3)))
CY20 = GeoLengthInputLine + GeoRadius2*(SIN(RAD(AS3)))

;variables required in the calculation of zli and zri values
UtilC = 0.5*GeoDL*GeoCurvatureRadiusSlab1Out/GeoWaveguideSpacing
UtilB = (Utillg-GeoRz*(SIN(RAD(UtilA0))-RAD(UtilA0)*COS(RAD(UtilA0))))/COS(RAD(UtilA0))-(UtilRend+UtilC*
```

```
;half way position to centre of 2nd fpz
Bx =CX20 + Utillg*SIN(RAD(GeoSlabAngle))
By = CY20 + Utillg*COS(RAD(GeoSlabAngle))
;gradient of lg
grad2 = ((By - CY20)/(Bx-CX20))
grad3 = -(1/grad2)


;centre of the 2nd fpz ro circle.
UtilXro = CX20 + 2* Utillg*SIN(RAD(GeoSlabAngle))
UtilYro = CY20 + 2* Utillg*COS(RAD(GeoSlabAngle))

;centre of the 2nd fpz ri circle
UtilXri = UtilXro
UtilYri = UtilYro - GeoCurvatureRadiusSlab1In


RETURN

;-------------------------------------------------------------------
;calculates the coord's of each waveguide writen
:CALCULATIONS_LINE
;calculating the modulo
;if on a waveguide = 0 if not it returns value of how many waveguides are required till the waveguide.
;make sure the CVI is going the correct way, could use this value to shorten moduloshift.
UtilModulo = (UtilCounter/UtilWaveguideAtEveryLine - CVI(UtilCounter/UtilWaveguideAtEveryLine))*UtilWavegu

;calculating the shifted modulo to produce the taper
;function is minimum, when counter is between two waveguides and is 1 when counter is at the waveguide, (absolute pro
;adding GeoNumberLines*UtilWaveguideAtEveryLine makes sure that the final value is positive, CVI function is symme
;long code but should work
UtilModuloShift = 1-ABS(((UtilCounter+(UtilWaveguideAtEveryLine/2)+UtilNumberOfLines*UtilWaveguideAtEvery
;use this one to generate the taper length
;ModuloShift = ModuloShift * GeoTaperLength

;new taper positioning test
AngleCorrection = CVI(UtilCounter/UtilWaveguideAtEveryLine)*UtilWaveguideAtEveryLine
ZAaj4 = AngleCorrection*UtilAngleBetweenLines + AS3
ZAaj5 = ZAaj4 - AS3

;calculation for curved waveguide section
;calculates angle from the y axis
ZAaj = UtilCounter * UtilAngleBetweenLines + AS3
;calculates angle from the awg axis
ZAaj2 = ZAaj - GeoSlabAngle
;calculates angle from the central axis of the fpz.
ZAaj3 = ZAaj - AS3
```

```
        ;calculates the radius needed for the array guides
        CR6 = (Utillg/COS(RAD(ZAaj2))-(UtilRend+UtilC*RAD(ZAaj2)+UtilB))/(TAN(RAD(ZAaj2))-RAD(ZAaj2

        ;extra length: glen's "zlj"
        UtilExtraLength = (UtilC-CR6)*RAD(ZAaj2)+UtilB

        ;distance from start to end point of a waveguide in the array
        Utilh = 2*CR6*SIN(RAD(ZAaj2))

        ;setting starting coordinates for the movement
        CX0 = UtilCounter*GeoLineSpacing
        CY0 = 0

        ;straight line at the beginning
        CY1 = GeoLengthInputLine

;curve at excitation , gets to a flat line instead of curve before 1st fpz
        CR2 = GeoRadius2 - UtilCounter*GeoLineSpacing
        CX2 = CX0 + CR2*(1-COS(RAD(AS3)))
        CY2 = CY1 + CR2*(SIN(RAD(AS3)))

        ;entry curvature is calculated later as a laser on coord.

;slab1 - curvature this is the position where the slab ends.-make window position if no tapers
        CX3 = CX20 + SIN(RAD(ZAaj))*(GeoCurvatureRadiusSlab1Out)
        CY3 = CY20 + COS(RAD(ZAaj))*(GeoCurvatureRadiusSlab1Out)

;straight lines, section 4, movement for incomplete taper length, close shutter after here
;this is the kink after the 1st slab ends.
        CX4 = CX20 + SIN(RAD(ZAaj))*(GeoCurvatureRadiusSlab1Out+UtilModuloShift*GeoTaperLength)
        CY4 = CY20 + COS(RAD(ZAaj))*(GeoCurvatureRadiusSlab1Out+UtilModuloShift*GeoTaperLength)

;taper angle corrected taper off. -working
        CX42 = CX3 + SIN(RAD(ZAaj4))*(UtilModuloShift*GeoTaperLength)
        CY42 = CY3 + COS(RAD(ZAaj4))*(UtilModuloShift*GeoTaperLength)

;straight line for taper + extraLength.
;extra length can be a negative this is why the taper length is actually only half quoted value to allow this.
        CX5 = CX20 + SIN(RAD(ZAaj))*(UtilRend+UtilExtraLength)
        CY5 = CY20 + COS(RAD(ZAaj))*(UtilRend+UtilExtraLength)

;taper angle corrected taper end test.-test without utilExtralength-working
        CX52 = CX3 + SIN(RAD(ZAaj4))*(2*GeoTaperLength)
        CY52 = CY3 + COS(RAD(ZAaj4))*(2*GeoTaperLength)

;curved guides, radius calculated already before-posiable change to a reverse arument??-maybe.
        CX6 = CX5 + Utilh*SIN(RAD(GeoSlabAngle))
        CY6 = CY5 + Utilh*COS(RAD(GeoSlabAngle))
```

```
        ; calculation of a point perpendicular to the 2nd slab input for gradient calculation. NOT WORKING
        CX62 = CX7 +((2*GeoTaperLength)*SIN(RAD(ZAaj5)))
        CY62 = CY7 - ((2*GeoTaperLength)*COS(RAD(ZAaj5)))

        ;end point of slab 2 is determined by a window off coordinate

;moves to end of chip.-never used yet
        ;CY9 = Length


;shutter , using just the y will cause issues for initial slabs with higher angles especially 90,code will need improvments
;determines position of the start of the slab, opens window for laser.
        UtilLeadInProfile1 = GeoCurvatureRadiusSlab1In-SQR(GeoCurvatureRadiusSlab1In*GeoCurvatureRadiusSlab1In-(UtilCo
        UtilLaserOnCoordinateY = CY2 + (COS(RAD(AS3))*UtilLeadInProfile1)
        UtilLaserOnCoordinateX = CX2 + (SIN(RAD(AS3))*UtilLeadInProfile1)

;runs laser till 500um past end of chip so no slow down in velcity within chip.
        UtilLaserOffCoordinateY = Length

;postion a second window starts for the tapers before the second slab in y coord
        LaserOn2 = UtilYro - ((GeoCurvatureRadiusSlab1Out + UtilModuloShift*GeoTaperLength)*COS(RAD(ZAaj3)))
        LaserOn2X = UtilXro + ((GeoCurvatureRadiusSlab1Out + UtilModuloShift*GeoTaperLength)*SIN(RAD(ZAaj3)))

        ;position corrected taper angle starts at-working
        LaserOn3X = CX7 + ((UtilModuloShift*GeoTaperLength)*SIN(RAD(ZAaj5)))
        LaserOn3 = CY7 - ((UtilModuloShift*GeoTaperLength)*COS(RAD(ZAaj5)))


;position a second window stops creating the curve for the output edge of the awg.
        LaserOff2 = UtilYri + SQR(UtilYri*UtilYri - ((UtilYri*UtilYri) + (CX7*CX7) - 2*UtilXri*CX7 + (UtilXri*UtilXri) - (

        ;gradient of slabs in 1st line
        grad1 = (CY3-CY2)/(CX3-CX2)
        ;outerslab coords
        outerX = ((-grad3*Bx+By+grad1*CX2-CY2)/(grad1-grad3))
        outerY = grad3*(outerX - Bx)+By

        ;central position in the array -NOT WORKING-issue possiably when grad is straight up and down on second slab --use sam
        grad4 = ((CY52-CY3)/(CX52-CX3))

        ;grad5 = ((CY7 - CY62)/(CX7 - CX62)) ;replace with grad3                    ;THIS IDEA DOESNT WORK
        ;ArrayCenterX = ((-grad5*CX62+CY62+grad4*CX52-CY52)/(grad4-grad5))
        ;ArrayCenterY = (grad4*(ArrayCenterX - CX52)) + CY52

        ArrayCenterX = ((-grad3*Bx+By+grad4*CX52-CY52)/(grad4-grad3))              ;NOW TRYING THIS
        ArrayCenterY = (grad4*(ArrayCenterX - CX52)) + CY52
RETURN

;-------------------------------------------------------------------
```

References

[1] J. Bland-hawthorn and P. Kern. *Astrophotonics : a new era for astronomical instruments.* Optics Express **17**(3), 2545 (2009).

[2] C. Lovis, F. Pepe, F. Bouchy, G. Lo, M. Mayor, O. D. Haute-provence, and S. Michel. *The exoplanet hunter HARPS : unequalled accuracy and perspectives toward 1 cm s -1 precision.* In *SPIE Proceedings*, pp. 1–9 (2006).

[3] H. Ishio, J. Minowa, and K. Nosu. *Review and status of wavelength-division-multiplexing technology and its application.* Journal of Lightwave Technology **2**(4), 3 (1984).

[4] M. Smit. *New focussing and dispersive planar component based on an optical phased array.* Electronics Letters **24**(7), 17 (1988).

[5] A. R. Vellekoop and M. K. Smit. *A small-size polarization splitter based on a planar optical phased array.* Journal of Lightwave Technology **8**(1), 118 (1990).

[6] A. R. Vellekoop and M. K. Smit. *Four-C hannel Integrated-Optic Wavelength Demultiplexer With Weak Polarization Dependence.* Journal of Lightwave Technology **9**(3), 310 (1991).

[7] M. K. Smit. *Integrated Optics in silicon-based aluminum oxide.* Ph.D. thesis, Delft Univ. of Technol. (1991).

[8] C. Dragone. *An N x N Optical Multiplexer Using a Planar Arrangement of Two Star Couplers.* Photonics technology letters **3**(9), 812 (1991).

[9] C. Dragone, C. A. Edwards, and R. C. Kistler. *Integrated Optics NxN Multiplexer on Silicon.* Photonics technology letters **3**(10), 896 (1991).

[10] B. J. Luff, D. Feng, D. C. Lee, W. Qian, H. Liang, and M. Asghari. *Hybrid Silicon Photonics for Low-Cost High-Bandwidth Link Applications.* Advances in Optical Technologies **2008**, 1 (2008).

[11] F. G. Watson. *A Multi-Fiber Waveguide Spectrograph for Astronomy ?* SPIE Proceedings **2476**(68), 68 (1995).

[12] F. Watson. *Waveguide Spectrographs for Astronomy ?* SPIE Proceedings **2871**, 1373 (1996).

[13] J. Bland-Hawthorn and A. Horton. *Instruments without optics: an integrated photonic spectrograph.* SPIE Proceedings **6269**, 62690N (2006).

[14] N. Cvetojevic, N. Jovanovic, C. Betters, J. S. Lawrence, S. C. Ellis, G. Robertson, and J. Bland-Hawthorn. *First starlight spectrum captured using an integrated photonic micro-spectrograph.* Astronomy & Astrophysics **544**, L1 (2012).

[15] N. Cvetojevic, N. Jovanovic, J. Lawrence, M. Withford, and J. Bland-Hawthorn. *Developing arrayed waveguide grating spectrographs for multi-object astronomical spectroscopy.* Optics Express **20**(3), 2062 (2012).

[16] I. Spaleniak, N. Jovanovic, S. Gross, M. J. Ireland, J. S. Lawrence, and M. J. Withford. *Integrated photonic building blocks for next-generation astronomical instrumentation II: the multimode to single mode transition.* Optics Express **21**(22), 27197 (2013).

[17] N. Jovanovic, P. G. Tuthill, B. Norris, S. Gross, P. Stewart, N. Charles, S. Lacour, M. Ams, J. S. Lawrence, A. Lehmann, C. Niel, J. G. Robertson, G. D. Marshall, M. Ireland, A. Fuerbach, and M. J. Withford. *Starlight demonstration of the Dragonfly instrument : an integrated photonic pupil-remapping interferometer for high-contrast imaging.* Mon. Not. R. Astron. Soc. **427**, 806 (2012).

[18] I. Spaleniak, S. Gross, N. Jovanovic, R. J. Williams, J. S. Lawrence, M. J. Ireland, and M. J. Withford. *Multiband processing of multimode light: Combining 3D photonic lanterns with waveguide Bragg gratings.* Laser and Photonics Reviews **8**(1), 1 (2014).

[19] K. M. Davis, K. Miura, N. Sugimoto, and K. Hirao. *Writing waveguides in glass with a femtosecond laser.* OPTICS LETTERS **21**(21), 1729 (1996).

[20] E. N. Glezer, M. Milosavljevic, L. Huang, R. J. Finlay, T. H. Her, J. P. Callan, and E. Mazur. *Three-dimensional optical storage inside transparent materials: errata.* Optics Letters **21**(24), 2023 (1996).

[21] G. D. Marshall, A. Politi, J. C. F. Matthews, P. Dekker, M. Ams, M. J. Withford, and J. L. O'Brien. *Laser written waveguide photonic quantum circuits.* Optics Express **17**(15), 12546 (2009).

[22] C. B. Schaffer, A. Brodeur, and E. Mazur. *Laser-induced breakdown and damage in bulk transparent materials induced by tightly focused femtosecond laser pulses.* Measurement Science and Technology **12**(11), 1784 (2001).

[23] L. V. Keldysh. *Ionization in the field of a strong electromagnetic wave.* JETP, Soviet Physics **20**(5), 1307 (1965).

[24] A. Kaiser, B. Rethfeld, M. Vicanek, and G. Simon. *Microscopic processes in dielectrics under irradiation by subpicosecond laser pulses.* Physical Review B **61**(17), 11437 (2000).

[25] F. Quéré, S. Guizard, and P. Martin. *Time-resolved study of laser-induced breakdown in dielectrics.* Europhysics Letters (EPL) **56**(1), 138 (2007).

[26] M. Lenzner, J. Krüger, S. Sartania, Z. Cheng, C. Spielmann, G. Mourou, W. Kautek, and F. Krausz. *Femtosecond Optical Breakdown in Dielectrics.* Physical Review Letters **80**(18), 4076 (1998).

[27] C. Schaffer, J. García, and E. Mazur. *Bulk heating of transparent materials using a high-repetition-rate femtosecond laser.* Applied Physics A: Materials Science & Processing **76**(3), 351 (2003).

[28] J. W. Chan, T. Huser, S. Risbud, and D. M. Krol. *Structural changes in fused silica after exposure to focused femtosecond laser pulses.* Optics Letters **26**(21), 1726 (2001).

[29] W. Reichman, J. W. Chan, and D. M. Krol. *Confocal fluorescence and Raman microscopy of femtosecond laser-modified fused silica.* Journal of Physics: Condensed Matter **15**, 2447 (2003).

[30] a. Saliminia, R. Vallée, and S. Chin. *Waveguide writing in silica glass with femtosecond pulses from an optical parametric amplifier at 1.5μm.* Optics Communications **256**(4-6), 422 (2005).

[31] M. Will, S. Nolte, B. N. Chichkov, and A. Tünnermann. *Optical properties of waveguides fabricated in fused silica by femtosecond laser pulses.* Applied Optics **41**(21), 4360 (2002).

[32] P. Dekker, M. Ams, and G. Marshall. *Annealing dynamics of waveguide Bragg gratings: evidence of femtosecond laser induced colour centres.* Optics Express **18**(4), 1247 (2010).

[33] C. Hnatovsky, R. Taylor, E. Simova, P. Rajeev, D. Rayner, V. Bhardwaj, and P. Corkum. *Fabrication of microchannels in glass using focused femtosecond laser radiation and selective chemical etching.* Applied Physics A **84**(1-2), 47 (2006).

[34] Y. Shimotsuma, P. Kazansky, J. Qiu, and K. Hirao. *Self-Organized Nanogratings in Glass Irradiated by Ultrashort Light Pulses.* Physical Review Letters **91**(24), 247405 (2003).

[35] L. Sudrie, M. Franco, B. Prade, and A. Mysyrowicz. *Writing of permanent birefringent microlayers in bulk fused silica with femtosecond laser pulses.pdf.* Optical Engineering **177**(1999), 279 (1999).

[36] J. Qiu, K. Miura, and K. Hirao. *Femtosecond laser-induced microfeatures in glasses and their applications.* Journal of Non-Crystalline Solids **354**(12-13), 1100 (2008).

[37] W. Cai, A. R. Libertun, and R. Piestun. *Polarization selective computer-generated holograms realized in glass by femtosecond laser induced nanogratings.* Optics Express **14**(9), 3785 (2006).

[38] G. Cheng, K. Mishchik, C. Mauclair, E. Audouard, and R. Stoian. *Ultrafast laser photoinscription of polarization sensitive devices in bulk silica glass.* Optics Express **17**(12), 9515 (2009).

[39] S. Richter, M. Heinrich, S. Döring, a. Tünnermann, and S. Nolte. *Formation of femtosecond laser-induced nanogratings at high repetition rates.* Applied Physics A **104**(2), 503 (2011).

[40] H. B. Sun, Y. Xu, S. Juodkazis, K. Sun, M. Watanabe, S. Matsuo, H. Misawa, and J. Nishii. *Arbitrary-lattice photonic crystals created by multiphoton microfabrication.* Optics Letters **26**(6), 325 (2001).

[41] N. Jovanovic, J. Thomas, R. J. Williams, M. J. Steel, G. D. Marshall, A. Fuerbach, S. Nolte, A. Tünnermann, and M. J. Withford. *Polarization-dependent effects in point-by-point fiber Bragg gratings enable simple, linearly polarized fiber lasers.* Optics Express **17**(8), 6082 (2009).

[42] C. Miese, M. J. Withford, and A. Fuerbach. *Femtosecond laser direct-writing of waveguide Bragg gratings in a quasi cumulative heating regime.* Optics Express **19**(20), 19542 (2011).

[43] S. Gross. *Direct Write Mid-IR Waveguide Lasers.* Ph.D. thesis (2012).

[44] M. Ams, G. D. Marshall, and M. J. Withford. *Study of the influence of femtosecond laser polarisation on direct writing of waveguides.* Optics Express **14**(26), 13158 (2006).

[45] M. Ams, G. Marshall, D. Spence, and M. Withford. *Slit beam shaping method for femtosecond laser direct-write fabrication of symmetric waveguides in bulk glasses.* Optics Express **13**(15), 5676 (2005).

[46] d. l. C. A. Ruiz, A. Ferrer, W. Gawelda, D. Puerto, M. G. Sosa, J. Siegel, and J. Solis. *Independent control of beam astigmatism and ellipticity using a SLM for fs-laser waveguide writing.* Optics Express **17**(23), 20853 (2009).

[47] A. . A. Said, M. Dugan, P. Bado, Y. Bellouard, A. Scott, and J. R. Mabesa, Jr. *Manufacturing by laser direct-write of three-dimensional devices containing optical and microfluidic networks* **5339**, 194 (2004).

[48] R. Osellame, M. Lobino, N. Chiodo, M. Marangoni, G. Cerullo, R. Ramponi, H. T. Bookey, R. R. Thomson, N. D. Psaila, and A. K. Kar. *Femtosecond laser writing of waveguides in periodically poled lithium niobate preserving the nonlinear coefficient.* Applied Physics Letters **90**(24), 241107 (2007).

[49] S. M. Eaton, H. Zhang, M. L. Ng, J. Li, W.-J. Chen, S. Ho, and P. R. Herman. *Transition from thermal diffusion to heat accumulation in high repetition rate femtosecond laser writing of buried optical waveguides.* Optics Express **16**(13), 9443 (2008).

[50] S. Eaton, H. Zhang, P. Herman, F. Yoshino, L. Shah, J. Bovatsek, and A. Arai. *Heat accumulation effects in femtosecond laser-written waveguides with variable repetition rate.* Optics Express **13**(12), 4708 (2005).

[51] R. R. Gattass, L. R. Cerami, and E. Mazur. *Micromachining of bulk glass with bursts of femtosecond laser pulses at variable repetition rates.* Optics Express **14**(12), 5279 (2006).

[52] M. Ams. *Fabrication Of Optical Waveguide Devices In Bulk Materials Using Femtosecond Laser Pulses.* Ph.D. thesis (2008).

[53] K. Kajihara, L. Skuja, M. Hirano, and H. Hosono. *Formation and decay of nonbridging oxygen hole centers in SiO2 glasses induced by F2 laser irradiation: In situ observation using a pump and probe technique.* Applied Physics Letters **79**(12), 1757 (2001).

[54] L. Skuja, S. State, T. Suzuki, and K. Tanimura. *Site-selective laser-spectroscopy studies of the intrinsic 1.9-eV luminescence center in glassy SiO2.* Physical Review B **52**(21), 15208 (1995).

[55] K. Kajihara, L. Skuja, M. Hirano, and H. Hosono. *In situ observation of the formation, diffusion, and reactions of hydrogenous species in F2-laser-irradiated SiO2 glass using a pump-and-probe technique.* Physical Review B **74**(9), 094202 (2006).

[56] F. Dreisow, A. Szameit, T. Pertsch, S. Nolte, and A. Tuennermann. *Visualization of light propagation in fs laser written waveguide arrays.* SPIE Proceedings **6460**(0), 64601C (2007).

[57] Heraeus. *SUPRASIL 311 and 312 Standard Optics Information.* Tech. rep.

[58] Corning. *Corning Eagle AMLCD Glass Substrates.* Tech. Rep. April (2005).

[59] S. Gross, N. Riesen, J. D. Love, and M. J. Withford. *Three-dimensional ultra-broadband integrated tapered mode multiplexers.* Laser & Photonics Reviews **8**(5), L81 (2014).

[60] T. Meany, S. Gross, N. Jovanovic, A. Arriola, M. J. Steel, and M. J. Withford. *Towards low-loss lightwave circuits for non-classical optics at 800 and 1,550 nm.* Applied Physics A **114**(1), 113 (2013).

[61] N. Jovanovic, P. G. Tuthill, B. Norris, S. Gross, P. Stewart, N. Charles, S. Lacour, J. Lawrence, G. Robertson, A. Fuerbach, and M. J. Withford. *Progress and challenges with the Dragonfly instrument; an integratedphotonic pupil-remapping interferometer* **8445**, 844505 (2012).

[62] W. Watanabe, Y. Note, and K. Itoh. *Fabrication of multimode interference waveguides in glass by use of a femtosecond laser.* Optics Letters **30**(21), 2888 (2005).

[63] S. Ghosh, N. D. Psaila, R. R. Thomson, B. P. Pal, R. K. Varshney, and A. K. Kar. *Ultrafast laser inscribed waveguide lattice in glass for direct observation of transverse localization of light.* Applied Physics Letters **100**(10), 101102 (2012).

[64] A. P. G. Russell, T. G. Hawarden, E. Atad, S. K. Ramsay-Howat, A. Quirrenbach, R. Bacon, and R. M. Redfern. *Instrumentation studies for a european extremely large telescope: a strawman instrument suite and implications for telescope design.* In A. L. Ardeberg and T. Andersen, eds., *SPIE Proceedings*, vol. 5382, pp. 684–698 (2004).

[65] R. Haynes, J. Bland-Hawthorn, M. C. Large, K.-F. Klein, and G. W. Nelson. *New age fibers the children of the photonic revolution.* In E. Atad-Ettedgui and P. Dierickx, eds., *Optical Fabrication Metrology and material Advancment for telescopes*, pp. 586–597 (2004).

[66] J. Bland-Hawthorn, M. Englund, and G. Edvell. *New approach to atmospheric OH suppression using an aperiodic fibre Bragg grating.* Optics Express **12**(24), 5902 (2004).

[67] R. R. Thomson, A. K. Kar, and J. Allington-Smith. *Ultrafast laser inscription: an enabling technology for astrophotonics.* Optics Express **17**(3), 1963 (2009).

[68] C. Q. Trinh, S. C. Ellis, J. Bland-Hawthorn, J. S. Lawrence, A. J. Horton, S. G. Leon-Saval, K. Shortridge, J. Bryant, S. Case, M. Colless, W. Couch, K. Freeman, H.-G. Löhmannsröben, L. Gers, K. Glazebrook, R. Haynes, S. Lee, J. OByrne, S. Miziarski, M. M. Roth, B. Schmidt, C. G. Tinney, and J. Zheng. *Gnosis: the First Instrument To Use Fiber Bragg Gratings for OH Suppression.* The Astronomical Journal **145**(2), 51 (2013).

[69] B. I. Akca, V. D. Nguyen, J. Kalkman, N. Ismail, G. Sengo, F. Sun, A. Driessen, T. G. van Leeuwen, M. Pollnau, K. Wörhoff, and R. M. de Ridder. *Toward Spectral-Domain Optical Coherence Tomography on a Chip.* IEEE Journal of Selected Topics in Quantum Electronics **18**(3), 1223 (2012).

[70] N. Ismail, L.-P. Choo-Smith, K. Wörhoff, A. Driessen, A. C. Baclig, P. J. Caspers, G. J. Puppels, R. M. de Ridder, and M. Pollnau. *Raman spectroscopy with an integrated arrayed-waveguide grating.* Optics Letters **36**(23), 4629 (2011).

[71] Y. Komai, H. Nagano, K. Kodate, K. Okamoto, and T. Kamiya. *Application of Arrayed-Waveguide Grating to Compact Spectroscopic Sensors.* Japanese Journal of Applied Physics **43**(8B), 5795 (2004).

[72] Y. Hida, T. Shibata, Y. Inoue, H. Takahashi, and K. Okamoto. *Silica-based Arrayed-waveguide Gratings for the Visible Wavelength Range.* NTT Technical Review **4**(6), 48 (2006).

[73] K. Kodate and Y. Komai. *Compact spectroscopic sensor using an arrayed waveguide grating.* Journal of Optics A: Pure and Applied Optics **10**(4), 044011 (2008).

[74] T. Saida, T. Shibata, M. Ishii, and H. Takahashi. *Integrated optical tweezers using arrayed waveguide grating.* (CLEO). Conference on Lasers and Electro-Optics, 2005. (2), 556 (2005).

[75] K. Okamoto and A. Sugita. *Flat spectral response arrayed-waveguide grating multiplexer with parabolic waveguide horns.* Electronics Letters **32**(18), 1661 (1996).

[76] M. R. Amersfoort, J. Soole, H. LeBlanc, N. Andreadakis, A. Rajhel, and C. Caneau. *Passband broadening of integrated arrayed waveguide filters using multimode interference couplers.* Electronics Letters **32**(5), 449 (1996).

[77] K. Okamoto and H. Yamada. *Arrayed-waveguide grating multiplexer with flat spectral response.* Optics Letters **20**(1), 43 (1995).

[78] D. Trouchet, A. Beguin, H. Boek, C. Prel, C. Lerminiaux, and R. Maschmeyer. *Passband flattening of PHASAR WDM using input and output star couplers designed with two focal points.* In *OFC '97 TuN1, SAN Jose, CA*, pp. 302–303 (1998).

[79] Synopsys. *RSoft CAD Environment 8.1 User Guide* (2008).

[80] K. Okamoto. *Fundamentals of optical waveguides* (Academic press, 2010).

[81] C. V. Dam, A. A. M. Staring, E. J. Jansen, J. J. M. Binsma, T. V. Dongen, M. K. Smit, and B. H. Verbeek. *Loss reduction for phased-array demultiplexers using a double etch technique.* In *OSA/IPR*, pp. 52–56 (1996).

[82] A. Sugita, A. Kaneko, K. Okamoto, M. Itoh, and A. Himeno. *Very Low Insertion Loss Arrayed-Waveguide Grating with Vertically Tapered Waveguides.* Photonics technology letters **12**(9), 1180 (2000).

[83] P. L. Yuan and G. Duluth. *Optical device having low insertion loss* (1998).

[84] B. Luyssaert, S. Member, P. Bienstman, P. Vandersteegen, and P. Dumon. *Efficient Nonadiabatic Planar Waveguide Tapers.* Journal of Lightwave Technology **23**(8), 2462 (2005).

[85] H. Takahashi, K. Oda, H. Toba, and Y. Inoue. *Transmission characteristics of arrayed waveguide N times N wavelength multiplexer.* Journal of Lightwave Technology **13**(3), 447 (1995).

[86] M. K. Smit, A. Member, and C. V. Dam. *PHASAR-Based WDM-Devices : Principles, Design and Applications.* Selected topics in Quantum Electronics **2**(2), 236 (1996).

[87] N. Cvetojevic, J. S. Lawrence, S. C. Ellis, J. Bland-Hawthorn, R. Haynes, and A. Horton. *Characterization and on-sky demonstration of an integrated photonic spectrograph for astronomy.* Optics Express **17**(21), 18643 (2009).

[88] D. Wang, G. Jin, Y. Yan, and M. Wu. *Aberration theory of arrayed waveguide grating.* Journal of Lightwave Technology **19**(2), 279 (2001).

[89] S. Lu, C. Yang, Y. Yan, G. Jin, Z. Zhou, W. H. Wong, and E. Y. B. Pun. *Design and fabrication of a polymeric flat focal field arrayed waveguide grating.* Optics Express **13**(25), 9982 (2005).

[90] B. I. Akca, G. Sengo, M. Pollnau, A. Driessen, K. Wörhoff, and R. M. de Ridder. *Flat-focal-field integrated spectrometer using a field-flattening lens.* Optics Letters **37**(20), 4281 (2012).

[91] N. Cvetojevic. *Development & Implementation of the Integrated Photonic Spectrograph for Astronomy.* Ph.D. thesis (2014).

[92] T. Takada, Y. Inoue, H. Yamada, and M. Horiguchi. *Measurement of phase error distributions in silica-based arrayed-waveguide grating multiplexers by using Fourier transform spectroscopy.* Electronics Letters **30**(20), 1671 (1994).

[93] R. Zektzer, D. Sinefeld, N. Goldshtein, and D. Marom. *Interferometric Method for Phase Error Measurement in an Arrayed Waveguide Grating with a Free Space Output.* National Fiber Optic Engineers Conference p. JTh2A.1 (2012).

[94] J. Gehler and F. Knappe. *Crosstalk Reduction of Arrayed Waveguide Gratings by UV trimming of individual waveguides without H2-Loading Crosstalk Reduction of Arrayed Waveguide Gratings by UV trimming of individual waveguides without H2-Loading.* In *OSA/OFC*, pp. 1–4 (2000).

[95] W. N. Ye. *STRESS ENGINEERING FOR POLARIZATION CONTROL IN SILICON-ON-INSULATOR WAVEGUIDES AND ITS APPLICATIONS IN NOVEL PASSIVE POLARIZATION.* Ph.D. thesis, Carleton, Ottawa , Canada (2006).

[96] Y. Inoue, Y. Ohmori, M. Kawachi, S. Ando, T. Sawada, and H. Takahashi. *Polarization Mode Converter With Polyimide half waveplate in silica based planer lightwave circuits.* Photonics Technology Letters **6**(5), 626 (1994).

[97] X. Xia, J. Zou, and T. Lang. *Experimental Demonstration of Birefringence Compensation Using Angled Star Couplers in Silica-Based Arrayed Waveguide Grating.* IEEE Photonics Journal **4**(6), 2236 (2012).

[98] S. H. Cho, B. E. Bouma, E. P. Ippen, and J. G. Fujimoto. *Low repetition rate high peak power Kerr lens mode locked Ti : Al2 O3 laser with a multiple-pass cavity.* Optics Letters **24**(6), 417 (1999).

[99] A. Fernandez, T. Fuji, A. Poppe, A. Fürbach, F. Krausz, and A. Apolonski. *Chirped-pulse oscillators: a route to high-power femtosecond pulses without external amplification.* Optics Letters **29**(12), 1366 (2004).

[100] S. H. Cho, F. X. Kärtner, U. Morgner, E. P. Ippen, J. G. Fujimoto, J. E. Cunningham, and W. H. Knox. *Generation of 90-nJ pulses with a 4-MHz repetition-rate Kerr-lens mode-locked Ti:Al2O3 laser operating with net positive and negative intracavity dispersion.* Optics Letters **26**(8), 560 (2001).

[101] V. Kalashnikov, E. Podivilov, A. Chernykh, and A. Apolonski. *Chirped-pulse oscillators: theory and experiment.* Applied Physics B **83**(4), 503 (2006).

[102] S. Naumov, A. Fernandez, R. Graf, P. Dombi, F. Krausz, and A. Apolonski. *Approaching the microjoule frontier with femtosecond laser oscillators.* New Journal of Physics **7**, 216 (2005).

[103] D. Herriott, H. Kogelnik, and R. Kompfner. *Off-Axis Paths in Spherical Mirror Interferometers.* Applied Optics **3**(4), 523 (1964).

[104] J. D. Kafka and T. Baer. *Prism-pair dispersive delay lines in optical pulse compression.* Optics Letters **12**(6), 401 (1987).

[105] A. Arriola, S. Gross, N. Jovanovic, N. Charles, P. G. Tuthill, S. M. Olaizola, A. Fuerbach, and M. J. Withford. *Low bend loss waveguides enable compact, efficient 3D photonic chips.* Optics Express **21**(3), 2978 (2013).

[106] S. Kanehira, K. Miura, and K. Hirao. *Ion exchange in glass using femtosecond laser irradiation.* Applied Physics Letters **93**(2), 023112 (2008).

[107] M. Sakakura, T. Kurita, M. Shimizu, K. Yoshimura, Y. Shimotsuma, N. Fukuda, K. Hirao, and K. Miura. *Shape control of elemental distributions inside a glass by simultaneous femtosecond laser irradiation at multiple spots.* Optics Letters **38**(23), 4939 (2013).

[108] M. Shimizu, M. Sakakura, M. Ohnishi, M. Yamaji, Y. Shimotsuma, K. Hirao, and K. Miura. *Three-dimensional temperature distribution and modification mechanism in glass during ultrafast laser irradiation at high repetition rates.* Optics Express **20**(2), 934 (2012).

[109] M. Abramowitz and M. W. Davidson. *Olympus Microscopy Resource Center — Differential Interference Contrast - Introduction* (2012). URL `http://www.olympusmicro.com/primer/techniques/dic/dicoverview.html`.

[110] D. B. Murphy, J. Hinsch, E. D. Salmon, K. R. Spring, C. Brandmaier, M. Brenner, S. Schwartz, H. E. Keller, M. Abramowitz, M. Pluta, M. Parry-Hill, R. T. Sutter, T. J. Fellers, and M. W. Davidson. *Molecular Expressions Microscopy Primer: Specialized Microscopy Techniques - Differential Interference Contrast* (2003). URL `http://micro.magnet.fsu.edu/primer/techniques/dic/dichome.html`.

[111] I. Mansour and F. Caccavale. *An Improved Procedure to Calculate the Refractive Index Profile from the Measured Near-Field Intensity.* Journal of Lightwave Technology **14**(3), 423 (1996).

[112] D. Blömer, A. Szameit, F. Dreisow, T. Schreiber, S. Nolte, and A. Tünnermann. *Nonlinear refractive index of fs-laser-written waveguides in fused silica.* Optics Express **14**(6), 2151 (2006).

[113] L. Tong, R. R. Gattass, I. Maxwell, J. B. Ashcom, and E. Mazur. *Optical loss measurements in femtosecond laser written waveguides in glass.* Optics Communications **259**(2), 626 (2006).

[114] P. G. Kazansky, W. Yang, E. Bricchi, J. Bovatsek, A. Arai, Y. Shimotsuma, K. Miura, and K. Hirao. *Quill writing with ultrashort light pulses in transparent materials.* Applied Physics Letters **90**(15), 151120 (2007).

[115] Y. Chung and N. Dagli. *An Assessment of Finite Difference Beam Propagation Method.* Journal of Quantum Electronics **26**(2), 1335 (1990).

[116] G. R. Hadley. *Transparent Boundary Condition for the Beam Propagation Method.* Journal of Quantum Electronics **28**(1), 363 (1992).

[117] W. P. Huang and C. L. Xu. *Simulation of Three-Dimensional Optical Waveguides by a Full-Vector Beam Propagation Method.* Journal of Quantum Electronics **29**(October), 2639 (1993).

[118] I. Ilic, R. Scarmozzino, R. M. O. Jr, J. T. Yardley, K. W. Beeson, and M. J. Mcfarland. *Modeling Multimode-Input Star Couplers in Polymers.* Journal of Lightwave Technology **12**(6), 996 (1994).

[119] R. Scarmozzino, A. Gopinath, R. Pregla, and S. Helfert. *Numerical Techniques for Modeling Guided-Wave Photonic Devices.* Journal of Selected Topics in Quantum Electronics **6**(1), 150 (2000).

[120] J. V. Roey, J. V. D. Donk, and P. E. Lagasse. *Beam-propagation method : analysis and assessment.* J. Opt. Soc. Am. **71**(7), 803 (1981).

[121] P. Kaczmarski and P. E. Lagasse. *Bidirectional beam propagation method.* Electronics Letters **24**, 675 (1988).

[122] G. R. Hadley. *Wide-angle beam propagation using Pade approximant operators.* Optics Letters **17**(20), 1426 (1992).

[123] a. Barty, K. a. Nugent, D. Paganin, and A. Roberts. *Quantitative optical phase microscopy.* Optics Letters **23**(11), 817 (1998).

[124] a. Roberts, E. Ampem-Lassen, A. Barty, K. a. Nugent, G. W. Baxter, N. M. Dragomir, and S. T. Huntington. *Refractive-index profiling of optical fibers with axial symmetry by use of quantitative phase microscopy.* Optics Letters **27**(23), 2061 (2002).